N° d'ordre 2012ISAL0124 Année 2012

THESE

Présentée devant

L'INSTITUT NATIONAL DES SCIENCES APPLIQUEES DE LYON

pour obtenir

LE GRADE DE DOCTEUR

Spécialité : Génie Mécanique

ECOLE DOCTORALE DES SCIENCES DE L'INGENIEUR DE LYON :
Mécanique, Energétique, Génie civil, Acoustique (MEGA)

par

MUHIBULLAH

Computation Experimental DIC Hybrid Strategy for Robust 3D Ductile Plastic Law Identification

---

Thèse présentée le 27 novembre 2012

JURY :

Rafael Estevez	Professor, SIMAP, Grenoble	Rapporteur
Karine Bruyère	Assistant Professor, IFSTTAR, Lyon	Rapporteur
Jean-Luc Loubet	DR CNRS, ECL, Lyon	Président
Alain Combescure	Professor, INSA, Lyon	Directeur de thèse
Julien Réthoré	Assistant Professor, INSA, Lyon	Co-directeur
Thomas Elguedj	Assistant Professor, INSA, Lyon	Co-directeur

Université de Lyon, CNRS,
INSA-Lyon, LaMCoS UMR5259, F69621, France

INSA Direction de la Recherche - Ecoles Doctorales – Quinquennal 2011-2015

SIGLE	ECOLE DOCTORALE	NOM ET COORDONNEES DU RESPONSABLE
CHIMIE	CHIMIE DE LYON http://www.edchimie-lyon.fr Insa : R. GOURDON	M. Jean Marc LANCELIN Université de Lyon – Collège Doctoral Bât ESCPE 43 bd du 11 novembre 1918 69622 VILLEURBANNE Cedex Tél : 04.72.43 13 95 directeur@edchimie-lyon.fr
E.E.A.	ELECTRONIQUE, ELECTROTECHNIQUE, AUTOMATIQUE http://edeea.ec-lyon.fr Secrétariat : M.C. HAVGOUDOUKIAN eea@ec-lyon.fr	M. Gérard SCORLETTI Ecole Centrale de Lyon 36 avenue Guy de Collongue 69134 ECULLY Tél : 04.72.18 60 97 Fax : 04 78 43 37 17 Gerard.scorletti@ec-lyon.fr
E2M2	EVOLUTION, ECOSYSTEME, MICROBIOLOGIE, MODELISATION http://e2m2.universite-lyon.fr Insa : H. CHARLES	Mme Gudrun BORNETTE CNRS UMR 5023 LEHNA Université Claude Bernard Lyon 1 Bât Forel 43 bd du 11 novembre 1918 69622 VILLEURBANNE Cédex Tél : 04.72.43.12.94 e2m2@biomserv.univ-lyon1.fr
EDISS	INTERDISCIPLINAIRE SCIENCES-SANTE http://ww2.ibcp.fr/ediss Sec : Safia AIT CHALAL Insa : M. LAGARDE	M. Didier REVEL Hôpital Louis Pradel - Bâtiment Central 28 Avenue Doyen Lépine 69677 BRON Tél : 04.72.68 49 09 Fax :04 72 35 49 16 Didier.revel@creatis.uni-lyon1.fr
INFOMATHS	INFORMATIQUE ET MATHEMATIQUES http://infomaths.univ-lyon1.fr	M. Johannes KELLENDONK Université Claude Bernard Lyon 1 LIRIS – INFOMATHS- Bâtiment Nautibus 43 bd du 11 novembre 1918 69622 VILLEURBANNE Cedex Tél : 04.72. 43.19.05 Fax 04 72 43 13 10 infomaths@bat710.univ-lyon1.fr
Matériaux	MATERIAUX DE LYON	M. Jean-Yves BUFFIERE INSA de Lyon - École Doctorale Matériaux Secrétariat Mériem LABOUNE Bâtiment Antoine de Saint-Exupéry 25bis Avenue Jean Capelle 69621 VILLEURBANNE Tel : 04 72 43 71 70 Fax : 04 72 43 72 37 ed.materiaux@insa-lyon.fr
MEGA	MECANIQUE, ENERGETIQUE, GENIE CIVIL, ACOUSTIQUE (ED n°162)	M. Philippe BOISSE INSA de Lyon - École Doctorale MEGA Secrétariat Mériem LABOUNE Bâtiment Antoine de Saint-Exupéry 25bis Avenue Jean Capelle 69621 VILLEURBANNE Tel : 04 72 43 71 70 Fax : 04 72 43 72 37 mega@insa-lyon.fr Site web : http://www.ed-mega.com
ScSo	ScSo* M. OBADIA Lionel Sec : Viviane POLSINELLI Insa : J.Y. TOUSSAINT	M. OBADIA Lionel Université Lyon 2 86 rue Pasteur 69365 LYON Cedex 07 Tél : 04.78.69.72.76 Fax : 04.37.28.04.48 Lionel.Obadia@univ-lyon2.fr

*ScSo : Histoire, Geographie, Aménagement, Urbanisme, Archéologie, Science politique, Sociologie, Anthropologie

Acknowledgements

I am sincerely and heartily grateful to my director Dr.Alain Combescure and my co-directors Dr.Julien Réthoré & Dr.Thomas Elguedj for their support during my PhD. This thesis would not have been possible without their guidance. This work was performed by the funding of INSA Lyon.

I am also thankful to Mr.Philippe Chaudet and Mr.Paul Valverde for helping me out during experiments.

I spent great time with my colleagues at LaMCoS. Miss.Isabelle Comby helped me with administrative matters. Thanks all of you.

I am indebted to my father Mr.Salimullah & my mother Mrs. Nasreen Ara for providing me with everything that I ever wished for. I am grateful to my elder brother Mr.Asadullah & my sweet sisters for their encouragement. Many thanks to you all.

Finally, I like to thank God for such a wonderful life.
“Happy is the time of the man; who spends it in adoring thee.” – Sa’di.

Abstract

The objective of the thesis is to formulate a strategy that gives a robust identification of constitutive law from full-field measurements taking into account 3D effects. Model validation from global response of samples or structures has shortcomings that can be overcome by the use of full-field measurement techniques. Full-field measurement techniques offer the opportunity to acquire large amount of experimental data that might be useful in the context of identification of constitutive law parameters. Among the full field measurement techniques the most popular is digital and stereo image correlation.

The existing strategies to make use of full-field data like the Virtual Field Method, the Equilibrium Gap Method, the Constitutive Equation Gap Method and the Reciprocity Method were limited to 2D applications. However, for a specimen with finite thickness 3D effects must be included. Most importantly, for the case of plasticity, stress triaxiality plays an important role. Its effect must therefore be accounted for in the modelling of the constitutive behaviour of the material.

Thus in this thesis we propose a method to identify the parameters of an elasto-plastic constitutive law in which the mechanical model can have 3D kinematics. The strategy has been shown to be noise robust, almost independent of initial parameter guess and mesh refinement and allows differentiating between constitutive models with same global response on the basis of mean correlation error. The identification is shown to be good for both single and multiple cameras.

The strategy validation is done for stainless steel. The global identified load displacement response of the strategy for mono and stereo mechanical image correlation is very close to the experiments. Lastly, the material parameters have been identified with very different initial guess but all converge to the same final values which show the robustness of the proposed strategy.

Contents

Chapter 1 Bibliography

Chapter 2 Theory

Chapter 3 Application of the Method

Notations

$\boldsymbol{\sigma}$	Stress Tensor.
$\boldsymbol{\varepsilon}$	Strain Tensor.
ν	Poisson's ratio.
$\boldsymbol{\varepsilon}_p$	Plastic strain.
$\boldsymbol{\varepsilon}_e$	Elastic strain.
ν^*	Coefficient of contraction.
$\mathbf{g}$	Gradient.
$\mathbf{H}_s$	Hessian.
$\mathbf{J}$	Jacobian.
$\mathbf{h}_{lm}$	Step for Levenberg-Marquardt method.
$\mathbf{h}_{gn}$	Step for Gauss-Newton method.
μ	Damping parameter in Levenberg-Marquardt method.
$f(\mathbf{x})$	Reference image.
$g(\mathbf{x})$	Deformed image.
$\mathbf{u}$	Displacement field.
$\boldsymbol{A}$	Hooke Tensor.
$\boldsymbol{\theta}$	Vector of unknown constitutive parameters.
$\boldsymbol{W}_F$, $\boldsymbol{W}_{\mathrm{U}}$	Weighting matrices.
$\boldsymbol{K}$	Stiffness matrix.
$\boldsymbol{\Lambda}$	Current estimation of constitutive parameters.
$\mathbf{G}$	Vector of grey level values of deformed image g.
$\mathbf{V}$	Solution vector of simulation.
$\bar{\mathbf{F}}_{\mathrm{int}}$	Vector collecting internal forces.
$\mathbf{F}_{ext}$	Vector collecting external forces.
η	Convergence tolerance.
E	Young's modulus.
σ_y	Yield stress.
S_y	Initial yield stress (σ_y when $\varepsilon_p = 0$).
H	Linear hardening coefficient.
α	Penalty parameter.
$\mathbf{P}$	Projection operator.
$\mathbf{F}^0_{ext}$	Vector collecting external reaction forces obtained via numerical simulation with DIC displacement prescribed as boundary condition.
δ	exponent used in the power part of the assumed material model.
ε_0	scaling factor for the accumulated plastic strain.

Introduction

Many companies optimise their operations by means of FE simulations, resulting in a reduction of time and cost that would be used in doing experiments or in the “trial and error” phase of the investigation. However, for the success and reliability of the simulation it is important to have the accuracy of the input data, i.e. the geometry, the boundary conditions, the load distribution, the material data, etc. In such a case, a good knowledge of the material properties and constitutive law is essential to perform a sufficiently accurate simulation.

The standard way of evaluating the stress-strain relation of a material is by performing standardized tests with hypothesis on the stress and strain states. The shortcomings of these tests are threefold. Firstly, the deformation fields that are generated during these tests are homogeneous and do not resemble the complex heterogeneous deformation fields which occur during real situations (e.g., real metal forming operations, [2]). Even if we perform multiple complex experiments with intricate specimen geometries to be close to actual complex strain states, it increases the chances of experimental noise. It is thus evident that identification from a single experiment would minimise noise measurement and is desirable. Secondly, the assumption of uniformity is no longer valid after the onset of necking. Lastly, for the case of plasticity, it is well known that stress triaxiality plays an important role and has been used extensively in the literature on ductile fracture. Its effect must therefore be accounted for in the modelling of the constitutive behaviour of the material. Thus to circumvent these difficulties we need inverse methods that link numerical simulation with experiments.

Full field measurement techniques offer the possibility to acquire a large amount of experimental data that might be useful in the context of identification of constitutive law parameters. Among the full field measurement techniques, the most popular is Digital Image Correlation (DIC) thanks to its ease of implementation and its versatility in terms of scale of observation ranging from nanoscopic to macroscopic observations with essentially the same type of analyses. We can also upgrade DIC to measure out of plane kinematic fields by doing Stereo Image Correlation. In stereo we make use of two cameras (left and right) or a single moving camera for the 3D analysis of kinematic fields. An additional step in stereo would be the calibration of the camera system required to find the placement and operating characteristics of the cameras being used. The two simultaneous images of the same specimen from two different views can then be correlated with the reference image to find the unknown 3D displacements and strains.

Apart from these experimental methodologies, different inverse methods involving full field measurement techniques have also been developed. These methods can be sorted into two groups.

In the first group, the identification directly extracts the constitutive parameters from the measured displacement field. We have the Constitutive Equation Gap Method [3] based on the minimization of a functional expressing the gap in the constitutive equation; the Equilibrium Gap Method [4] minimises equilibrium residuals; the Virtual Field Method [5] uses virtual work principle.

For the second group, named the Finite Element Model Updating (FEMU) [6] family, the idea is to update the parameters of a constitutive model so that the result of a numerical simulation, run under appropriate boundary conditions, matches as fairly as possible the experimental field, obtained via for example DIC, in the sense of a given norm (or cost function).

A point to be noted is that in the first group except the Virtual field method, the constitutive parameters are formulated as a quadratic functional of the gradient of the measured displacement. This may lead to systematic bias and noise sensitivity. The virtual field method is a linear form of the measured strain and thus does not exhibit systematic bias. With respect to FEMU involving the minimization of the norm of the measured and computed displacements (or strains) with respect to constitutive parameters, no systematic bias is obtained and noise robust strategy can be achieved as will be shown in later chapters. Another way of reducing noise is to make the identification strategy as direct as possible. During the identification process, there is usually a difference between the kinematic hypotheses made during the measurement and simulation stages making the results erroneous. Thus by having identical description for the displacement field in DIC and numerical simulation, we can avoid the noise or uncertainty propagation in the identification chain.

The above mentioned strategies of constitutive law identification from full-field measurements have a common limitation that they are limited to two-dimensional applications when 2D full field data are analyzed. But if the specimen is thick, we should not neglect three-dimensional effects for results closer to the real situation. In this thesis we therefore tend to have 3D kinematics in the mechanical model by using DIC which gives us 2D kinematic fields. We also show the application of the method to stereo image correlation.

Thus the original work done by Réthoré [7] involving noise robust strategy of Integrated Mechanical Image Correlation has been extended to include 3D kinematics. The proposed strategy offers us following benefits:

- Allow us to account for 3D effects in the mechanical model
- Noise Robust
- Low sensitivity to initial parameter guess and to mesh refinement

- The proposed strategy gives a framework whereby we can discriminate between constitutive models that give similar global responses. This discrimination is based on the use of correlation error.
- This strategy allows us to use one, two or more cameras.

In summary, the present research work allows us to identify elasto-plastic constitutive laws from full field measurements by taking into account 3D effects that are important in finite strain plasticity.

This work has been divided into three chapters beginning with the introduction.

In the first chapter, we present the basics of constitutive law modelling, the experimental and numerical techniques used in the identification process including explanation to the DIC and the inverse methods utilizing full field data for the identification purposes.

In the second chapter, theory and formulation related to the original and modified strategy is presented. Its application to the use of single and multiple camera system is proposed. Numerical features required for the identification of elasto-plastic laws are detailed.

In the third chapter shows the application of the method. Firstly, a virtual testing procedure is implemented and explained. With the help of this virtual testing procedure, we can evaluate the performance of the proposed strategy with respect to initial parameter guess, convergence rates for different situations and other parameters involved in the formulation. Finally, experimental setup is elaborated, and then DIC and stereo analysis results are presented. Finally the strategy is applied to DIC and stereo results for the identification procedure. Correlation error analysis is also done to discriminate between different strategies used.

Lastly, concluding remarks are presented.

Bibliography [8, 40, 41]

Constitutive law parameters for the material are most often related to the constitutive properties of the material and hence their identification is an important step of the design process. It can guide us to predict the behaviour of a material in different conditions. We define Identification as: “All the work which consists in specifying the functions which appear in the model and in finding the numerical values of the coefficients which define the functions for each material”. This work broadly includes three main activities: experimentation, numerical identification and finally validation.

The standard method of identification involves the measurement of global quantities and to infer the values of the parameters from simple exact solutions and under an assumption of homogeneous strain and stress fields in the zone of interest. However, the recent developments of low cost CCD cameras and improvements in image processing with powerful and affordable PCs make non contact measurement techniques more and more appealing. The large amount of experimental data available via full field measurements is particularly interesting for identification (typically 1000 to 10,000 independent measurement points). We no longer have to be content with approximate measurements of a few quantities; we are now in a position to measure the evolution of any mathematically well defined variable precisely. The identification of complex models has thus become possible, but it requires numerical methods for the identification of non-linear processes.

With the help of this identification, we can associate a theory of only the dominant phenomena to the identified material (e.g. elastoplasticity). Beyond its fundamental interest, this offers a guide for the choice of material in the design stage and helps to simplify the estimation of the resistance of a structure under service loads.

Thus in the following pages, we discuss the traditional global method of modelling, the type of experimental tests involved, the digital image correlation and the computational strategies devised for the full field data.

1 The global method of constitutive law modelling

We generally distinguish three broad methods for formulating the constitutive laws of materials.

> The microscopic approach attempts to model the mechanics of deformation and fracture at the atomic, molecular and crystalline levels; the microscopic behaviour being the result of integration or of an averaging process performed over the microscopic variables at the scale of the volume element of continuum mechanics.
>
> The thermodynamic approach introduces a homogeneous continuous medium equivalent to the real medium and represents microscopic physical phenomena by means of macroscopic "internal variables".
>
> The functional approach leads to the hereditary laws of the integral type which appear as characteristic functions of materials, and which are themselves expressed in terms of macroscopic variables.

None of these approaches allows direct identification of materials. Microscopic variables (density of dislocation, density of cavities, texture …) are difficult to measure, and moreover are difficult to use in practical engineering computations. Thermodynamic potentials are practically inaccessible to measurement, and internal variables, by definition, cannot be measured directly. As the hereditary functions need the knowledge of the whole history of the observable variables, they pose theoretical as well as experimental problems.

The global phenomenological method consists in studying the volume element of matter through the relations between cause and effect which exist between the physically accessible variables constituting the input and output of the process under study. In this way, we are able to determine the material response to a specific input. These responses are sufficient to characterize the materials qualitatively, but they do not constitute (except for linear phenomena) the constitutive laws.

1.1 Volume Element: A volume element, in the sense of solid mechanics, means a volume of a size large enough with respect to the material heterogeneities, and small enough for the partial derivatives of the equations of the continuum to be meaningful. Mathematically, RVE is the infinite length scale limit relative to the micro-scale (or the length scale of a single heterogeneity), where the material appears uniform, and therefore, the continuum concepts are applicable. RVE is useful for modelling the effect of nano- and meso-scale heterogeneities on the overall mechanical response of the macro-size components/specimens. It can also be defined as the smallest volume element of a material for which the macroscopic constitutive representation is sufficiently accurate to represent overall constitutive response.

Materials	**Inhomogeneities**	**Volume Element**
Metals and alloys	Crystals 1μm-0.1 m	0.5 x 0.5 x 0.5 mm
Polymers	Molecules 10 μm – 0.05 mm	1 x 1 x1 mm
Wood	Fibres 0.1 mm- 1 mm	1 x 1 x1 cm
Concrete	Granulates ~ 1cm	10 x 10 x 10 cm

Table1. Orders of magnitude of representative volume elements

1.2 Physically Accessible Variables: The physically accessible variables of the volume element are those that can simply be deduced from the four classical and measurable magnitudes of mechanics: displacement, force, time, temperature.

The strains and their rates:

total three-dimensional strain $\boldsymbol{\varepsilon}$, or one-dimensional ε, with its large deformation expression $\varepsilon_v = \ln(1+\varepsilon)$.
reversible elastic strain $\boldsymbol{\varepsilon}^{\mathbf{e}}$ or ε^e ,
permanent strain $\boldsymbol{\varepsilon}^{\mathbf{p}}$ or ε^p.

The three-dimensional stress $\boldsymbol{\sigma}$, or one-dimensional stress σ, with the approximate expression for large deformations $\sigma_v = \sigma(1+\varepsilon)$.

The temperature T.

The time t or the number of cycles to rupture t_R or N_R

1.3 Limitation of the global method: The classification resulting from the global phenomenological method should not be considered intrinsic. It provides, in fact, only a frame of reference for general characteristics. The behaviour of a given material can be represented by a schematic model only in relation to the envisaged usage and the desired precision of the predictions.
A given piece of steel at room temperature can be considered to be:

Linear, elastic for structural analysis,

visco-elastic for problems of vibration damping,

rigid, perfectly plastic for calculation of the limit loads,

hardening elastoplastic for an accurate calculation of the permanent deformations,

elastoviscoplastic for problems of stress relaxation,

damageable by ductility for calculation of the forming limits,

damageable by fatigue for calculation of the life-time, etc.

2 Experimental Techniques and Identification Process

The basic idea of modelling the constitutive law of a material from its global response is to match the stress-strain curve obtained via experiments with the model. In the following sections we describe the characteristic tests and experiments necessary for the standard modelling procedure.

2.1 Representative experiments of material behaviour[8]: The classical characteristic tests are essentially conducted in simple tension, or tension-compression at constant temperature. The classification of real solids is therefore based upon these tests. The specimen is subjected to an axial load (force or displacement) which produces a uniform state of stress or strain within the whole useful volume of the specimen which can be considered as one volume element.

What follows applies to isotropic materials.

The uniaxial state is defined by a one-dimensional state of stress and a two-dimensional state of strain:

$$\sigma = \begin{pmatrix} \sigma & 0 & 0 \\ 0 & 0 & 0 \\ 0 & 0 & 0 \end{pmatrix} \qquad \varepsilon = \begin{pmatrix} \varepsilon & 0 & 0 \\ 0 & -\nu^*\varepsilon & 0 \\ 0 & 0 & -\nu^*\varepsilon \end{pmatrix} \tag{2.1}$$

where ν^* is the coefficient of contraction, equal to Poisson's ratio ν in elasticity.

In elastoplasticity or elastoviscoplasticity the hypotheses of the decoupling of elastic and plastic strains ($\varepsilon = \varepsilon^e + \varepsilon^p$) and of plastic incompressibility (Tr(ε^p)= 0) allow us to express the contraction coefficient ν^* simply as:

$$\begin{pmatrix} \varepsilon & 0 & 0 \\ 0 & -\nu^*\varepsilon & 0 \\ 0 & 0 & -\nu^*\varepsilon \end{pmatrix} = \begin{pmatrix} \varepsilon_e & 0 & 0 \\ 0 & -\nu\varepsilon_e & 0 \\ 0 & 0 & -\nu\varepsilon_e \end{pmatrix} + \begin{pmatrix} \varepsilon_p & 0 & 0 \\ 0 & -0.5\varepsilon_p & 0 \\ 0 & 0 & -0.5\varepsilon_p \end{pmatrix} \tag{2.2}$$

$$\nu^* = \nu\frac{\varepsilon_e}{\varepsilon} + \frac{1}{2}\frac{\varepsilon_p}{\varepsilon} \tag{2.3}$$

or with the help of linear elastic law: $\varepsilon_e = \frac{\sigma}{E}$, as

$$\nu^* = \frac{1}{2} - \frac{\sigma}{E\varepsilon}\left(\frac{1}{2} - \nu\right) \tag{2.4}$$

***Hardening test in simple tension or compression*:** This is the most common test. The specimen is subjected to a deformation at constant speed. The response consists of a variation in the stress σ as a function of the strain ε showing the hardening of the material (Fig.2.1)

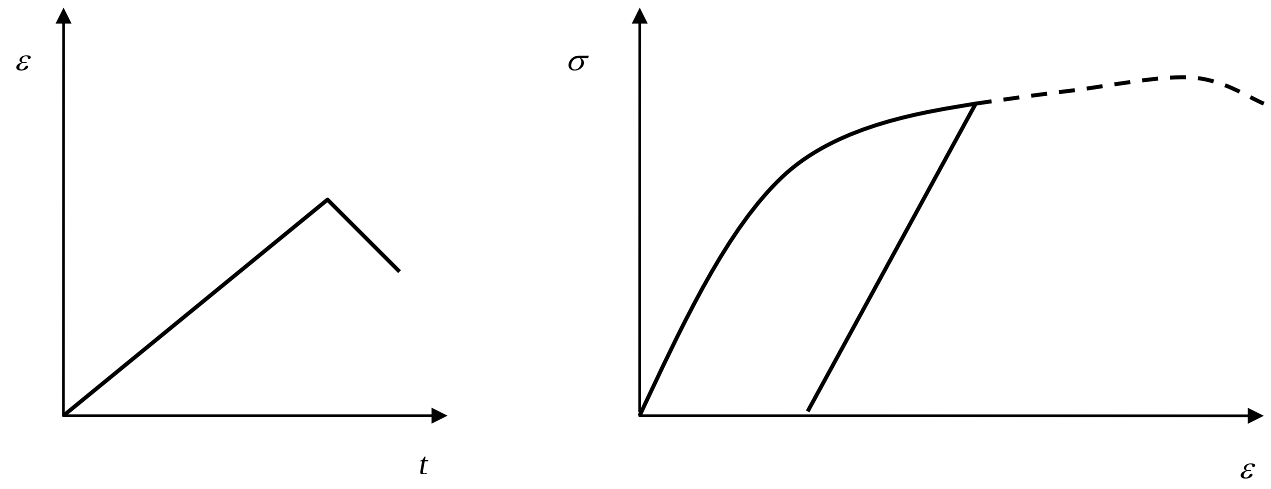

Fig.2.1 Hardening Test

***Creep test in simple tension or compression*:** In this test the specimen is subjected to a constant state of stress (generally apparent stress) and the resulting variation in strain ε as a function of time *t* is determined. This also characterizes the hardening and the viscosity of the material (Fig.2). The strain variation after the stress is removed (point B) corresponds to the recovery test. The partial strain recovery is indicated on the right hand side of Fig.2.2.

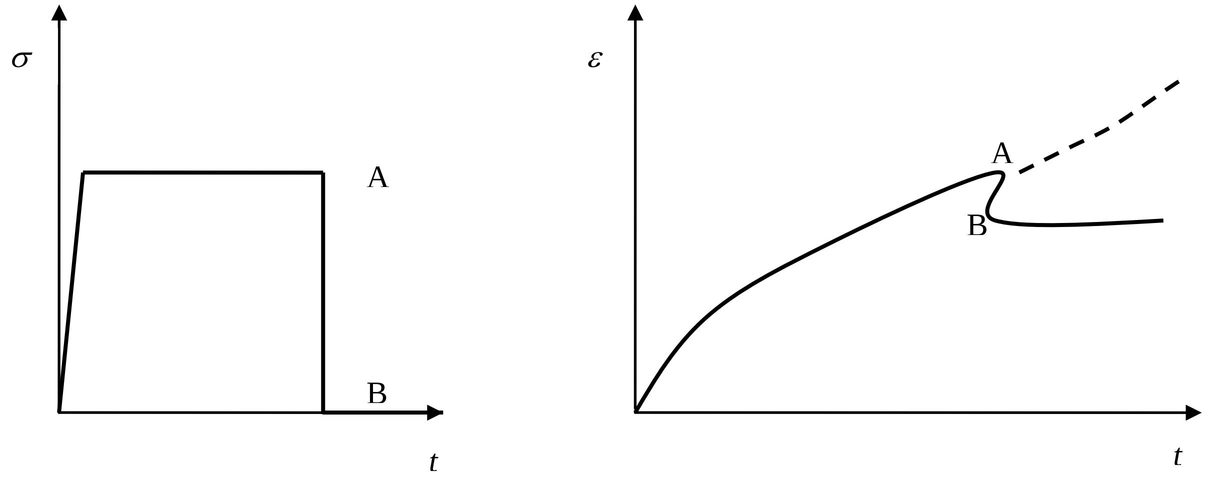

Fig.2.2 Creep Test and subsequent recovery

***Relaxation in simple tension or compression*:** This test is complementary to the preceding one in that the stress response to a constant state of strain is determined. It is governed by the viscosity but also depends on the hardening induced by the initial load (Fig.2.3)

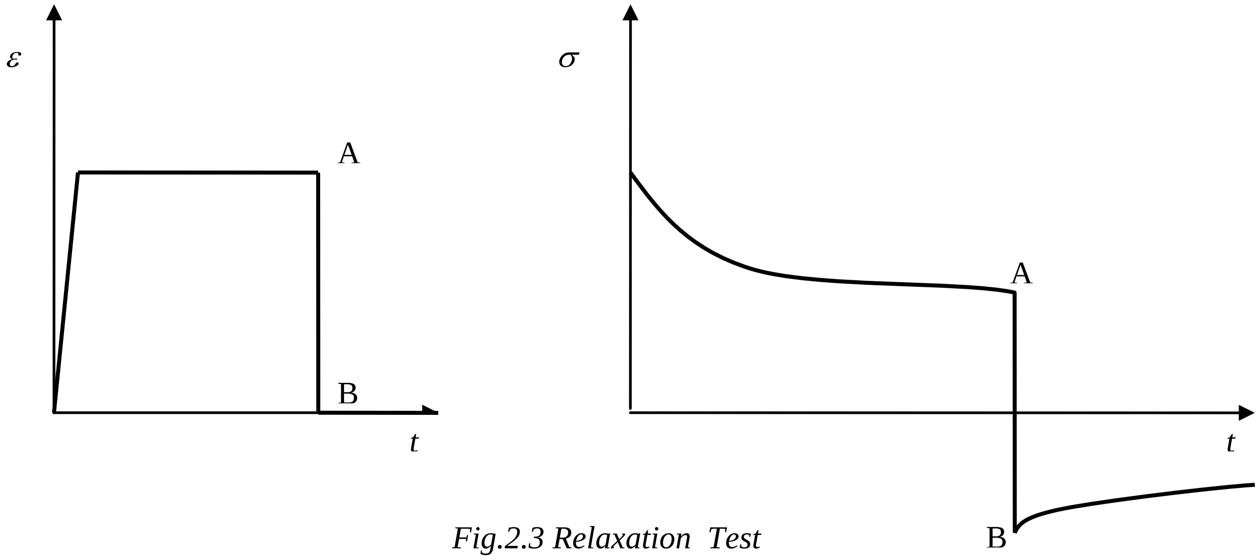

Fig.2.3 Relaxation Test

***Relaxation in simple tension or compression*:** As the name indicates, this test combines the two types of tests and allows us to determine from a single specimen the hardening characteristics, and also the viscosity, by means of successive relaxations each at differentstrain levels.

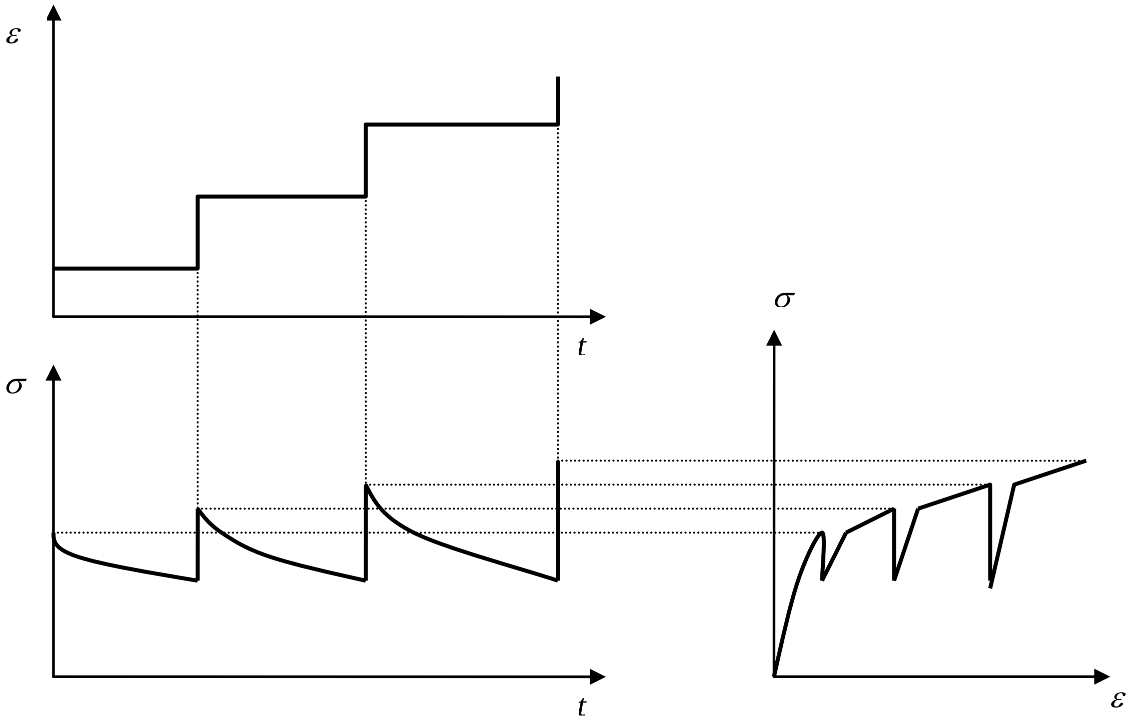

Fig.2.4 Multiple hardening-relaxation test

Cyclic Test**:** In this test the specimen is subjected to a periodic load (stress or strain) and the evolution of the cyclic responses is studied by obtaining a (σ, ε) graph (Fig.2.5). In general the response tends to be stabilized after a certain number of cycles. We can then obtain the cyclic curve which represents a relation between the peaks of the stabilized loops, corresponding to different stress or strain levels (Fig.2.6). In the case of polymeric materials, or more generally, in viscoelastic materials the peaks of the loops are difficult to define. We then speak of 'harmonic tests'.

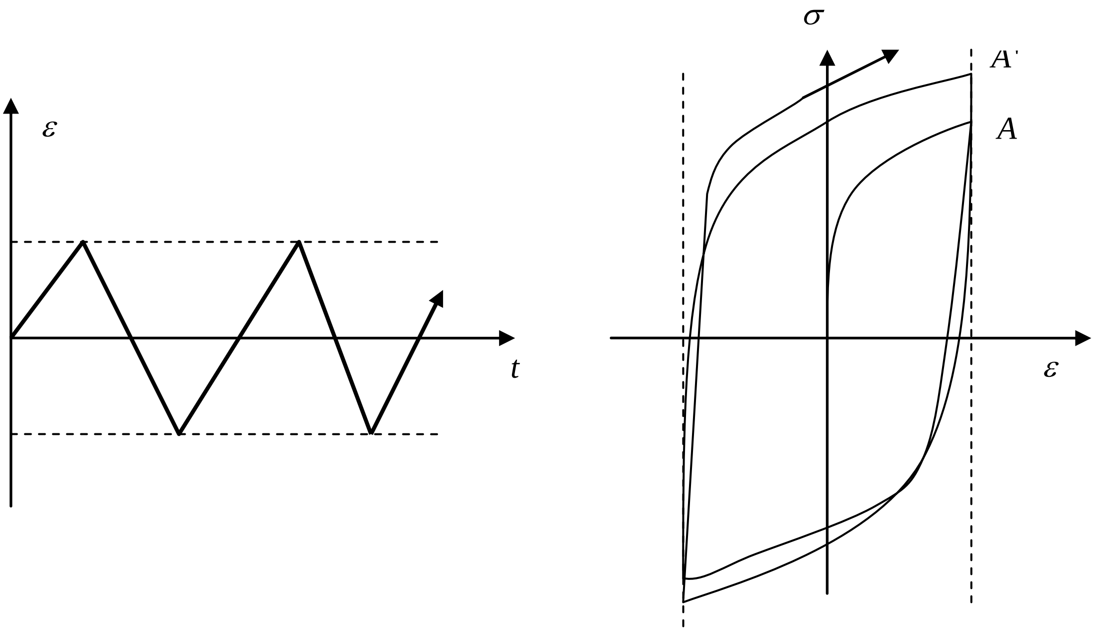

Fig.2.5 Cyclic test under prescribed load

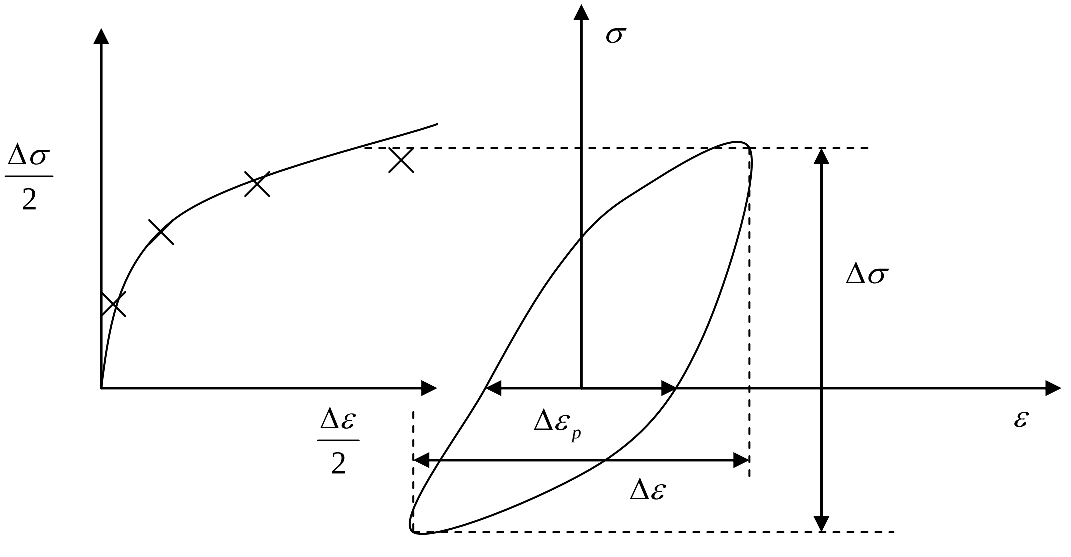

Fig.2.6 Cyclic hardening curve

Fracture Tests**:** The four preceding types of tests are also used to determine the corresponding fracture conditions:

stress and strain at fracture
time or number of cycles to fracture
energy dissipated in fracture.

Certain characteristics require the use of specimens of a particular geometry (notched specimens for measuring impact strength in the Charpy test, cracked specimens for measuring toughness, etc.).

2.2 Testing Machine: The phenomenological method requires the experiments to be made on a volume element of matter. As far as possible the specimens should be subjected to a uniform field of stress, strain and temperature. This is one of the difficulties of mechanical testing for the characterization of materials.

Uniaxial monotonic and cyclic tests: The most common test is a simple tension test in which the useful part of the specimen is subjected to a uniform uniaxial stress field. The essential elements of a testing machine are as follows:

the system for holding the heads of the specimen;
the dynamometer measuring the force applied to the specimen,
the transducer measuring the variation of length of the specimen,
the frame of the machine, which should be as stiff as possible,
the heating device,
the device for applying the forces.

Depending on the type of loading required, the stresses are applied differently: a system of weights for creep testing machines, a continuous screw-nut system driven by an electric motor, a servo-controlled hydraulic system for more sophisticated set-ups. The specimen itself includes a useful part consisting of a cylindrical shaft (Fig.2.8), end grips, and between the two, shoulders designed to minimize the stress concentration.

For tension tests, the useful part can be very long but is limited by the restriction due to machining and heating devices. In contrast, compression tests require much more compact specimens in order to avoid buckling problems.

For tests at high temperatures either resistance furnaces are used, or the Joule effect (due to electrical resistance of the sample) or high frequency induction are used to heat the specimen; the latter method is a better one for tests of short or medium duration. The choice of technique depends on the type of test (monotonic or cyclic) and on the temperatures to be reached (uniform, constant or variable temperature).

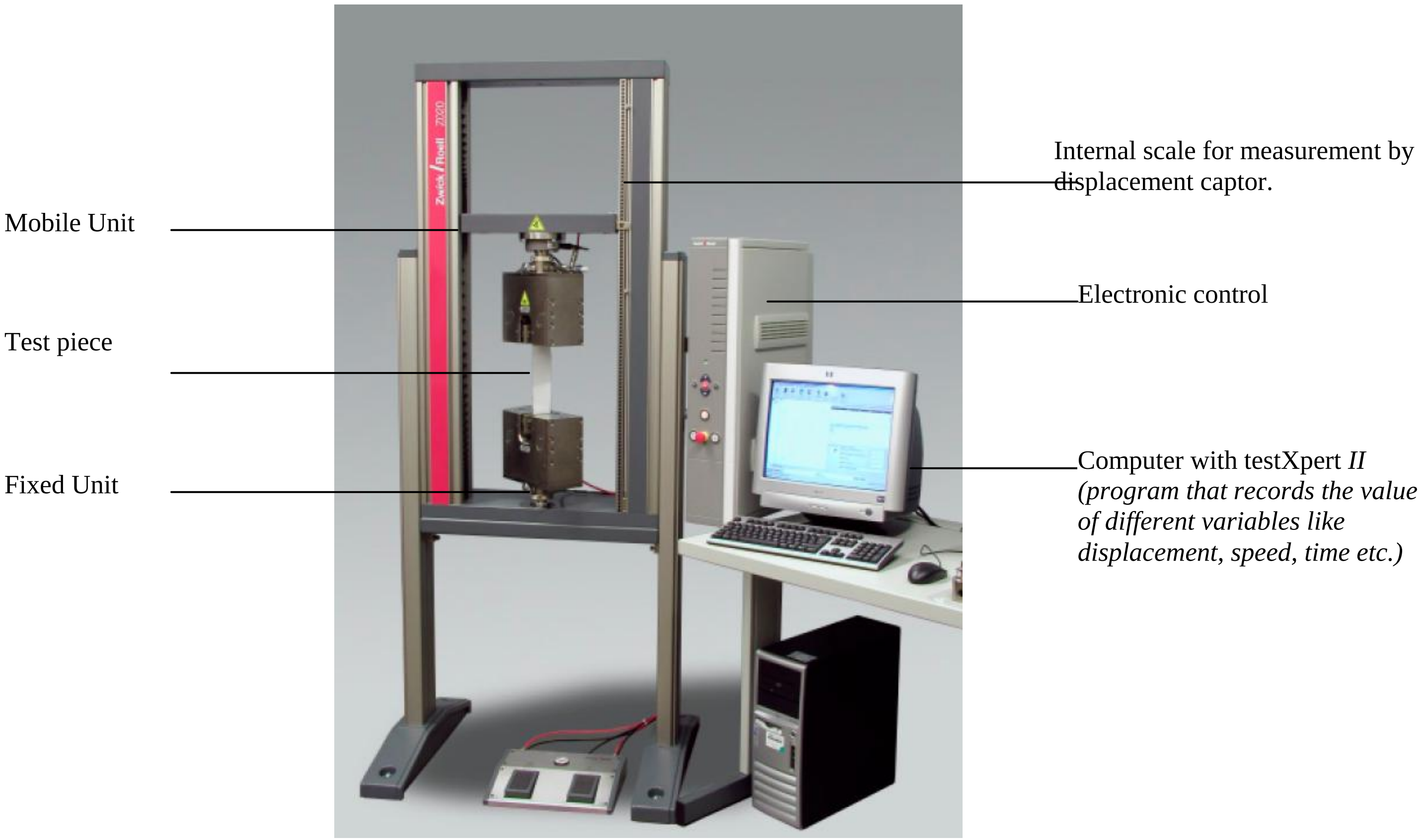

Fig.2.7 Zwick Tensile testing machine used during the experiments

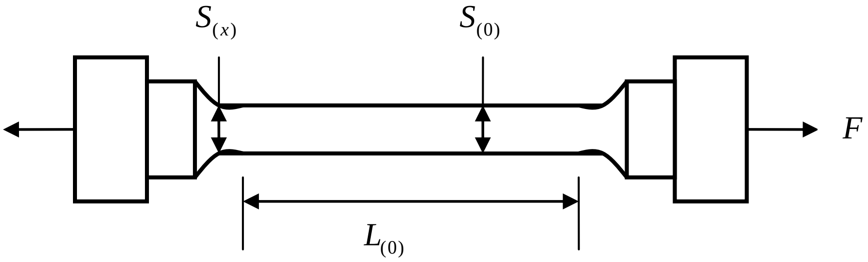

Fig. 2.8 Specimen for a tension test

2.3 Measurement of characteristic variables: Stresses can be deduced from forces by static equations for isostatic cases. The forces (or couples) applied to the specimens are measured by dynamometers mounted in series with the specimens. The dynamometers, equipped with strain gauges, have a relative precision of 10^{-3} which is generally sufficient for the characterization of materials.

The measurement of relative displacement between two points on a specimen is a much more delicate operation than the measurement of the loading force. To measure relative displacement it is necessary to connect a strain gauge in “parallel” with the sample and not in series. Essentially two techniques are used: local measurements by electrical resistance strain gauges, and global displacement measurements.

Wire Strain gauges: A resistance wire, well glued to the specimen, experiences the same strain as the specimen. It therefore follows that the variation in electrical resistance will be proportional to the strain ε. A precise measurement of this variation in resistance is obtained by employing a Wheatstone bridge; this can detect strains of the order of $\varepsilon = 10^{-7}$. However, the qualification 'well glued' mentioned above limits the applicability of this particularly useful technique. Adhesives do not withstand high temperature, and hence, these strain gauges are only used at, or below, room temperature, or at slightly higher temperature (not more than 200-400°C).

Displacement Transducers: The strain can also be deduced from the equations of continuum mechanics and knowledge of the displacement between two material points of the specimen. The axial displacement can be measured by an extensometer attached either to the cylindrical part of the specimen through knife edges, or to the gripping heads of the specimen. The variation in the diameter of the specimen can also be measured but without using the knife edges which very often initiate a fracture. The evolution, however, must take into account the variation of Poisson's coefficient in the presence of plastic strains. With inductive extensometers or with strain gauges, an absolute precision of $1\,\mu m$ can be attained. With optical extensometers this precision can be improved to $0.2\,\mu m$, but these are expensive and delicate instruments.

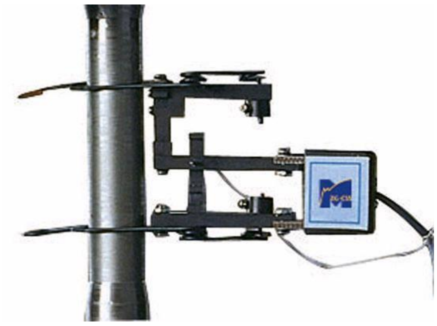

Fig. 2.9 Extensometer attached to a tensile test specimen

Plastic deformation: The useful length of a sample is the length L_0 which becomes L under the load, and which can be used to calculate the longitudinal strain by the simple relation:

$$\varepsilon = \frac{L - L_0}{L_0} \tag{2.5}$$

The plastic strain can be obtained by subtracting the elastic strain from the total strain ε (measured, for example, by an electric resistance strain gauge). In tension (compression) we then have:

$$\varepsilon_p = \varepsilon - \varepsilon_e = \varepsilon - \frac{\sigma}{E} = \varepsilon - \frac{F}{ES} \tag{2.6}$$

where S is the current cross-sectional area of the specimen .

The modulus of elasticity is obtained from data at the beginning of the test when the force is sufficiently low for the specimen to remain elastic. We then obtain:

$$E = \frac{F}{S\varepsilon_e} \tag{2.7}$$

When the extensometer cannot be connected directly onto the cylindrical part of the specimen, we take an equivalent useful length L_p corrected to take into account the plastic deformations in the connection areas. Employing the notation of Fig.2.8, this is defined by:

$$L_p = \frac{u_p}{\varepsilon_{p(0)}} = 2\int_0^{L/2} \frac{\varepsilon_{p(x)}}{\varepsilon_{p(0)}} dx \tag{2.8}$$

Plastic strain can also be expressed as a power function of the stress $\varepsilon_p = \left(\frac{\sigma}{K}\right)^{1/M}$. By a method of slicing, and neglecting the triaxiality effect in the connection zones, we can show that:

$$L_p = 2\int_0^{L/2} \left(\frac{S_{(0)}}{S_{(x)}}\right)^M dx \tag{2.9}$$

The useful plastic length is thus defined from the geometry of the specimen (law of variation of section $S_{(x)}$ and the hardening exponent. The procedure used to measure the plastic strain is therefore the following:

Determine the force-displacement relation by direct readings in a tension test (for example),

Subtract the initial displacement $u_{(j)}$ and the elastic displacement to obtain the plastic displacement. The stiffness R of the specimen and the grips at the level of the extensometer is obtained from the initial readings in the elastic domain. Then:

$$u_p = u - u_j - F/R \tag{2.10}$$

The relation $F(u_p)$ furnishes an approximation to the hardening exponent. In fact, an identity exists between the exponents of the power laws:

$\sigma = K\varepsilon_p^M$ and $F = K'u_p^M$ since $\sigma = F/S$ and $\varepsilon_p = u_p / L_p$.

The equivalent useful length L_p can be derived from these equations, and hence,

$$\varepsilon_p = u_p / L_p \tag{2.11}$$

It should be noted that this useful length can be defined by a preliminary test for a given specimen, material and temperature. Even if the hypotheses used to establish it are not completely rigorous, they are sufficient since the correction is, in fact, small with respect to the length of the cylindrical zone.

2.4 Sample Preparation: The preparation of the specimens is always a long and delicate task as, unless care is taken, fracture can occur prematurely and not precisely where it is expected. It always involves a compromise between the implications of the machine characteristics (loading type, maximum force, stiffness, heating system) and the implications of the measurements to be carried out (sensitivity of the dynamometers, elongation measurements by extensometers placed locally on the useful part of the specimen or externally on the gripping heads).

2.5 Identification Methods: Thermodynamics gives the general formulation of models without specifying their analytical form (except, however, for linear behaviour) or numerical values. On the other hand, experiments provide, for each material, the quantitative relations to be verified by the models constructed to represent the phenomena under study. Identification can be defined as all the work which consists in specifying the functions which appear in the model and in finding the numerical values of the coefficients which define the functions for each material. This represents a difficult task which does not follow any rigorous rules and in which experience and 'art of model construction' play a major role in steering between theory and experiment.

2.5.1 Quality versus Price: Given a set of experimental results, it is always possible to find a function which represents it with an error not greater than the margin of uncertainty in measurements. This is called fitting. Since the number of experimental points can be large, the fitting may require functions with a large number of representative coefficients.

On the other hand, a model which has the ambition of becoming a law must possess a general character, so that while identified only by a restricted number of experiments, it is representative of other types of experiments with a predictive capability. The totality of the situations verified by a model is its field of validity. This characterizes the goodness of the model and is expressed qualitatively by the range of the variations within which the model agrees with the physics.

The number of coefficients represents the price to pay since the difficulties of identification lie in this number. It may be easy to identify two coefficients by a 'hand procedure', but the identification of say five coefficients in a model will involve considerable numerical work; and the identification of say ten of them really belongs to 'computer-aided art'. Therefore to evaluate a model it is necessary to examine this relation of quality/price= domain of validity/number of coefficients clearly.

2.5.2 Modelling non-linear phenomenon: Plasticity is a nonlinear phenomenon, in the sense that a linearization limited to the first order Taylor expansion represents the phenomenon only for a very small change in the variables. Among all the analytical possibilities for representing nonlinearities, the following are most common:

the exponential: exp(aX) or the logarithm ln(aX)

the power function aX^n where N is a coefficient which may take the values, 2,5,10,20 or even 100. In some cases it is necessary to use the function $aX^{N(X)}$ in which N itself is a function of X.

The reasons for this are essentially twofold:

the easy identification by logarithmic transformation which yields linear relations,

the possibility of obtaining analytical solutions of models for studying their properties.

3 Numerical Methods of Minimization [40, 41]

Knowing a mathematical model by its analytical expression, and obtaining a set of experimental results in which all the variables of the model have been activated, we are in a position to calculate the unknown coefficients which give the best representation of the experimental results. We thus tend to minimize the difference between the experimental and estimated set of values.

Generalities
Let us mention at once that problems arise differently depending on the test data available and the model under study. Two cases have to be distinguished.

The constitutive law is directly identified, i.e., we seek the entity (or the transfer function) representative of the material. One example of this is a law in which a variable X and its derivative $\dot{X}$ are present:

$H(X, \dot{X}, Y) = 0$

Once a series of triplets of values $(X, \dot{X}, Y)$ have been measured (at the same instant), the coefficients which define the above function H can be obtained by direct fitting of the experimental points. Depending upon the particular case, we may use a linear or nonlinear least-squares method to obtain these coefficients.
The response is identified, i.e., the coefficients of the function H are determined, by adjusting in the best possible way, the response values obtained from the assumed constitutive equation for a given load (input) against values obtained experimentally under the same load. In this case we use a nonlinear least-squares method, since the response cannot usually be stated explicitly in a simple analytic way.

Remarks
A given model cannot be identified correctly unless a sufficient number of test results are available which embrace a significant range of variation of each of the parameters (for example, the parameters, $X, \dot{X}$ and Y in the above function H). Otherwise, we run the risk of not determining one or more coefficients well enough.

For an identical material and model, it may be necessary to define several sets of coefficients, each better suited to a domain of variation or to a load type, for example, rapid transient loads, short-term loads, long-term loads and stationary loads.

In the art of identification, least squares problems are at the heart of computational strategy involved. The following pages describe the basic definition and the various methods related to the least square problems.

3.1 Introduction and Definitions [40]: Our objective is to minimize the discrepancy between the experimental data and the estimated values from a model. Different norms may be used, and generally speaking, we have the problem of minimizing an error function, which depends on the unknown coefficients. Different methods of minimization can be used. They have different efficiencies; however, in general, convergence may be difficult to achieve, due to large nonlinearities of the phenomena generally studied.
We define the least Squares Problem as:

Definition 1.1. Least Squares Problem

Find x^*, a local minimizer for

$F(\mathbf{x}) = \frac{1}{2}\sum_{i=1}^{m}(f_i(\mathbf{x}))^2$

where $f_i : \mathbb{R}^n \mapsto \mathbb{R}, i = 1,...,m$ are given functions, and $m \geq n$.

We thus have to find the argument of F that gives the minimum value of this so-called *objective* or *cost function*. We define the global minimizer as:

Definition 1.2. Global Minimizer

Given $F : \mathbb{R}^n \mapsto \mathbb{R}$. Find

$\mathbf{x}^+ = \arg\min_{\mathbf{x}} \{F(\mathbf{x})\}$

This problem is very hard to solve in general. For solving the simpler problem of finding a local minimizer for F, an argument verctor which gives a minimum value of F inside a certain region whose size is given by δ, where δ is a small, positive number.

Definition 1.3. Local Minimizer

Given $F : \mathbb{R}^n \mapsto \mathbb{R}$. Find $\mathbf{x}^*$ such that

$F(\mathbf{x}^*) \leq F(\mathbf{x})$ for $\| \mathbf{x} - \mathbf{x}^* \| < \delta$ where $\|.\|$ is the L_2-norm,

We assume that the cost function F is differentiable and so smooth that the following Taylor exapansion is valid:

$$F(\mathbf{x}+\mathbf{h}) = F(\mathbf{x}) + \mathbf{h}^T\mathbf{g} + \frac{1}{2}\mathbf{h}^T\mathbf{H}_s\mathbf{h} + O(\|\mathbf{h}\|^3) \tag{2.12}$$

where $\mathbf{g}$ is the gradient,

$$\mathbf{g} \equiv \mathbf{F'}(\mathbf{x}) = \begin{pmatrix} \frac{\partial F}{\partial x_1}(\mathbf{x}) \\ \vdots \\ \frac{\partial F}{\partial x_n}(\mathbf{x}) \end{pmatrix} \tag{2.13}$$

and $\mathbf{H}$ is the Hessian,

$$\mathbf{H} \equiv \mathbf{F}''(\mathbf{x}) = \left(\frac{\partial^2 F}{\partial x_i \partial x_j}(\mathbf{x}) \right) \tag{2.14}$$

If $\mathbf{x}^*$ is a local minimizer and $\|\mathbf{h}\|$ is sufficiently small, then we cannot find a point $\mathbf{x}^* + \mathbf{h}$ with a smaller F -value. Combining this observation with (2.12) we get:

Theorem 1.1. Necessary condition for a local minimizer

If $\mathbf{x}^*$ is a local minimizer, then
$\mathbf{g}^* \equiv \mathbf{F}'(\mathbf{x}^*) = 0$

We use a special name for arguments that satisfy the necessary conditions:

Definition 1.4. Stationary Point

If $\mathbf{g}_s = \mathbf{F}'(x_s) = 0$,
then $\mathbf{x}_s$ is said to be a stationary point for F .

Thus a local minimizer is also a stationary point, but so is a local maximizer. A stationary point which is neither a local maximizer nor a local minimizer is called a saddle point. In order to determine whether a given stationary point is a local maximizer or not, we need to include the second order term in the Taylor series (2.12). Inserting $\mathbf{x}_s$ we see that:

$$F(\mathbf{x}_s + \mathbf{h}) = F(\mathbf{x}_s) + \frac{1}{2}\mathbf{h}^T\mathbf{H}_s\mathbf{h} + O(\|\mathbf{h}\|^3) \tag{2.15}$$

with $\mathbf{H}_s = \mathbf{F}''(\mathbf{x}_s)$.

From definition (2.14) of the Hessian it follows that any $\mathbf{H}$ is a symmetric matrix. If we request that $\mathbf{H}_s$ is positive definite, then its eigenvalues are greater than some number $\delta > 0$ and $\mathbf{h}^T\mathbf{H}_s\mathbf{h} > \delta\|\mathbf{h}\|^2$.

This shows that for $\|\mathbf{h}\|$ sufficiently small the third term on the right-hand side of (2.15) will be dominated by the second. This term is positive, so that we get

Theorem 1.2. Sufficient condition for a local minimizer

Assume that $\mathbf{x}_s$ is a stationary point and that $\mathbf{F}''(\mathbf{x}_s)$ is positive definite.
Then $\mathbf{x}_s$ is a local minimizer.

If $\mathbf{H}_s$ is negative definite, then $\mathbf{x}_s$ is a local maximizer. If $\mathbf{H}_s$ is indefinite (i.e., it has both positive and negative eigenvalues), then $\mathbf{x}_s$ is a saddle point.

3.2 Descent Methods: All methods for non-linear optimization are iterative: From a starting point $\mathbf{x}_0$ the method produces a series of vectors $\mathbf{x}_1, \mathbf{x}_2, ...$, which (hopefully) converges to $\mathbf{x}^*$, a local minimizer for the given function. Most methods have measures which enforce the *descending condition*

$$F(\mathbf{x}_{k+1}) < F(\mathbf{x}_k) \tag{2.16}$$

This prevents convergence to a maximizer and also makes it less probable that we converge towards a saddle point. If the given function has several minimizers the result will depend on the starting point $\mathbf{x}_0$. We do not know which of the minimizers that will be found; it is not necessarily the minimizer closest to $\mathbf{x}_0$.

In many cases the method produces vectors which converge towards the minimizer in two clearly different stages. When $\mathbf{x}_0$ is far from the solution we want the method to produce iterates which move steadily towards x^*. In this “global stage” of the iteration we are satisfied if the errors do not increase except in the very first steps, i.e,

$$\| e_{k+1} \| < \| e_k \| \tag{2.17}$$

where $\| e_k \|$ denotes the current error,

$$e_k = \mathbf{x}_k - \mathbf{x}^* \tag{2.18}$$

In the final stage of the iteration, where $\mathbf{x}_k$ is close to $\mathbf{x}^*$, we want faster convergence. We distinguish between

Linear Convergence:

$$\| e_{k+1} \| \le a \| e_k \| \text{ when } \| e_k \| \text{ is small; } 0 < a < 1, \tag{2.19a}$$

Quardratic Convergence:

$$\| e_{k+1} \| = O(\| e_k \|^2) \text{ when } \| e_k \| \text{ is small,} \tag{2.19b}$$

Superlinear Convergence:

$$\| e_{k+1} \| / \| e_k \| \to 0 \text{ for } k \to \infty \tag{2.19c}$$

```
Algorithm 1.1 Descent Method
begin
  $k := 0; \mathbf{x} := \mathbf{x}_0$; found := false                {starting Point}
  while (not found) and ( $k < k_{\max}$ )
    $\mathbf{h}_d :=$ search_direction($\mathbf{x}$)              {From $\mathbf{x}$ and downhill}
    if (no such h exists)
      found:=ture                                    { $\mathbf{x}$ is stationary}
    else
      $\alpha :=$ step_length($\mathbf{x}, \mathbf{h}_d$)        {from $\mathbf{x}$ in direction $\mathbf{h}_d$ }
      $\mathbf{x} := \mathbf{x} + \alpha \mathbf{h}_d$; $k := k + 1$
end
```

One step from the current iterate consists in

1. Find a descent direction $\mathbf{h}_d$ and

2. Find a step length giving a good decrease in the F -value

Consider the variation of the F -value along the half line starting at $\mathbf{x}$ and with direction $\mathbf{h}$. From the Taylor expansion (2.15) we see that

$$F(\mathbf{x}+\alpha\mathbf{h}) = F(\mathbf{x})+\alpha\mathbf{h}^T\mathbf{F}'(\mathbf{x})+O(\alpha^2) \tag{2.20}$$

which for α sufficiently small becomes

$$F(\mathbf{x}+\alpha\mathbf{h}) \simeq F(\mathbf{x})+\alpha\mathbf{h}^T\mathbf{F}'(\mathbf{x}) \tag{2.21}$$

We say that $\mathbf{h}$ is a *descent direction* if $F(\mathbf{x}+\alpha\mathbf{h})$ is a decreasing function of α at α =0. This leads to the following definition.

Definition 1.5 Descent direction.
$\mathbf{h}$ is a descent direction for F at $\mathbf{x}$ if $\mathbf{h}^T\mathbf{F}'(\mathbf{x})$ <0

If no such $\mathbf{h}$ exists, then $\mathbf{F}'(\mathbf{x})$ =0, showing that in this case $\mathbf{x}$ is stationary. Otherwise we have to choose α, i.e., how far we should go from $\mathbf{x}$ in the direction given by $\mathbf{h}_d$, so that we get a decrease in the value of the objective function. One way of doing this is to find (an approximation to)

$$\alpha_e = \arg\min_{\alpha>0}\{F(\mathbf{x}+\alpha\mathbf{h})\} \tag{2.22}$$

This process is called as *line search* and is dicussed later. First, however are two methods for computing the descent direction.

3.2.1 The steepest Descent method: From (2.21) we see that when we perform a step $\alpha\mathbf{h}$ with positive α, then the relative gain in function value satisfies

$$\lim_{\alpha\to 0}\frac{F(\mathbf{x})-F(\mathbf{x}+\alpha\mathbf{h})}{\alpha\,||\mathbf{h}||} = -\frac{1}{||\mathbf{h}||}\mathbf{h}^T\mathbf{F}'(\mathbf{x}) = -||\mathbf{F}'(\mathbf{x})||\cos\theta \tag{2.23}$$

where θ is the angle between the vectors $\mathbf{h}$ and $\mathbf{F}'(\mathbf{x})$. This shows that we get the greatest gain rate if $\theta=\pi$, i;e, if we use the steepest descent direction $\mathbf{h}_{sd}$ given by

$$\mathbf{h}_{sd} = -\mathbf{F}'(\mathbf{x}) \tag{2.24}$$

The method based on (2.24) is called the steepest descent method or gradient method.

The choice of descent direction is “the best” locally and we could combine it with an exact line search (2.22). A method like this converges, but the final convergence is linear and often very slow.

3.2.2 Newton’s method: We can derive this method from the condition that $\mathbf{x}^*$ is a stationary point and thus satisfies $\mathbf{F}'(\mathbf{x}^*) = 0$. Also ignoring second and higher order terms of $||\mathbf{h}||$ we get

$$\mathbf{F}'(\mathbf{x}+\mathbf{h}) \simeq \mathbf{F}'(\mathbf{x})+\mathbf{F}''(\mathbf{x})\mathbf{h} \tag{2.25}$$

We now derive the Newton method: Find $\mathbf{h}_n$ as the solution to

$$\mathbf{H}\mathbf{h}_n = -\mathbf{F}'(\mathbf{x}) \text{ with } \mathbf{H} = \mathbf{F}''(\mathbf{x}) \tag{2.26}$$

and compute the next iterate by

$$\mathbf{x} := \mathbf{x} + \mathbf{h}_n \tag{2.27}$$

where $\mathbf{h}_n$ is the descent direction.

Newton's method is very good in the final stage of the iteration, where $\mathbf{x}$ is close to $\mathbf{x}^*$.

3.2.3 Line Search: Given a point $\mathbf{x}$ and a descent direction $\mathbf{h}$. The next iteration step is a move from $\mathbf{x}$ in direction $\mathbf{h}$. To find out, how far to move, we study the variation of the given function along the half line from $\mathbf{x}$ in the direction of $\mathbf{h}$,

$$\varphi(\alpha) = F(\mathbf{x} + \alpha\mathbf{h}),\ \mathbf{x} \text{ and } \mathbf{h} \text{ fixed, } \alpha \geq 0 \tag{2.28}$$

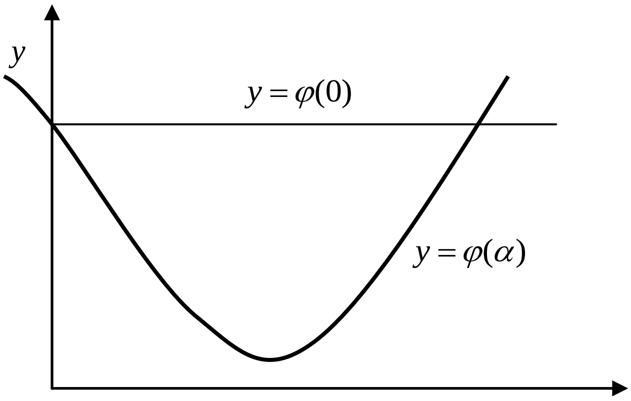

Fig 2.10 Variation of the cost function along the search line

Our $\mathbf{h}$ being a descent direction ensures that
$\varphi'(0) = \mathbf{h}^T\mathbf{F}'(\mathbf{x}) < 0$,
indicating that if α is sufficiently small, we satisfy the descending condition (2.16), which is equivalent to
$\varphi(\alpha) < \varphi(0)$.

Often we are given an initial guess on α, e.g. $\alpha = 1$ with Newton's method. Figure 2.10 illustrates the three different situations that can arise

1. α is so small that the gain in value of the objective function is very small. α should be increased.

2. α is too large: $\varphi(\alpha) \geq \varphi(0)$. Decrease α in order to satisfy the descent condition (2.16)

3. α is close to the minimizer of $\varphi(\alpha)$. Accept this α-value. This gives the smallest local minimizer of φ. If we increase α beyond the interval shown in Fig 2.10, it may well happen that we get close to another local minimum for F.

An *exact line search* is an iterative process producing a series $\alpha_1, \alpha_{2,} \dots$. The aim is to find the true minimizer α_e defined in (2.22) and the algorithm stops when the iterate α_s satisfies $|\varphi'(\alpha_s)| \le \tau |\varphi'(0)|$
where τ is a small, positive number. In the iteration we can use approximates to the variations of $\varphi(\alpha)$ based on the computed values of

$\varphi(\alpha_k) = F(\mathbf{x} + \alpha_k \mathbf{h})$ and $\varphi'(\alpha_k) = \mathbf{h}^T F(\mathbf{x} + \alpha_k \mathbf{h})$.

3.3 Non-Linear Least Squares Problems: Given a non-linear vector function $\mathbf{f} : \mathbb{R}^n \mapsto \mathbb{R}^m$ with $m \ge n$. We want to minimize $\|\mathbf{f}(\mathbf{x})\|$, or equivalently to find

$$\mathbf{x}^* = \arg\min_{\mathbf{x}} \{F(x)\} \tag{2.29a}$$

where

$$F(\mathbf{x}) = \frac{1}{2} \sum_{i=1}^{m} (f_i(\mathbf{x}))^2 = \frac{1}{2} \|\mathbf{f}(\mathbf{x})\|^2 = \frac{1}{2} \mathbf{f}(\mathbf{x})^T \mathbf{f}(\mathbf{x}) \tag{2.29b}$$

Least Squares problems can be solved by general optimization methods, but here special methods are presented that are more efficient. We need following definitions:

Provided that $\mathbf{f}$ has continuous second partial derivatives, we can write its Taylor expansion as

$$\mathbf{f}(\mathbf{x} + \mathbf{h}) = \mathbf{f}(\mathbf{x}) + \mathbf{J}(\mathbf{x})\mathbf{h} + O(\|\mathbf{h}\|^2) \tag{2.30}$$

where $\mathbf{J} \in \mathbb{R}^{m \times n}$ is the Jacobean. This is a matrix containing the first partial derivatives for the function components,

$$(\mathbf{J}(\mathbf{x}))_{ij} = \frac{\partial f_i}{\partial x_j}(\mathbf{x}) \tag{2.31}$$

As regards $F : \mathbb{R}^n \mapsto \mathbb{R}$, it follows from the first formulation in (2.29b) that

$$\frac{\partial F}{\partial x_j}(\mathbf{x}) = \sum_{i=1}^{m} f_i(\mathbf{x}) \frac{\partial f_i}{\partial x_j}(\mathbf{x}) \tag{2.32}$$

Thus the gradient (2.13) is

$$\mathbf{F}'(\mathbf{x}) = \mathbf{J}(\mathbf{x})^T \mathbf{f}(\mathbf{x}) \tag{2.33a}$$

We shall also need the Hessian of F. From (2.32) we see that the element in position (j,k) is

$$\frac{\partial^2 F}{\partial x_j \partial x_k}(\mathbf{x}) = \sum_{i=1}^{m}\left(\frac{\partial f_i}{\partial x_j}(\mathbf{x})\frac{\partial f_i}{\partial x_k}(\mathbf{x}) + f_i(\mathbf{x})\frac{\partial^2 f_i}{\partial x_j \partial x_k}(\mathbf{x})\right) \qquad (2.33b)$$

showing that

$$\mathbf{F}''(\mathbf{x}) = \mathbf{J}(\mathbf{x})^T\mathbf{J}(\mathbf{x}) + \sum_{i=1}^{m} f_i(\mathbf{x})\mathbf{f}_i''(\mathbf{x}) \qquad (2.33c)$$

3.3.1 The Gauss-Newton Method: This is an efficient method based on the implementation of first derivatives of the components of the vector function. It is based on the linear approximation to the components of $\mathbf{f}$ in the neighbourhood of $\mathbf{x}$: For small $\|\mathbf{h}\|$ we see from the Taylor expansion (2.30) and (2.31) that:

$$\mathbf{f}(\mathbf{x}+\mathbf{h}) \simeq l(\mathbf{h}) \equiv \mathbf{f}(\mathbf{x}) + \mathbf{J}(\mathbf{x})\mathbf{h} \qquad (2.34)$$

Inserting this in the definition (2.29) of F we see that

$$F(x+h) \simeq L(\mathbf{h}) \equiv \frac{1}{2} l(\mathbf{h})^T l(\mathbf{h}) = F(\mathbf{x}) + \mathbf{h}^T\mathbf{J}^T\mathbf{f} + \frac{1}{2}\mathbf{h}^T\mathbf{J}^T\mathbf{J}\mathbf{h} \qquad (2.35)$$

The Gauss-Newton step $\mathbf{h}_{gn}$ minimizes $L(\mathbf{h})$.

It is easily seen that the gradient and the Hessian of L are

$$L'(\mathbf{h}) = \mathbf{J}^T\mathbf{f} + \mathbf{J}^T\mathbf{J}\mathbf{h}, \qquad L''(\mathbf{h}) = \mathbf{J}^T\mathbf{J} \qquad (2.36)$$

Comparing with (2.33) shows that $\mathbf{L}'(0) = \mathbf{F}'(\mathbf{x})$. Thus we can find $\mathbf{h}_{gn}$ by solving

$$(\mathbf{J}^T\mathbf{J})\mathbf{h}_{gn} = -\mathbf{J}^T\mathbf{f} \ , \qquad \mathbf{x} := \mathbf{x} + \alpha\mathbf{h}_{gn} \qquad (2.37)$$

where the second relation is a typical step.

3.3.2 The Levenberg-Marquardt Method: Levenberg (1944) and later Marquardt (1963) suggested using a damped Gauss-Newton Method. The step $\mathbf{h}_{lm}$ is defined by the following modification to (2.37),

$$(\mathbf{J}^T\mathbf{J} + \mu\mathbf{I})\mathbf{h}_{lm} = -\mathbf{g} \text{ with } -\mathbf{g} = \mathbf{J}^T\mathbf{f} \text{ and } \mu \geq 0 \qquad (2.38)$$

Here, $\mathbf{J} = \mathbf{J}(\mathbf{x})$ and $\mathbf{f} = \mathbf{f}(\mathbf{x})$. The damping parameter μ has several effects:

1. For all $\mu > 0$ the coefficient matrix is positive definite, and this ensures that $\mathbf{h}_{lm}$ is a descent direction
2. For large values of μ we get
$$\mathbf{h}_{lm} \simeq -\frac{1}{\mu}\mathbf{g} = -\frac{1}{\mu}\mathbf{F}'(\mathbf{x}) \tag{2.39}$$
i.e., a short step in the steepest descent direction. This is good if the current iterate is far from the solution.
3. If μ is very small, then $\mathbf{h}_{lm} \simeq \mathbf{h}_{gn}$, which is a good step in the final stages of the iteration, when $\mathbf{x}$ is close to $\mathbf{x}^*$. If $F(\mathbf{x}^*) = 0$ (or very small), then we can get (almost) quadratic convergence.

Thus the damping parameter influences both the direction as well as size of the step, and this leads us to make a method without a specific line search.

The choice of initial μ-value should be related to the size of the elements in $\mathbf{A}_0 = \mathbf{J}(\mathbf{x}_0)^T \mathbf{J}(\mathbf{x}_0)$, e.g. be letting

$$\mu_0 = \tau.\max_i\{a_{ii}^{(0)}\} \tag{2.40a}$$

where τ is chosen by the user. The updating is controlled by the gain ratio

$$\rho = \frac{F(\mathbf{x}) - F(\mathbf{x} + \mathbf{h}_{lm})}{L(0) - L(\mathbf{h}_{lm})} \tag{2.40b}$$

The stopping criteria for the algorithm can be if the change in $\mathbf{x}$ is small,

$$\| x_{new} - x \| \leq \varepsilon_2 (\| x \| + \varepsilon_2) \tag{2.40c}$$

Finally to avoid infinite loop, we can have the saveguard

$$k \leq k_{\max} \tag{2.40d}$$

Also ε_2 and $k_{\max}$ are chosen by the user.

The algorithm is summarized below:

Algorithm 1.3 Levenberg-Marquardt Method

```
begin
  $k := 0; \nu := 2; \mathbf{x} := \mathbf{x}_0$
  $\mathbf{A} := \mathbf{J}(\mathbf{x})^T \mathbf{J}(\mathbf{x}); \mathbf{g} := \mathbf{J}(\mathbf{x})^T \mathbf{f}(\mathbf{x})$
  $found := (\| x_{new} - x \| \leq \varepsilon_2 (\| x \| + \varepsilon_2)); \mu := \tau * \max\{a_{ii}\}$
  while(not found)and $(k < k_{\max})$
    $k := k + 1; Solve(\mathbf{A} + \mu \mathbf{I})\mathbf{h}_{lm} = -\mathbf{g}$
    if $\| \mathbf{h}_{lm} \| \leq \varepsilon_2 (\| \mathbf{x} \| + \varepsilon_2)$
      $found :=$ true
    else
      $\mathbf{x}_{new} := \mathbf{x} + \mathbf{h}_{lm}$
      $\rho := (F(\mathbf{x}) - F(\mathbf{x}_{new})) / (L(0) - L(\mathbf{h}_{lm}))$
      if $\rho > 0$
        $\mathbf{x} := \mathbf{x}_{new}$
        $\mathbf{A} := \mathbf{J}(\mathbf{x})^T \mathbf{J}(\mathbf{x}); \mathbf{g} = \mathbf{J}(\mathbf{x})^T \mathbf{f}(\mathbf{x})$
        $found := (\| x_{new} - x \| \leq \varepsilon_2 (\| x \| + \varepsilon_2))$
        $\mu := \mu * \max\{\frac{1}{3}, 1 - (2\rho - 1)^3\}; \nu := 2$
      else
        $\mu := \mu * \nu; \nu := 2 * \nu$
end
```

4 Digital Image Correlation

With the introduction of high speed cameras and affordable processing power of today’s computers, an evolution has emerged to use digital image correlation technique or shortly DIC in experimental mechanics to find displacements, strains, stresses and shape measurements. DIC is also appealing thanks to its versatility in terms of the scale of observation. . DIC has been used effectively in biomechanics, fracture mechanics studies and for concrete deformations. A wide range of applications [10-16] of the technique have already indicated the versatility of the method.

4.1 Governing Equations: The principle of image correlation is derived from the “passive advection” of the local texture of two gray level images. The displacement field $\mathbf{u}$ between the reference image f and the “deformed” image g induced by this advection is to be estimated as accurately as possible.

The local form of the principle reads

$$f(\mathbf{x}) = g(\mathbf{x} + \mathbf{u}(\mathbf{x})) \tag{2.41}$$

This equation cannot be fulfilled pixelwise and thus a weak form is genereally formulated through the minimization of the global quantity

$$\eta^2 = \iint_\Omega \phi^2(\mathbf{x}) d\mathbf{x} \tag{2.42}$$

where the local error density, $\phi(\mathbf{x})$, is

$$\phi^2(\mathbf{x}) = [g(\mathbf{x} + \mathbf{u}(\mathbf{x})) - f(\mathbf{x})]^2 \tag{2.43}$$

We directly minimize the functional η^2 for arbitrary displacement fields. Therefore ϕ is used as a local error indicator for the correlation procedure. This indicator gives a straightforward way of estimating the quality of the results.

4.2 Non-Linear Problem and noise reduction: The equation (2.41) is an ill-posed problem that cannot be fulfilled pixelwise and due to the presence of local minima as the texture is nearly irregular. Also there is likelihood of the presence of noise since we are dealing with digital images and noise can come from poor speckle, camera configuration or low quality sensors as well as numerical techniques being used during the correlation procedure. Thus to circumvent the non-linear aspects of the problem and to reduce noise in the determination of displacement, following strategies are adopted:

4.2.1 Newton Algorithm: A Newton iterative procedure is elaborated to circumvent the non-linear aspects of the problem. Let us denote by $\mathbf{u}^i$ the approximation of the displacement field at iteration i. The problem is recast in the following form: find the displacement increment $d\mathbf{u} = \mathbf{u}^{i+1} - \mathbf{u}^i$ by minimizing η such that

$$\eta^2 = \iint_\Omega [g(\mathbf{x} + \mathbf{u}^i(\mathbf{x}) + d\mathbf{u}(\mathbf{x})) - f(\mathbf{x})]^2 d\mathbf{x} \tag{2.44}$$

Assuming a small increment of the solution, the first term is linearized to provide

$$\eta^2 = \iint_\Omega [g(\mathbf{x} + \mathbf{u}^i(\mathbf{x})) + d\mathbf{u}(\mathbf{x}).\nabla g(\mathbf{x} + \mathbf{u}^i(\mathbf{x})) - f(\mathbf{x})]^2 d\mathbf{x} \tag{2.45}$$

The motion has to be sufficiently small for the Taylor expansion to be valid and we can see that DIC is an ill-posed problem since the displacement can only be measured along the intensity gradient.

The right-hand side is now expressed in an appropriate way

$$\begin{aligned}\eta^2 = &\iint_\Omega [d\mathbf{u}(\mathbf{x}).\nabla g(\mathbf{x} + \mathbf{u}^i(\mathbf{x}))]^2 d\mathbf{x} + 2\iint_\Omega d\mathbf{u}(\mathbf{x}).\nabla g(\mathbf{x} + \mathbf{u}^i(\mathbf{x}))[g(\mathbf{x} + \mathbf{u}^i(\mathbf{x})) - f(\mathbf{x})] d\mathbf{x} \\ &+ \iint_\Omega [g(\mathbf{x} + \mathbf{u}^i(\mathbf{x})) - f(\mathbf{x})]^2 d\mathbf{x}\end{aligned} \tag{2.46}$$

As mentioned earlier, the displacement field is decomposed over a set of functions $\Psi_n(\mathbf{x})$.

The approximation of the displacement field then reads

$$\mathbf{u}(\mathbf{x}) = \sum_{n \in N} a_n \psi_n(\mathbf{x}) \tag{2.47}$$

where $(a_n)_{n \in N}$ is the set of unknown associated with the chosen interpolation functions (N being a set of integers identifying the interpolation functions). By adopting matrix-vector notations, the minimization of (2.46) is recast as a linear system

$$M^i d\mathbf{u} = \mathrm{b}^i \tag{2.48}$$

where M^i is a "mass"- like matrix defined as

$$\begin{aligned} M^i_{nm} &= \iint_\Omega (\psi_m . \nabla g(\mathbf{x} + \mathbf{u}^i(\mathbf{x})))(\psi_n . \nabla g(\mathbf{x} + \mathbf{u}^i(\mathbf{x}))) d\mathbf{x} \\ [\mathbf{M_{DIC}}] &= [\mathbf{N}]^T [\nabla \mathbf{G}][\nabla \mathbf{G}][\mathbf{N}] \end{aligned} \tag{2.49}$$

and b^i is the "force" vector

$$\begin{aligned} \mathrm{b}^i_n &= \iint_\Omega (\psi_n . \nabla g(\mathbf{x} + \mathbf{u}^i(\mathbf{x})))[f(\mathbf{x}) - g(\mathbf{x} + \mathbf{u}^i(\mathbf{x}))] d\mathbf{x} \\ \{\mathbf{b_{DIC}}\} &= [\mathbf{N}]^T [\nabla \mathbf{G}][\mathbf{F} - \mathbf{G}] \end{aligned} \tag{2.50}$$

where $[\mathbf{N}]$ is a matrix that collects the value of the basis functions at the pixel location $\mathbf{x}$, $[\nabla \mathbf{G}]$ is a diagonal matrix that collects the value of $\nabla g(\mathbf{x} + \mathbf{u}^i(\mathbf{x}))$ and $[\mathbf{F} - \mathbf{G}]$ a vector containing the values of $[f(\mathbf{x}) - g(\mathbf{x} + \mathbf{u}^i(\mathbf{x}))]$.

The solution is then updated and the process is repeated until a convergence criterion associated with a given norm is reached.

To improve convergence we can replace $\nabla \mathbf{G}$ by $\nabla \mathbf{F}$ because when convergence is reached both are equal and we don't need to calculate $\nabla \mathbf{G}$ at each iteration. We thus have

$$M^i_{nm} = [\mathbf{N}]^T [\nabla \mathbf{F}][\nabla \mathbf{F}][\mathbf{N}] \tag{2.51}$$

and

$$\mathrm{b}^i_n = [\mathbf{N}]^T [\nabla \mathbf{F}][\mathbf{F} - \mathbf{G}] \tag{2.52}$$

4.2.2 FE-DIC: Having an identical description for the displacement field during the measurement stage and for the numerical simulation is the key for reducing the noise or uncertainty propagation in the identification chain. During the latter, there is usually a difference between the kinematic hypotheses made during the measurement and simulation stages and this can make comparison difficult. This can be avoided by using FE shape functions in equation (2.47). Since the image is naturally partitioned into pixels, it is appropriate to choose a square or rectangular shape for each element. The limiting element size is one pixel.

4.2.3 Multi-grid solver: The solver must be able to avoid local minima. A multi-grid finite element strategy is utilized for this purpose. The region of interest of the reference image is decomposed into square elements Ω_e of pixels. The vertices of Ω_e are the nodes N_e that support finite element shape functions $(N_j)_{j \in N_e}$.

For the Multi-grid strategy, coarser grids are derived from the original one. At those grid levels, the elements consist of a set of "grains" (at the finest scale a grain is a pixel). The size of the grains is multiplied by a factor of 2 in each direction from a certain grid level to the next coarser one. Using this notation the element size in terms of "grains" is the same for all grids. This coarse graining strategy allows for a regularization of the texture of the images. This regularization stage allows for filtering the short wavelengths of the texture at the coarser grids of the algorithm. These high frequency modes are then gird by grid reintroduced in the calculation. Also we don't need V or W cycles instead only one way down from the coarsest to the finest would be sufficient to find the global minimum [17].

4.3 Advantages of using full-field measurements for identification: Full field measurements provide us with rich experimental data (typically 1000 to 10,000 independent measurement points) that is not available with the conventional methods of measuring global responses of material specimens.

In standard identification procedure, we have standardized geometries (e.g., a dog-bone shape) and boundary conditions to give uniform state of stress and strain. If a homogeneous state of stress and strain does not exist, it is only possible to determine the average strain value over the gage length region with this procedure and not the true properties of the material at a point. With this assumption fulfilled we may use simple analytical expressions to relate the stress and strain and find the unknown constitutive parameters of the mechanical material behaviour model. As was explained in the introduction this is not true of the actual situation in most engineering applications. Hence its use is limited. But with Full field measurements, we can analyze complex experiments with non-homogeneous strain states and non-standardized specimen geometries to give us more reliable estimates of constitutive parameters.

These complex tests have yet another advantage: in general several standard tests are needed to determine all unknown material parameters. As a consequence of the parameters being evaluated sequentially, values of parameters may depend upon the order in which they were determined [59]. However, the heterogeneous stress and strain fields, resulting from the complex material tests provide much more information and, hence, allow the simultaneous identification of several material parameters. Thus full-field measurements allow greater accuracy, flexibility and speed. Moreover, larger sets of constitutive parameters can be identified.

However, identification of parameters using this type of approach requires suitable computational strategies to analyze experimental data. The following section gives an overview of the available strategies.

5 Identification from Digital Images [19, 20, 42]:

The aim of the present section is to present an overview of recently-developed identification approaches specifically aimed at analyzing field measurements. All of these strategies can be termed as inverse strategies since they are inverse of the direct problem in mechanics of finding the displamcent, stress and strain.

Govening Equations: An elastic body whose undeformed configuration occupies the domain Ω is governed by three sets of equations, namely the equilibrium equations (having for simplicity assumed the absence of body forces)

$$\begin{cases} div\sigma = 0 \text{ in } \Omega, \\ \boldsymbol{\sigma}.\boldsymbol{n} = \bar{\boldsymbol{T}} \quad \text{on } S_f \end{cases} \tag{2.53a}$$

the kinematic compatibility equations

$$\begin{cases} \boldsymbol{\varepsilon} = \frac{1}{2}(\nabla\mathbf{u} + \nabla^T\mathbf{u}) \text{ in } \Omega \\ \mathbf{u} = \bar{\mathbf{u}} \text{ on } S_u \end{cases} \tag{2.53b}$$

and the constitutive equation

$$\boldsymbol{\sigma} = \boldsymbol{A} : \boldsymbol{\varepsilon} \text{ in } \Omega \tag{2.53c}$$

In these equations $\mathbf{u}$ denotes the displacement vector, $\boldsymbol{\varepsilon}$ the infinitesimal strain vector, $\boldsymbol{\sigma}$ the Cauchy stress tensor and $\boldsymbol{n}$ the outward normal vector. Over-lined quantities are prescribed as static or kinematic boundary conditions. Components of the Hooke tensor $\boldsymbol{A}$

can be either constant (homogeneous material) or point-dependent (heterogeneous material).

Introducing sets S and C of statically admissible stress fields and of kinematically admissible displacement fields, respectively, i.e.:

$$S\bar{\boldsymbol{T}} = \{\boldsymbol{\tau} \in \upsilon_\sigma, \text{div}\boldsymbol{\tau} = 0 \text{ (in } \Omega) \text{ and } \boldsymbol{\tau}.\boldsymbol{n} = \bar{\boldsymbol{T}}(\text{on } S_f)\} \tag{2.53d}$$

$$C(\bar{\mathbf{u}}) = \{\boldsymbol{v} \in \upsilon_u, \boldsymbol{v} = \bar{\mathbf{u}} \text{ (on } S_u)\} \tag{2.53e}$$

where υ_σ is the set of symmetric second-order tensor fields $\boldsymbol{\tau}$ that are, together with $\text{div}\boldsymbol{\tau}$, square integrable over Ω, and υ_u is the set of vector (displacement) fields defined over Ω.

Identification Problem: Constitutive parameter identification is often referred to as an inverse problem. The lack of information about $\boldsymbol{A}$ must be compensated with overdetermined data. Thus in addition to the boundary conditions, supplementary information resulting from measurements must be available. Such additional information may take many forms, and is here assumed to consist of kinematic field measurements.

In many practical cases, the primary unknown of the identification problem is a vector $\boldsymbol{\theta} = \{\theta_1, ..., \theta_m\}$ of M constitutive parameters entering the elasticity tensor: $\boldsymbol{A} = \boldsymbol{A}(\theta)$. We thus have the following relation:

$$\tilde{\boldsymbol{K}}(\boldsymbol{\theta})\boldsymbol{U} = \boldsymbol{R} \tag{2.54}$$

When the parameterization $\boldsymbol{A}(\theta)$ is linear in $\boldsymbol{\theta}$ we can write:

$$\boldsymbol{A} = \sum_{i=1}^{M} \boldsymbol{A}_i\theta_i \qquad \tilde{\boldsymbol{K}}(\boldsymbol{\theta}) = \sum_{i=1}^{M} \tilde{K}_i\theta_i \tag{2.55}$$

5.1 The Finite Element Model Updating Method (FEMU) [26]: The goal of FEMU approach is to identify the constitutive parameters $\boldsymbol{\theta}$ by exploiting equation (2.54), or similar equations stemming from a FEM model of the sample. Basically, the FEMU approach is based on the minimizing the discrepancy between either known and predicted forces (FEMU-F) or measured and predicted displacement fields (FEMU-U).

5.1.1 The Force Balance Method (FEMU-F): It is based on the experimental availability of all the nodal displacements $\overset{\wedge}{\boldsymbol{U}}$ and prescribed forces $\overset{\wedge}{\boldsymbol{R}}$. Substituting the known quantities $\overset{\wedge}{\boldsymbol{U}}$ and $\overset{\wedge}{\boldsymbol{R}}$ into equation (2.54) yields a set of equations used as a basis for recovering the constitutive unknowns $\boldsymbol{\theta}$. The FEMU-F approach consists in minimizing least-squares functional of the form

$$J_F(\boldsymbol{\theta}) = \frac{1}{2}(\overset{\wedge}{\boldsymbol{R}} - \tilde{\boldsymbol{K}}(\boldsymbol{\theta})\overset{\wedge}{\boldsymbol{U}})^T \boldsymbol{W}_F (\overset{\wedge}{\boldsymbol{R}} - \tilde{\boldsymbol{K}}(\boldsymbol{\theta})\overset{\wedge}{\boldsymbol{U}}) \tag{2.56}$$

where $\boldsymbol{W}_F$ is a (symmetric, positive definite) weighting matrix.

5.1.2 The Displacement Method (FEMU-U): In many cases, the displacements are only partially known, and the force method cannot be applied. The displacement method has hence been developed as an alternative. We minimize the following functional

$$J_{\mathrm{U}}(\boldsymbol{\theta}; \bar{w}) = \frac{1}{2}(\overset{\wedge}{\boldsymbol{U}} - \boldsymbol{U}(\boldsymbol{\theta}; \bar{w}))^T \boldsymbol{W}_{\mathrm{U}} (\overset{\wedge}{\boldsymbol{U}} - \boldsymbol{U}(\boldsymbol{\theta}; \bar{w})) \tag{2.57}$$

where $\boldsymbol{U}(\boldsymbol{\theta}; \bar{w})$ is the solution to a well-posed direct elasticity problem, $\bar{w}$ symbolizes the available information on boundary conditions, and $\boldsymbol{W}_{\mathrm{U}}$ is a (symmetric, positive definite) weighting matrix.

The misfit functions (2.56) and (2.57) are two of other variants that are possible [21-23]. FEMU can be applied to any kind of over determined data. Minimization of J_F or J_{U} is often carried out by Gauss-Newton or Levenberg-Marquardt methods. Finally, the direct solution $\boldsymbol{U}(\boldsymbol{\theta})$ may be set up using methods other than FEM e.g. the finite difference method.

FEMU has been applied to the identification of parameters driving the elasto-plastic behaviour of metals, with promising results, from tensile tests on notched or drilled specimens giving rise to heterogeneous stress states for which displacements were measured using DIC and the total tensile force was known. Various constitutive models have been tested (with linear or non linear hardening). The boundary conditions are provided by the DIC patterns located at the boundary of the measurement zone (near the clamps).

5.2 The Constitutive Equation Gap Method [19]: The CEG measures the distance between a given stress field $\boldsymbol{\tau}$ and another stress field computed through a constitutive model from a given displacement field $\boldsymbol{v}$.If the constitutive model is linearly elastic, then the CEG between the fields $\boldsymbol{\tau}$ and $\boldsymbol{v}$ is defined by

$$\Xi(\boldsymbol{v},\ \boldsymbol{\tau}, \boldsymbol{A})=\frac{1}{2}\int_{\Omega}(\boldsymbol{\tau}-\boldsymbol{A}:\boldsymbol{\varepsilon}[\boldsymbol{v}]):\boldsymbol{A}^{-1}:(\boldsymbol{\tau}-\boldsymbol{A}:\boldsymbol{\varepsilon}[\boldsymbol{v}])dV \qquad (2.58)$$

where the elasticity tensor $\boldsymbol{A}$ is allowed to be heterogeneous.

Considering a constitutive parameter identification problem, where for instance the elasticity tensor $\boldsymbol{A}$ is to be identified, one may alter definitions (2.53d) and (2.53e) of the sets of admissible fields so as to include all available experimental information about displacements and stresses. Based on such adjusted definitions, $\boldsymbol{A}$ can be sought so as to minimize the CEG:

$$\boldsymbol{A}=\arg\min_{\boldsymbol{A}^{*}\in \mathrm{A}} J(\boldsymbol{A}^{*}) \text{ with } J(\boldsymbol{A}^{*})=\min_{(\boldsymbol{v},\boldsymbol{\tau})\in C\times S}\Xi(\boldsymbol{v},\boldsymbol{\tau},\boldsymbol{A}^{*}) \qquad (2.59)$$

where A is the set of admissible elasticity tensor fields.

5.3 The Virtual Field Method [19]: This approach is applicable to situations where the strain field is experimentally known in Ω:

$$\boldsymbol{\varepsilon}=\overset{\wedge}{\boldsymbol{\varepsilon}} \text{ in } \Omega \qquad (2.60)$$

where $\overset{\wedge}{\boldsymbol{\varepsilon}}$ is known from full-field measurements (possibly through differentiation of a measured displacement field). No limitations are put on the loading conditions, which are also assumed to be known. Assuming that no body forces are applied and that boundary conditions are as stipulated in equations (2.53), the principle of virtual work takes the form

$$-\int_{\Omega}\boldsymbol{\sigma}:\boldsymbol{\varepsilon}[\mathbf{u}^{*}]dV+\int_{S_f}T\mathbf{u}^{*}dS=\int_{\Omega}\rho\ddot{\mathbf{u}}.\mathbf{u}^{*}dV \qquad (2.61)$$

for any $\mathbf{u}^{*}\in C(0)$.

The VFM basically consists of exploiting identity (2.61) with particular choices of virtual fields, tailored to specific identification problem at hand.

First a constitutive model is assumed for the material. For instance, one has $\boldsymbol{\sigma}=\boldsymbol{A}(\theta):\overset{\wedge}{\boldsymbol{\varepsilon}}$ if elastic moduli are to be identified. Then, virtual fields are chosen. Each virtual field substituted in (2.61) yields one scalar equation. The constitutive parameters are then sought as solutions to a set of such equations.

5.4 The Equilibrium Gap Method [19]: This approach has been developed for cases where the elastic heterogeneity takes the form of a scalar field $C(\boldsymbol{x})$, i.e.

$$\boldsymbol{A}(\boldsymbol{x})=C(\boldsymbol{x})\boldsymbol{A}_0 \qquad (2.62)$$

(where $\boldsymbol{A}_0$ is given and corresponds to a reference medium) with the aim of identifying this contrast field from the displacement field measured in Ω.

The basic assumption is that the displacement data is available on a measurement grid, which is usually regular. A FEM mesh is then set up so that its nodes coincide with the measurement points. Assuming a constant contrast $C(\boldsymbol{x})=C_e$ over each finite element, the stiffness matrix of element E_e has the form

$$[\boldsymbol{K}_e](C) = C_e[\boldsymbol{K}_{e0}] \tag{2.63}$$

where $[\boldsymbol{K}_{e0}]$ is the element stiffness matrix for the reference medium endowed with moduli $\boldsymbol{A}_0$.Then, the FEM equilibrium equation at the m-th DOF (assumed to be located at a node which does not support any external load) have the form.

$$\sum_{e|m\in E_e} C_e\{e_m\}^T[\boldsymbol{K}_{e0}]\{\mathbf{u}_e\} = 0 \tag{2.64}$$

where $\{\mathbf{u}_e\}$ is the vector of DOFs on element E_e, $\{e_m\}$ is the m-th unit vector, and the summation runs over the elements which share the m-th DOF. Equations (2.64) provide the basis upon which the contrasts C_e are identified, the cofactor of each C_e being known by virtue of the assumption that a full-field kinematic measurement is available.

5.5 The Reciprocity Gap Method [19]: The RGM primarily concerns situations where mechanical field measurements are available on the boundary. Let $(\overset{\wedge}{\mathbf{u}}, \overset{\wedge}{\boldsymbol{T}})$ denote known displacements and tractions on the boundary. From the virtual work principle, a reciprocity gap functional can then be defined. Consider for the sake of illustration the case where the measurements have been taken on an elastic body Ω with boundary S endowed with the elasticity tensor $\boldsymbol{A}(\boldsymbol{x})$, which is to be identified. Besides, let $\mathbf{u}^*$ denote the displacement field induced by a traction distribution $\boldsymbol{T}^*$ on S on a body with the same geometry but characterized by the trial elasticity tensor $A^*(\boldsymbol{x})$ (any such auxiliary state is referred to as an 'adjoint state'). On combining the identities obtained from the virtual work principle applied in turn to the experimental state and the adjoint state one obtains

$$\int_\Omega \varepsilon[\mathbf{u}] : [\boldsymbol{A} - \boldsymbol{A}^*] : \varepsilon[\mathbf{u}^*] dV = \int_{\partial\Omega} (\overset{\wedge}{\boldsymbol{T}}.\mathbf{u}^* - \boldsymbol{T}^*.\overset{\wedge}{\mathbf{u}}) dS \equiv R(\boldsymbol{A}^*, \mathbf{u}; \mathbf{u}^*) \tag{2.65}$$

For any adjoint state $\mathbf{u}^*$, the reciprocity gap $R(\boldsymbol{A}^*, \mathbf{u}^*)$ is thus a known function of the experimental data $(\overset{\wedge}{\mathbf{u}}, \overset{\wedge}{\boldsymbol{T}})$. One must have

$$R(\boldsymbol{A}^*, \mathbf{u}, \mathbf{u}^*) = 0 \tag{2.66}$$

This equation thus yields an independent scalar relationship on the unknown distribution $\boldsymbol{A}^*$, or on the parameters involved in its definitions, for any choice of adjoint state.

Theory

In this section we shall consider the development of the strategy that allows us to include 3D effects in our material model. The strategy has its roots in the inverse strategy of FEMU discussed in the last section. The following pages explain the theory behind the procedure of identification.

1. Finite Element Model Updating based Procedures

As discussed earlier many variants of FEMU exist depending on different cost functions Φ and different techniques for updating the parameters. The following figure shows the principle of FEMU based procedures.

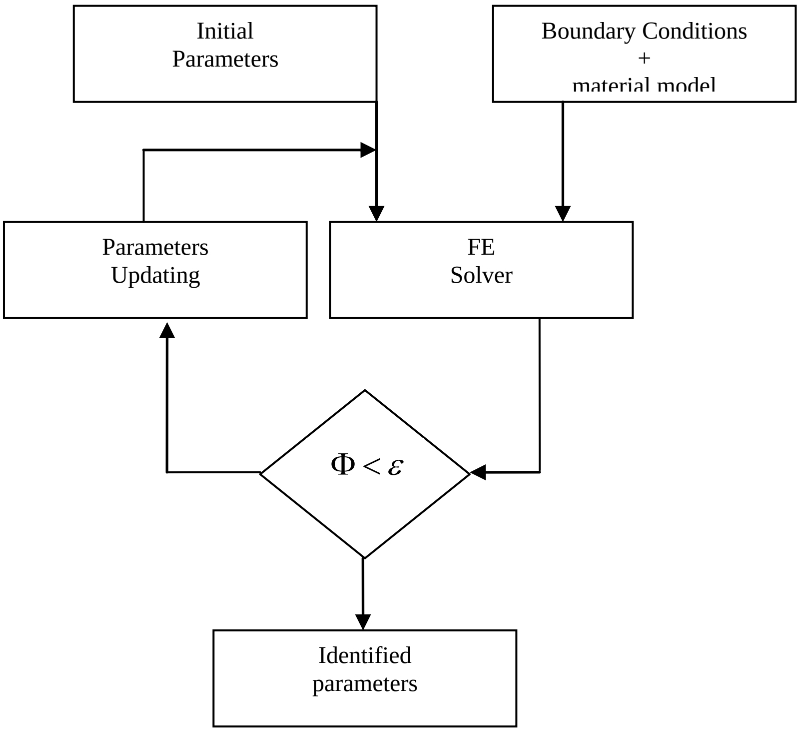

First we need to extract the boundary conditions to be applied on the FE model. However, if the boundary conditions contain noise, the strategy will in turn be affected by noise. The identified parameter will then be sensitive to mesh size and we will have higher noise levels. So we need strategy for identification that is independent from the use of boundary conditions altogether. Integrated Mechanical Image Correlation (I-MIC) is thus adopted and explained in the following pages. To include 3D effects, changes have been done on the original I-MIC approach proposed by Réthoré [7]. The modified I-MIC is transformed for the use in mono and stereo image correlation.

1.1 Mechanical Image Correlation (MIC): To reduce noise in the identification chain, the idea is to try and minimize the mismatching of the images directly from the constitutive parameters. The cost function used is:

$$\mathbf{\Lambda} = \text{Arg Min} \sum_{p \in ROI} [\, f(\mathbf{x}_p) - g(\mathbf{x}_p + \mathbf{v}(\mathbf{x}_p))]^2 \tag{3.1}$$

where $\mathbf{x}_p$ is the pixel p coordinate on the image.

In this strategy, the deformed image g is corrected by $\mathbf{v}$ which is the simulated displacement using the current estimation of the constitutive parameters $\mathbf{\Lambda}$ and appropriate boundary conditions. We obtain the solution increment from:

$$[\mathbf{M}_{\mathbf{MIC}}]\{\mathrm{d}\mathbf{\Lambda}\} = \{\mathbf{b}_{\mathbf{MIC}}\} \tag{3.2}$$

with

$$[\mathbf{M}_{\mathbf{MIC}}] = \left[\frac{\Delta\mathbf{G}}{\Delta\mathbf{\Lambda}}\right]^T \left[\frac{\Delta\mathbf{G}}{\Delta\mathbf{\Lambda}}\right] \tag{3.3}$$

$\mathbf{G}$ is the vector containing the grey level values of the deformed image g. $\Delta\mathbf{G}$ is linearlized and written as $\Delta\mathbf{G}[\mathbf{N}][\Delta\mathbf{V}]$. The matrix $[\mathbf{M}_{\mathbf{MIC}}]$ finally recasts in the following form:

$$[\mathbf{M}_{\mathbf{MIC}}] = \left[\frac{\Delta\mathbf{V}}{\Delta\mathbf{\Lambda}}\right]^T [\mathbf{N}]^T [\nabla\mathbf{G}][\nabla\mathbf{G}][\mathbf{N}] \left[\frac{\Delta\mathbf{V}}{\Delta\mathbf{\Lambda}}\right] = \left[\frac{\Delta\mathbf{V}}{\Delta\mathbf{\Lambda}}\right]^T [\mathbf{M}_{\mathbf{DIC}}] \left[\frac{\Delta\mathbf{V}}{\Delta\mathbf{\Lambda}}\right] \tag{3.4}$$

where $\mathbf{V}$ is the solution vector of a mechanical simulation run with the constitutive parameters $\mathbf{\Lambda}$ and the appropriate boundary conditions obtained from DIC. $\frac{\Delta\mathbf{V}}{\Delta\mathbf{\Lambda}}$ collects the variation of the simulated mechanical solution $\mathbf{V}$ with respect to the constitutive parameters $\mathbf{\Lambda}$.

The vector $\{\mathbf{b}_{\mathbf{MIC}}\}$ is:

$$\{\mathbf{b}_{\mathbf{MIC}}\} = \left[\frac{\Delta\mathbf{V}}{\Delta\mathbf{\Lambda}}\right]^T [\mathbf{N}]^T [\nabla\mathbf{F}][\mathbf{F} - \mathbf{G}(\mathbf{\Lambda})] \tag{3.5}$$

when the same modification as for DIC is adopted, i.e. $\nabla\mathbf{G}$ is substituted by $\nabla\mathbf{F}$. Solving this system, the constitutive parameters increment is directly obtained from the minimization of the mismatching between the two images.

To see the performance of MIC, Réthoré [7] has identified steel plate Poisson's ratio and analysed the effect of different mesh sizes on the identification. The analysis shows that MIC is independent of mesh size when we use the boundary conditions obtained via DIC analysis with a mesh size corresponding to least noise levels. This optimum noise level is achieved for element size of 200 pixel-elements. However, if current element size is used to extract the displacement boundary conditions, then we see that the results are not independent of the mesh size. Thus it is evident in Figure 3.1 that when the MIC analysis is performed using boundary conditions coming from 200 pixel-DIC analysis with least noise amplitude, the identified Poisson's ratio is independent of the mesh size used in MIC. On the other hand, when MIC analysis is performed by using boundary conditions coming from DIC analysis using the same element size in DIC as that of MIC, noisy boundary conditions affect the identification procedure and Poisson's ratio then becomes sensitive to mesh size used in MIC. This confirms the analysis of Avril and Pierron [20] who state that the maximum likelihood set of parameters can only be obtained if the boundary conditions used to obtain $\mathbf{V}$ are not affected by noise.

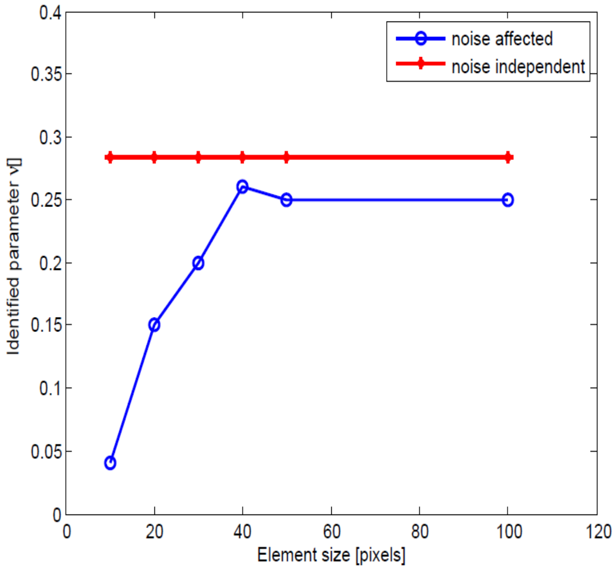

Fig.3.1 Evolution of the identified Poisson's ratio as a function of the element size.

To circumvent this drawback, we consider another strategy independent of boundary conditions in the following section.

1.2 The Integrated-Mechanical Image Correlation (I-MIC): We saw in the previous section how the use of boundary conditions affects the identification process and leads to a strategy sensitive to mesh size. The commonality in both FEMU and MIC is the use of the $\mathbf{V}$ field. This field is obtained from a numerical simulation of a mechanical problem and thus utilises boundary conditions. To avoid the usage of boundary conditions altogether, we propose a strategy that reduces the two step procedure of FEMU and MIC into a single step algorithm. Instead of only obtaining displacement field from images and then using it as boundary condition for a mechanical simulation to extract the material parameters, we tend to extract both the displacement field as well as material parameters from the images.

For this purpose the following cost function is proposed:

$$\{\mathbf{U},\mathbf{\Lambda}\} = Arg\ Min\left(\frac{1}{m_o}\{\mathbf{F}-\mathbf{G}(\mathbf{U},\mathbf{\Lambda})\}^T\{\mathbf{F}-\mathbf{G}(\mathbf{U},\mathbf{\Lambda})\} + \left(\frac{1}{\alpha}-1\right)\frac{1}{k_o}\{\bar{\mathbf{F}}_{\text{int}}(\mathbf{U},\mathbf{\Lambda})\}^T\{\bar{\mathbf{F}}_{\text{int}}(\mathbf{U},\mathbf{\Lambda})\}\right) \tag{3.6}$$

“Integrated” refers to the fact that in this strategy the proposed material behaviour and the balance of momentum are directly integrated into the correlation algorithm. In this equation, the finite element decomposition presented previously in equation (2.47) is adopted so that the nodal displacement vector $\mathbf{U}$ is searched for. $\bar{\mathbf{F}}_{\text{int}}$ is the vector that collects the internal forces for each DOF except those concerned with Dirichlet or Neumann boundary conditions. m_o and k_o are normalization constants that allow us to mix the two contributions of eqn (3.6) with the use of penalty parameter α.

The cost function has two contributions: Optical and Mechanical. The first contribution (on the left of the + sign) concerns the solution of DIC problem. The second contribution (on the right of + sign) is related to the fulfilment of the balance of momentum equations by the displacement field. It is termed mechanical in the sense because it doesn’t have any input from the grey levels of the images unlike the first contribution which is termed optical. The two contributions cannot reach their minimum for the same displacement field which is the reason why the mechanical part is used as a penalty term. α is related to the mechanical filtering of the cut-off wave length of the mechanical filtering provided by the penalty term. The short wavelengths of the displacement solution are dominated by the mechanical contribution whereas the large wavelengths remain governed by the DIC contribution. This filtering that is efficient in noise removal from permissible displacement solution fields was first introduced in Réthoré et al [53].

Neither the knowledge of external load applied to the sample nor displacement boundary conditions are required in this strategy. Thus without the use of boundary conditions, the response of the method is robust with respect to the noise that can affect the displacement field on the boundary. It is also important to note that static quantities, i.e, external loads are not used in this approach. The global response of the specimen that should correspond to these loads can be estimated a posteriori from the displacement field and the material parameters. The ratio between the estimated and actual loads can then be used for the calibration of the model parameters.

Application to Elasto-Plastic Law: Since we are not using the external loads in this strategy, the application of I-MIC to non-linear constitutive laws is not straight forward. We only utilize Dirichlet boundary conditions in the elasto-plastic simulation by prescribing the displacement field obtained from DIC.

From a virtual testing procedure that will be detailed in the next sections, it was observed that the prescribed displacement is not affecting the material parameter identification. In other words the parameters of the elasto-plastic constitutive law have a small influence on the displacement field. For example when the magnitude of the prescribed displacement varies from 1 to 2, the change in the identified yield stress is not appreciable as shown in the figure below:

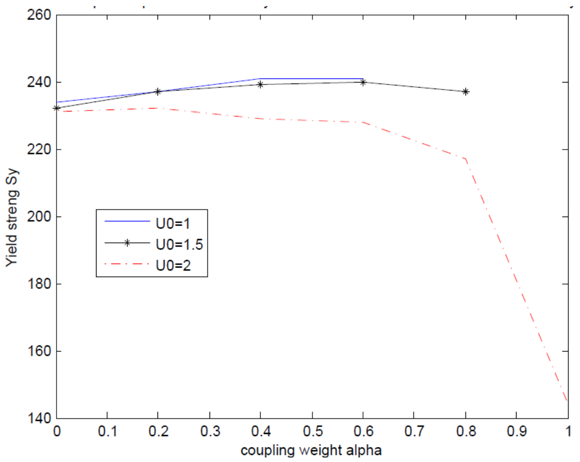

Fig.3.2. Effect of coupling weight α and different amplitude of applied forces on identified yield stress in virtual testing using I-MIC.

Thus, the results obtained by I-MIC for the identification of elasto-plastic law were erroneous. As a remedy we tend to prescribe force instead of displacement for our numerical simulation. Thus, in the present case we will be using displacement that is dependent on the force vector. The strategy employed to find this force vector numerically is also explained in the following sections.

1.3 The Modified I-MIC approach: Thus to make I-MIC suitable for elasto-plastic laws, it is clear that we need to invoke static quantities, e.g., external loads. First the new I-MIC formulation is described, and then details are provided on the important steps of the methodology. For the sake of clarity, we first focus on a two-dimensional case where only one deformed image coming from one camera is available.

In the original I-MIC formulation [7], the mechanical constraints were obtained by the Equilibrium Gap Method ([5] and [39]) as shown in equation (3.6). It does not involve the contribution of the boundary nodes. It has been shown to be an advantage in reducing the effect of noise but as mentioned previously this specificity is the reason why the approach fails for more general constitutive laws. Keeping in mind that the experimental tests are not perfect and that they may contain experimental noise due to various factors like signal to noise ratio of the test equipment, the external loads applied on the non-free boundary of the specimen is a priori unknown. The external force vector is estimated by a different strategy.

Also, instead of using $\bar{\mathbf{F}}_{\text{int}}$, a balance between the work of the external forces, collected in $\mathbf{F}_{ext}$, and the internal work is adopted. Thus in the new modified strategy, the cost function becomes:

$$\{\mathbf{U},\mathbf{\Lambda}\} = Arg\ Min\left(\frac{1}{m_o}\{\mathbf{F}-\mathbf{G}(\mathbf{U},\mathbf{\Lambda})\}^T\{\mathbf{F}-\mathbf{G}(\mathbf{U},\mathbf{\Lambda})\}+\left(\frac{1}{\alpha}-1\right)\frac{1}{k_o}\{\mathbf{U}\}^T\{\mathbf{F}_{ext}-\mathbf{F}_{\text{int}}(\mathbf{U},\mathbf{\Lambda})\}\right) \quad (3.7)$$

From this equation it is clear that the mechanical part of the residual has a linear dependence on $\mathbf{U}$ unlike the optical part. An iterative resolution strategy is therefore employed.

If $d\mathbf{U}$ is the solution increment between two successive iterations, we have:

$$\{\mathbf{G}(\mathbf{U}+d\mathbf{U})\}=\{\mathbf{G}(\mathbf{U},\mathbf{\Lambda})+[\nabla\mathbf{G}]^T[\mathbf{N}]\{d\mathbf{U}\} \tag{3.8}$$

and

$$\{\mathbf{F}_{\text{int}}(\mathbf{U}+d\mathbf{U},\mathbf{\Lambda})\}=\{\mathbf{F}_{\text{int}}(\mathbf{U},\mathbf{\Lambda})\}+[\frac{\delta\mathbf{F}_{\text{int}}}{\delta\mathbf{U}}]\{d\mathbf{U}\} \tag{3.9}$$

Introducing these expressions in equation (3.7), the stationarity with respect to $d\mathbf{U}$ is used to obtain

$$[\mathbf{M}_{I-MIC}]\{d\mathbf{U}\}=\{\mathbf{b}_{I-MIC}\} \tag{3.10}$$

where

$$[\mathbf{M}_{I-MIC}]=\frac{1}{m_o}[\mathbf{N}]^T[\nabla\mathbf{F}][\nabla\mathbf{F}][\mathbf{N}]+\left(\frac{1}{\alpha}-1\right)\frac{1}{k_o}[\mathbf{K}]$$

$$=\frac{1}{m_o}[\mathbf{M}_{DIC}]+\left(\frac{1}{\alpha}-1\right)\frac{1}{k_o}[\mathbf{K}] \tag{3.11}$$

and

$$\begin{aligned}[\mathbf{b}_{I-MIC}]&=\frac{1}{m_o}[\mathbf{N}]^T[\nabla\mathbf{F}][\mathbf{F}-\mathbf{G}]+\left(\frac{1}{\alpha}-1\right)\frac{1}{k_o}[\mathbf{F}_{ext}-\mathbf{F}_{\text{int}}]\\&=\frac{1}{m_o}[\mathbf{b}_{DIC}]+\left(\frac{1}{\alpha}-1\right)\frac{1}{k_o}[\mathbf{F}_{ext}-\mathbf{F}_{\text{int}}]\end{aligned} \tag{3.12}$$

In these equations, we replace $\nabla\mathbf{G}$ which depends on the current solution vector $\mathbf{U}$ by $\nabla\mathbf{F}$ and $\frac{\delta\mathbf{F}_{\text{int}}}{\delta\mathbf{U}}$ is denoted by $\mathbf{K}$ which should be the algorithmic consistent tangent matrix for optimal convergence. Note that the equations involve $\mathbf{M}_{DIC}$ and $\mathbf{b}_{DIC}$ that can be obtained by a standard DIC problem. Once the displacement solution is obtained for a fixed value of the material parameters, we can derive the solution procedure to evaluate the material parameters increment.

For the material parameter increment, the mechanical residual vanishes and hence only the optical part of the cost function plays the role. Thus the solution increment for the constitutive parameters is obtained by minimizing the DIC residual only. We thus have:

$$[\mathbf{M}_{\Lambda}]\{d\mathbf{\Lambda}\}=\{\mathbf{b}_{\Lambda}\} \tag{3.13}$$

In this equation the following definitions hold:

$$\begin{aligned}[\mathbf{M}_{I-MIC}] &= [\frac{\Delta\mathbf{U}}{\Delta\mathbf{\Lambda}}]^T[\mathbf{N}]^T[\nabla\mathbf{F}][\nabla\mathbf{F}][\mathbf{N}][\frac{\Delta\mathbf{U}}{\Delta\mathbf{\Lambda}}] \\ &= [\frac{\Delta\mathbf{U}}{\Delta\mathbf{\Lambda}}]^T[M_{DIC}][\frac{\Delta\mathbf{U}}{\Delta\mathbf{\Lambda}}]\end{aligned} \tag{3.14}$$

and

$$\begin{aligned}[\mathbf{b}_\Lambda] &= [\frac{\Delta\mathbf{U}}{\Delta\mathbf{\Lambda}}]^T[\mathbf{N}]^T[\nabla\mathbf{F}]\{\mathbf{F} - \mathbf{G}(\Lambda)\} \\ &= [\frac{\Delta\mathbf{U}}{\Delta\mathbf{\Lambda}}]^T[\mathbf{b}_{DIC}]\end{aligned} \tag{3.15}$$

the sensitivity matrix $\frac{\Delta\mathbf{U}}{\Delta\mathbf{\Lambda}}$ being computed with $\mathbf{U}$ fields that are obtained by solving equation (3.10). The process is run until convergence is reached on $\mathbf{\Lambda}$ for a given criterion η and a given limit η_c. In practice, the maximum of the ratio between the parameter increment and its current value is used.

$$\eta = \text{Max}\frac{\delta\mathbf{\Lambda}}{\mathbf{\Lambda}} \tag{3.16}$$

The convergence tolerance η_c is set to 10^{-3}.

The iterative procedure is shown in the following flow chart:

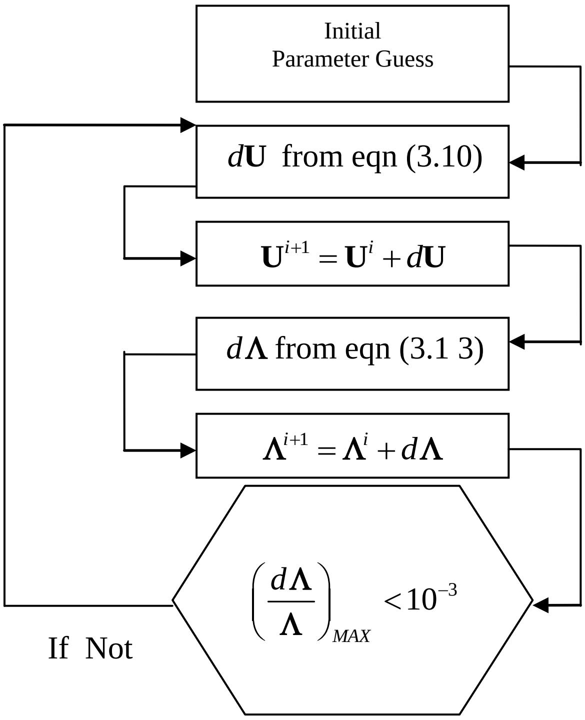

2. Integrated Mechanical Image Correlation using 3D Kinematics

In order to make the strategy applicable to sheets with finite thickness and elasto-plastic material behaviour, we need to extend the previous strategy to three-dimensional kinematics. For this objective, the DIC mesh is extruded along the mean normal direction of its surface so that the mechanical part of the I-MIC functional is computed in 3D.

2.1 Using a Single Camera: A mesh of the specimen in the physical space (i.e., using physical units) is first generated. Using simple affine transformations this mesh is glued on the reference image so that its contour coincides with the contour of the specimen. The DIC analysis is then performed. The direction normal to the sample surface is supposed to be orthogonal to the camera sensor plane. The 2D mesh is simply extruded along this direction. The thickness of the specimen is converted from physical units into pixels. This mesh is to be used for the 3D numerical integration of the mechanical operator $\mathbf{K}$ and $\mathbf{F_{int}}$ whereas only the projection of the first node layer onto the sensor plane is accounted for in the integration of the correlation operator $\mathbf{M}_{DIC}$ and $\mathbf{b}_{DIC}$. A projection operator is defined such that the projected displacement reads

$$\{\mathbf{U}_p\} = [\mathbf{P}]\{\mathbf{U}\} \tag{3.17}$$

where $\mathbf{P}$ is a diagonal matrix. The i^{th} diagonal term P_i is zero if the corresponding DOF is held by a node not located on the first layer. Otherwise its value is set to unity if the corresponding DOF has its components within the sensor plane.

2.2 Using Multiple Cameras: The same strategy can be applied to the stereo camera system. The main difference between mono and stereo camera system is that in later the analysis is performed in the physical space and not within the sensor space. First a 2D mesh is positioned within the physical space so that its projection on the images of the two cameras matches the projection of the specimen. Then the 3D displacement is projected onto the sensors of the two cameras and the correlation residuals are computed. The projection operator is different for each camera; it will be denoted as $\mathbf{P_c}$ of the c^{th} camera.

2.3 Problem Formulation: This formulation deals with a sequence of images captured all along the sample loading. The modified I-MIC3D functional is adapted for the case of multiple images coming from multiple cameras in the following way.

$$\{\mathbf{U},\Lambda\} = ArgMin\left(\begin{array}{l}\left(\dfrac{1}{\alpha}-1\right)\dfrac{1}{k_o}\displaystyle\sum_{t=0}^{T}\{\delta\mathbf{U}\}^T\{\mathbf{F}_{ext}(t)-\mathbf{F}_{\text{int}}(\mathbf{U},\Lambda)\\ +\dfrac{1}{m_o}\displaystyle\sum_{c=1}^{N_{cam}}\sum_{t=0}^{T}\{\mathbf{F}_c(t)-\mathbf{G}_c(t,[\mathbf{P}_c]\{\mathbf{U}\},\mathbf{\Lambda})\}^T\{\mathbf{F}_c(t)-\mathbf{G}_c(t,[\mathbf{P}_c]\{\mathbf{U}\},\mathbf{\Lambda})\}\end{array}\right) \tag{3.18}$$

In this equation, a subscript c has been added to the image vector to indicate the camera number. Discrete summation over time and over the cameras has also been added in order to generalize the functional (3.7) that is dedicated to mono image correlation. The work of the internal and external forces is substituted by the sum over time of the power of these forces, $\delta\mathbf{U}$ being the increment over time of the displacement vector.

2.4 Numerical Features: The mechanical part of the I-MIC3D functional is written considering geometrical non-linearities in an updated-Lagrangian framework. In addition, the numerical integration of the internal forces vector is performed using a reduced integration scheme. When performing numerical simulations using finite elements with reduced integration, one has to control zero-energy hourglass deformation modes. In the present case, the optical part of the functional controls these modes and there is no need to introduce artificial forces.

Calculation of External Force Vector:

The I-MIC3D functional proposed herein involves the finite element external force vector $\mathbf{F}_{ext}$. This vector is a priori unknown, only its resultant being measured experimentally. In practice, we elaborate the following strategy. Given the initial guess of the material parameters and the displacement field obtained by solving a pure DIC problem, a numerical simulation is performed using this displacement field as boundary conditions and the initial constitutive parameters. From this numerical simulation, an external force vector $\mathbf{F}_{ext}^{0}$ can be computed in a post-processing step as the reaction forces to the prescribed displacement field obtained from DIC. This gives us a distribution of nodal forces that allows obtaining a realistic displacement field since the pure DIC displacement was prescribed on the mesh boundary. The resultant of $\mathbf{F}_{ext}^{0}$ is calculated and then scaled so that it equals the experimental resultant force. By multiplying $\mathbf{F}_{ext}^{0}$ by this scaling factor, a realistic nodal force distribution $\mathbf{F}_{ext}$ whose resultant is equal to the experimental force measurement is obtained and used in the I-MIC3D functional.

Application of the Method

In this section we shall apply our new method of I-MIC3D. For these two applications are considered. The first one is by the means of virtual method. Here the images generated are artificial and better suited to analyze the affect of various factors on the overall performance of the Method. The other application is with a tensile test on 304L steel.

In the subsequent pages, we shall describe the performance of the strategy for both DIC as well as stereo image correlation. In stereo, we can obtain out of plane displacement and it would be interesting to see the performance of the Method in this scenario with multiple cameras for more accuracy.

1. Virtual Testing of I-MIC3D

To see the performance of the proposed strategy, a virtual testing procedure is developed. The interest lies in the fact that the virtual images produced are independent of noise and hence we can appreciate the effect of various variables like penalty parameter, initial parameter guess and different identification strategies to the fullest without involving external factors. We shall see the effect of these variables on the identification, convergence rate and correlation error evolution of the I-MIC3D.

Principle

By using an arbitrary displacement value in pixels, sample geometry and the constitutive law, a numerical simulation is performed. The initial mesh is glued onto a virtual image (synthetic or real). Gluing involves operations like translation, rotation and scaling by which we change the physical units of the mesh into pixels. The deformed mesh obtained as a result of the simulation under prescribed displacement is then used to create artificial deformed images for the purpose of virtual testing. Following figure shows the process:

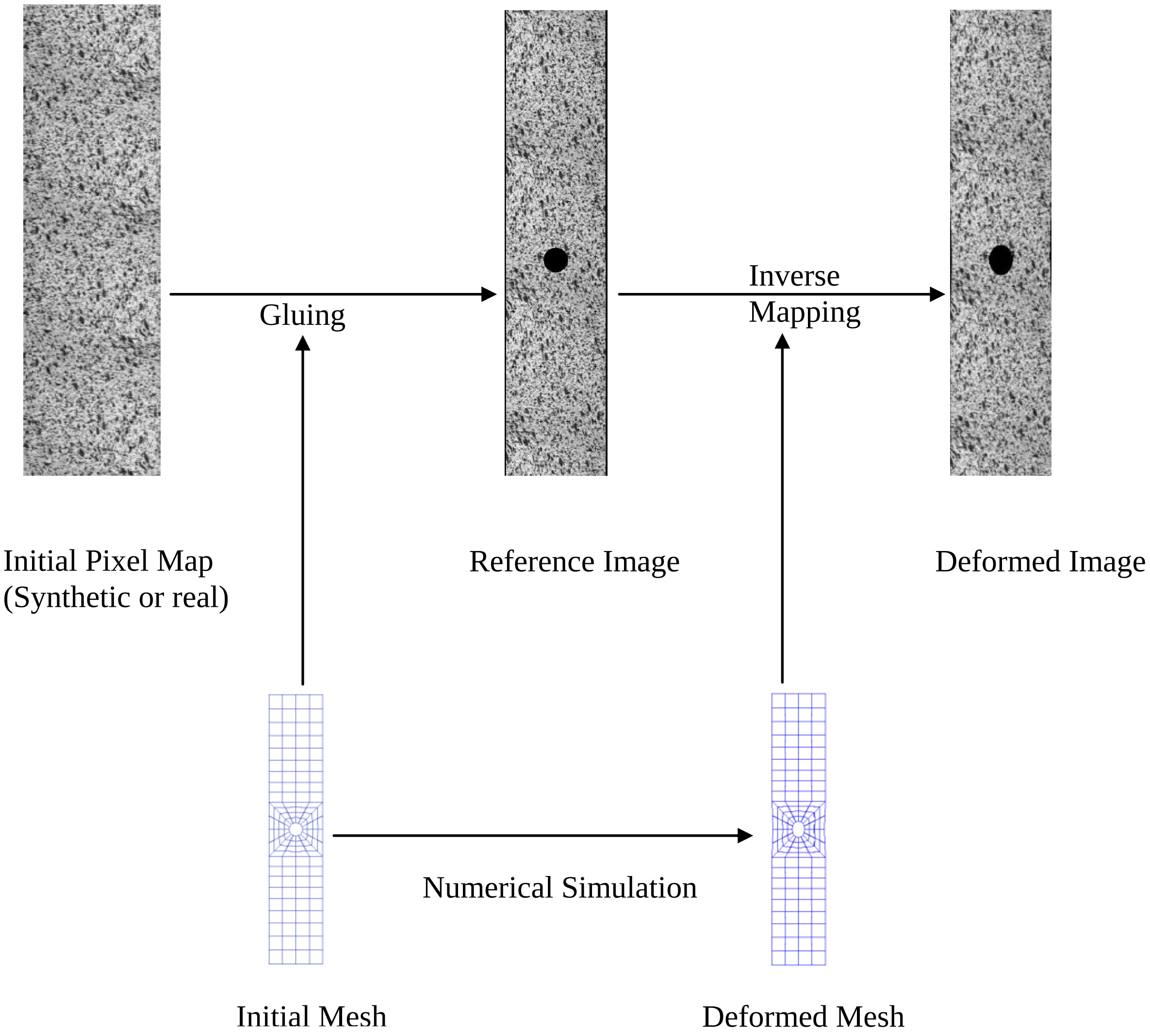

Fig.4.3. Illustration of Virtual Testing Procedure.

Given f the reference image, we generate g so that for a given displacement field $\mathbf{u}$ we have

$$f(\mathbf{x}_p) = g(\mathbf{x}_p + \mathbf{u}(\mathbf{x}_p)) \tag{4.19}$$

In this equation, $\mathbf{x}_p$ are integer pixel positions. In practice, we want the argument of g to be integer values. The mapping $\Phi(\mathbf{x}_p) = \mathbf{x}_p + \mathbf{u}(\mathbf{x}_p) = \mathbf{X}$, where $\mathbf{X}$ are non-integer position, is inverted: $\mathbf{x} = \Phi^{-1}(\mathbf{X}_p)$ so that g is computed at integer pixel position as a sub-pixel interpolation of . Given integer pixel position $\mathbf{X_p}$, non-integer position $\mathbf{x}$ are searched for so that $\mathbf{x} + \mathbf{u}(\mathbf{x}) = \mathbf{X_p}$. A Newton-Raphson procedure is used to obtain $\mathbf{X_p}$ and spline-cubic gray level interpolation is performed to compute $g(\mathbf{X_p}) = f(\mathbf{x})$. Once the images have been generated, the proposed identification strategy is run and we study the influence of penalty parameter and the initial guess of the material parameters.

1.1 Test Design: A virtual sample with a hole similar to the sample used in real experiments is used for virtual testing. The analysis of real experiments is done in the next chapter. The sample width is 20 mm, and its thickness is 8 mm. A hole of 5 mm in diameter is machined in the centre of the sample.

The material considered in the numerical simulation for the virtual testing has elastic-plastic behaviour. For the elastic regime, the parameters are Young's modulus E and Poisson's ratio ν whose values are set to 168 GPa and 0.25 respectively. For the plastic regime, a nonlinear isotropic hardening is considered. The evolution of the yield stress σ_y as a function of the accumulated plastic strain ε_p is parameterized as follows:

$$\begin{aligned}\sigma_y(\varepsilon_p) &= B(\varepsilon_0+\varepsilon_p)^{\delta}+H\varepsilon_p \\ &= B\varepsilon_0{}^{\delta}\left(1+\frac{\varepsilon_p}{\varepsilon_0}\right)^{\delta}+H\varepsilon_p \end{aligned} \tag{4.20}$$

where ε_0 a scaling factor for the accumulated plastic strain.

Considering the following relations

$$\begin{cases}\dfrac{\partial\sigma_y}{\partial\varepsilon_p}(\varepsilon_p=0)=E \\ \sigma_y(\varepsilon_p=0)=S_y\end{cases} \tag{4.21}$$

E being the Young's modulus and S_y the initial yield stress, (4.20) becomes:

$$\sigma_y(\varepsilon_p)=H\varepsilon_p+S_y\left(1+\frac{\varepsilon_p}{\varepsilon_0}\right)^{\delta} \tag{4.22}$$

H is a linear hardening coefficient. The respective values for the parameters are: 1480 MPa for H, 284 MPa for S_y, 7.16 10^{-5} for ε_0 and 0.042 for δ. These values are obtained by using global response of the real experiment. The virtual tests are performed in plane stress as well as using full 3D analysis. The following figure shows the global response of the virtual sample.

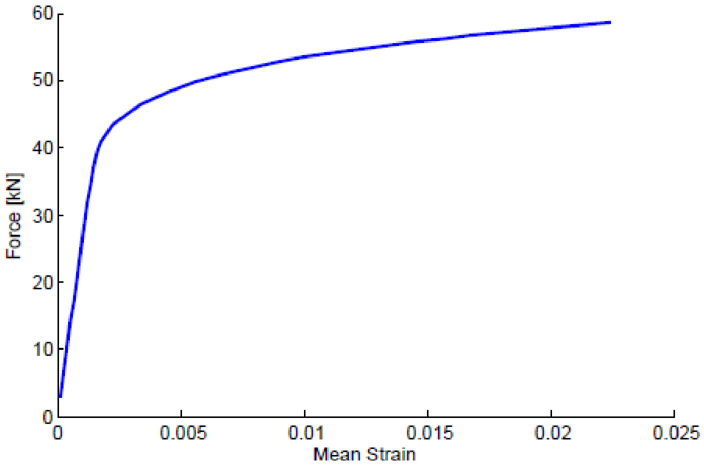

Fig.4.4.Global response of the virtual test (force v.s. mean strain).

In the Figure 4.4, we define mean strain by the following relation:

$$Emean = \frac{2 \times uo \times ti}{\max(yo) - \min(yo)} \tag{4.23}$$

where uo is the imposed displacement and ti is number of the image. The denominator signifies the specimen length.
The numerical simulations for the two cases of plane stress or 3D have been carried out using the mesh shown in the figure 4.5.

For the identification purposes, following three stages will be considered:

Stage 0: contains all the steps before the onset of plasticity (first 5 images)
Stage 1: contains all the steps for a maximum accumulated plastic strain upto 4% (20 images).
Stage 2: contains all the steps for ε_p upto 30% (38 images).

Figure 4.5 also shows the equivalent plastic strain distribution for the two cases of plane stress and 3D.

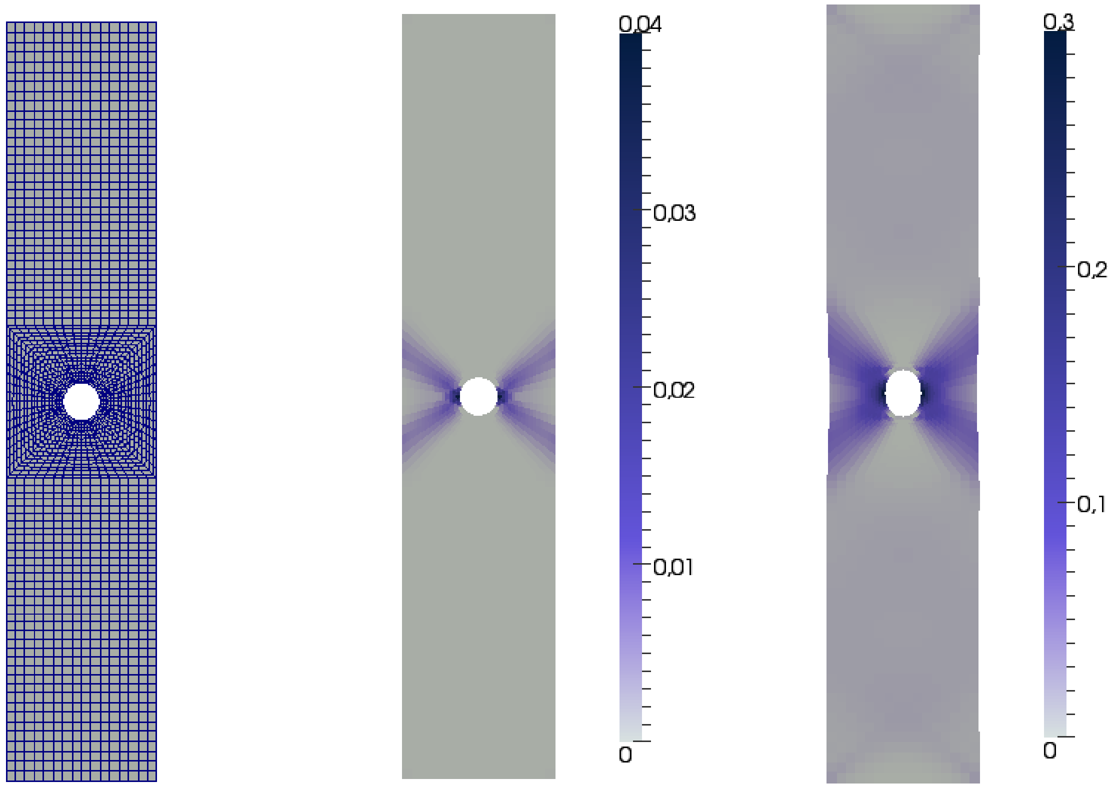

(a) (b) (c)

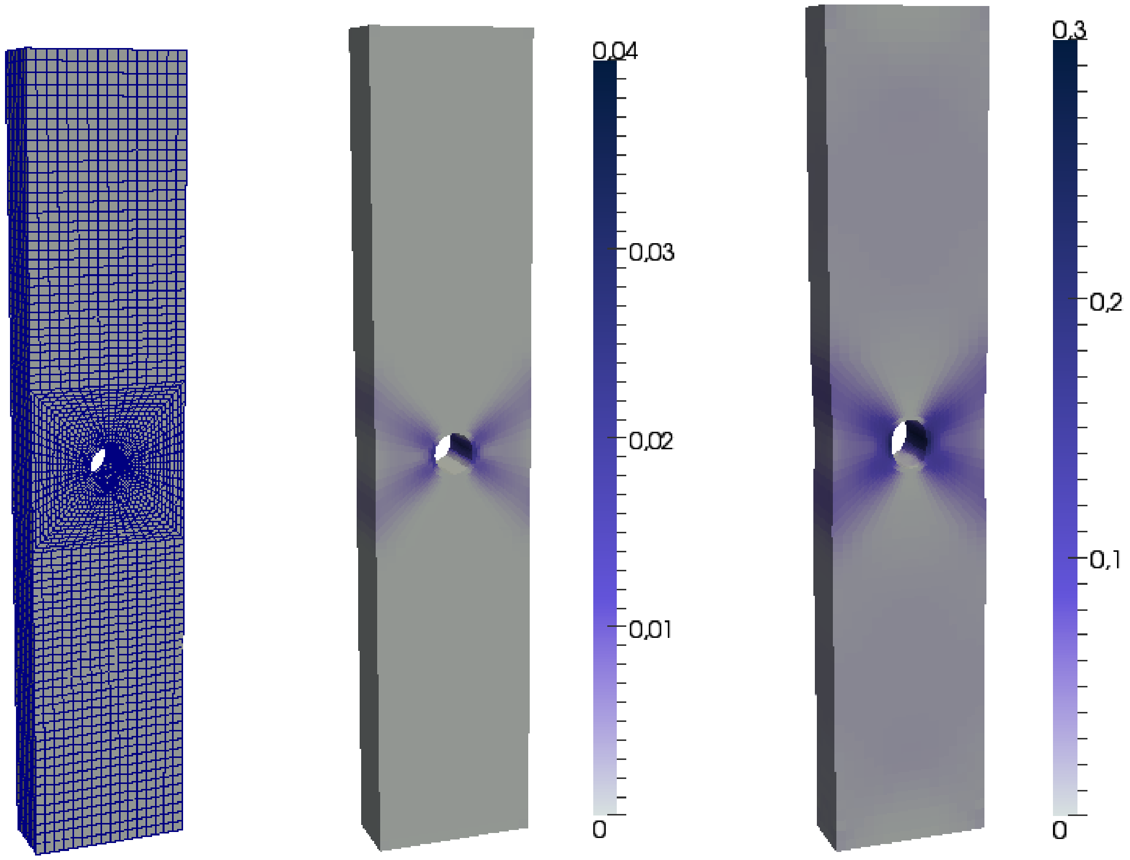

(d) (e) (f)

Fig.4.5.Mesh and equivalent plastic strain distribution for the virtual test. Figures (a) and (d) show the mesh used for the plane stress and 3D analysis respectively. Figures (b) and (e) the equivalent plastic strain distribution for stage 1 and figures (c) and (f) the same field for stage 2.

The corresponding images generated as described above are shown in fig.4.7.

Numerical Simulation Particulars: During the numerical simulation of the reference sample mesh in Abaqus, we have used the option of large displacement theory i.e., Lagrangian behaviour of model description. The number of elements for simulation in plane stress is 992 using the element type CPS4. It is a plane stress linear element prefixed by CPS. For 3D analysis, the mesh has elements 3968 with type C3D8.C3D8 is a 8-node linear brick. Both element types are used with reduced integration. Hourglass control is activated to avoid the spurious non-zero energy modes.

For each step in the analysis the Step Manager also indicates whether Abaqus will account for nonlinear effects from large displacements and deformations. If the displacements in a model due to loading are relatively small during a step, the effects may be small enough to be ignored. However, in cases where the loads on a model result in large displacements, nonlinear geometric effects can become important. Thus the option of Nlgeom is turned on.

The simulation is performed under arbitrary prescribed displacement. The objective is to have the as much plasticity as possible without reaching deformations superior to 50%.

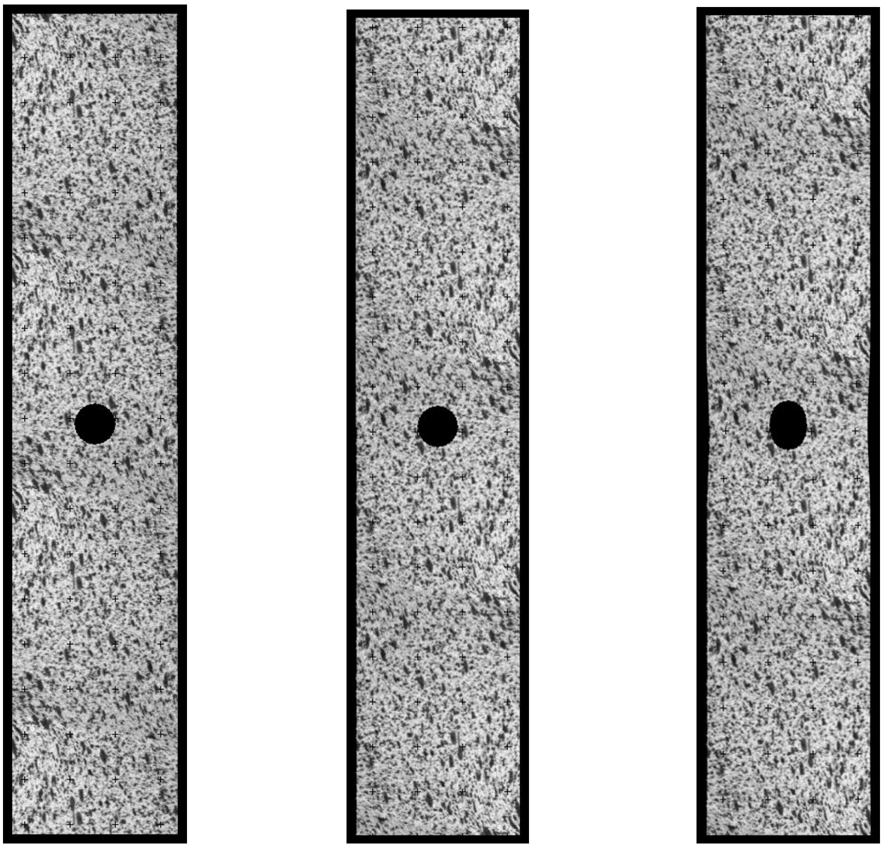

Fig.4.6. Virtual Images generated for the reference state, for stage 1 and stage 2.

1.2 Identification: We chose E, H, δ and S_y as parameters to be identified, and ε_0 is obtained using (4.20) and (4.21)

$$\varepsilon_0 = \frac{\delta S_y}{E - H} \tag{4.23}$$

In the following analysis several types of identification are performed:

I. identification of E using images of stage 0,
II. identification of S_y using images of stage 1,
III. identification of H using images of stage 2,
IV. Simultaneous identification of S_y and H using images of stage 2.

In these analyses, only the parameter to be identified is unknown and all other parameters are set to their respective actual value. Since the same identification strategy would be used in the next chapter involving real experiments, it should be noted that order of different identifications mentioned is important to follow. Once we have the converged values of E and S_y, we can use them as fixed values in the identification of H and then compare the global response of this converged system of values with the experiment.

The meshes used for the I-MIC3D analysis have a lower refinement than those used for the direct analysis and the virtual images generation. In the following we will focus on the identification of E, S_y and H .

1.3 Influence of Penalty parameter: To see the effect of the penalty parameter α we perform the identification of type I and II for different values of α . The initial guess for Young's Modulus E^0 and the initial yield stress S_y^0 are set to 90% of their actual values as reported in section 4.1 from uniaxial experiment. The influence of α on the identified value for E and S_y is shown in the figure below. $\bar{E}$ and $\bar{S}_y$ are the ratio between the current parameter value and its actual value.

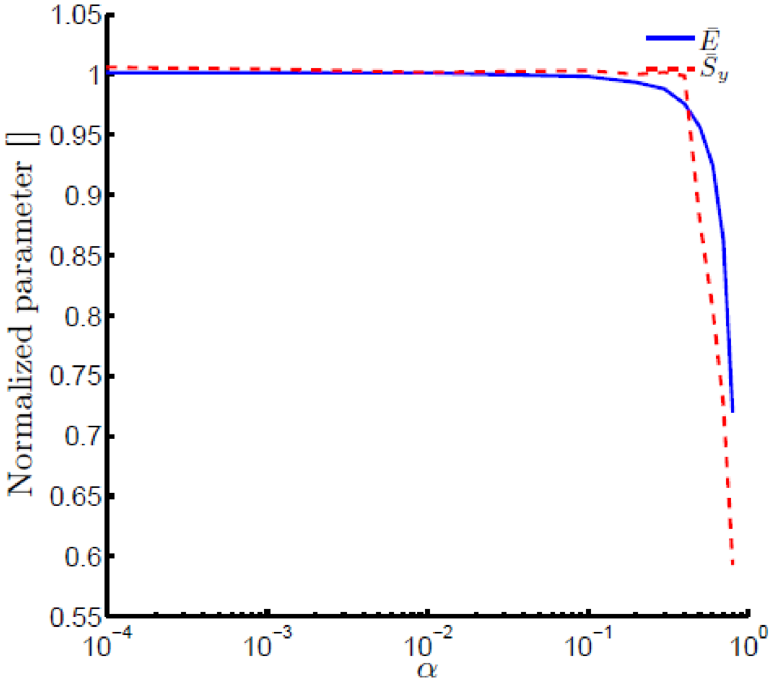

Fig.4.7. Influence of the penalty parameter α for identification of type I and II in plane stress.

Starting for α close to 1 (the emphasis is on the DIC part of the functional), the result progressively improves when α decreases. Thus for better results we may choose α as small as possible. The limit when α vanishes of the I-MIC strategy consists in performing direct numerical simulation under prescribed forces and to minimize the DIC part of the functional with respect to the material parameters. This limit case when $\alpha = 10^{-4}$ will be used for the rest of the analyses.

1.4 Influence of Initial guess: Minimization techniques as mentioned in the previous chapter are sensitive to initial guess for the searched parameters. In the I-MIC3D, the initial guess may not only affect the convergence characteristics of the proposed algorithm but also affects the calculation of the external force vector $\mathbf{F}_{ext}$ .Thus it is essential to evaluate the performance of I-MIC3D with respect to the initial parameter values.

For plane stress and full 3D analysis, figure 4.8 shows the evolution of of the identified parameters when the initial guess varies from 80% to 120% of the actual parameter value.

For Young's modulus the mean deviation (mean of absolute deviation from set of data's mean) is 0.10% for plane stress and 0.0384% for 3D. Concerning its standard deviation we obtain 0.12% and 0.0412% respectively. For the initial yield stress we have 0.0325% for mean deviation and 0.0384% for standard deviation. For the 3D case, we obtain 0.0325% and 0.0370% respectively. Concerning the linear hardening modulus in plane stress, the MD is 0.0440% and SD is 0.0559% while in 3D, the MD is 0.0232% and SD is 0.0306%. These values are all less than 1% and demonstrate that the proposed method has a really low sensitivity to the initial parameter value.

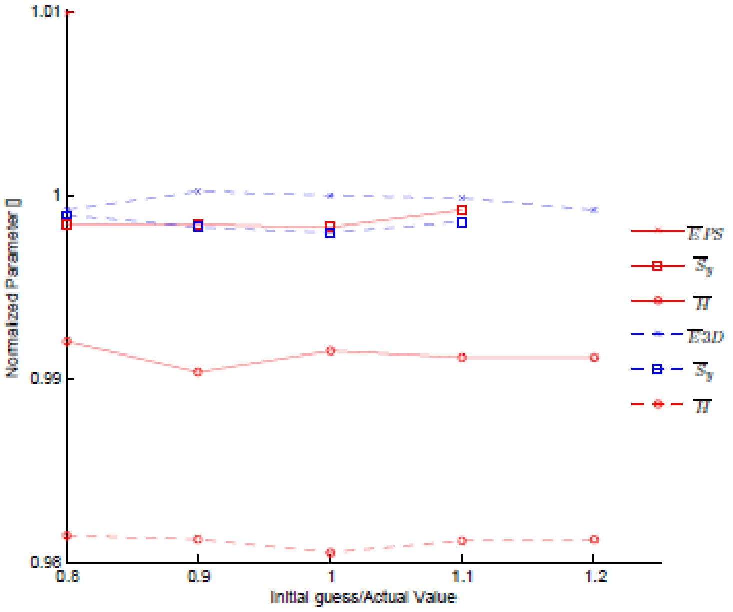

Fig.4.8. Influence of the initial guess for identification of type I, II and III in plane stress or full 3D kinematics.

In figure 4.8, the results obtained from analysis types II, III and IV are compared. It is shown that the results are similar for separate as well as simultaneous identification of the parameters. The major difference is the slower rate of convergence for simultaneous identification of type IV. As illustrated in figure 4.9. for a sequential identification, 7 and 4 iterations are required for S_y and H respectively whereas convergence is achieved for a simultaneous identification after 15 iterations. Moreover, for type IV analysis, the analysis is performed over all 38 images whereas for type II analysis only 20 images are required. The cost of sequential identification is thus even less expensive. Figure 4.9(b) shows the relative error with respect to the number of iterations.

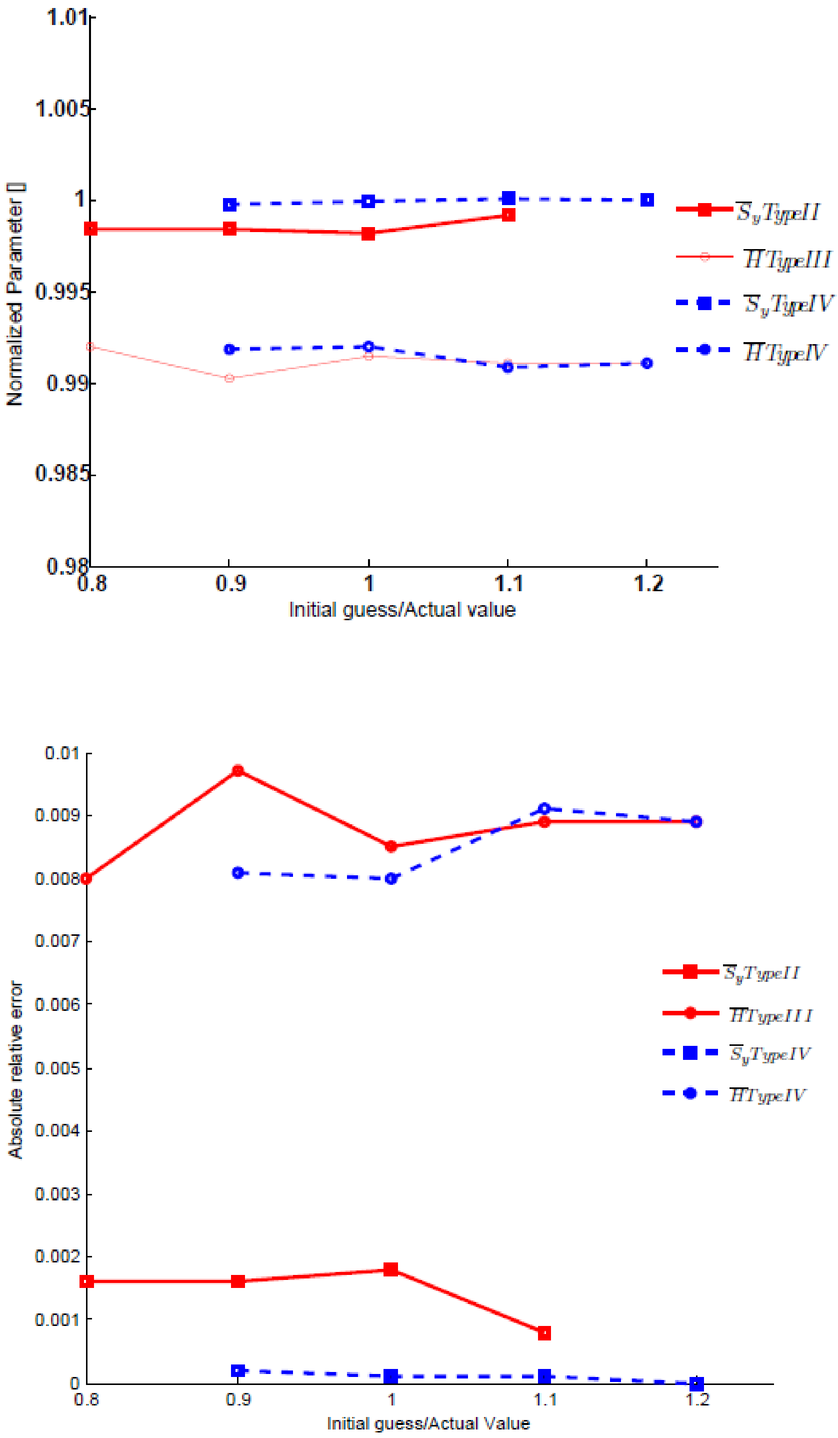

Fig.4.9. Influence of the initial guess for identification of type I, III and IV in plane stress. Also shown in (b) is the relative error evolution.

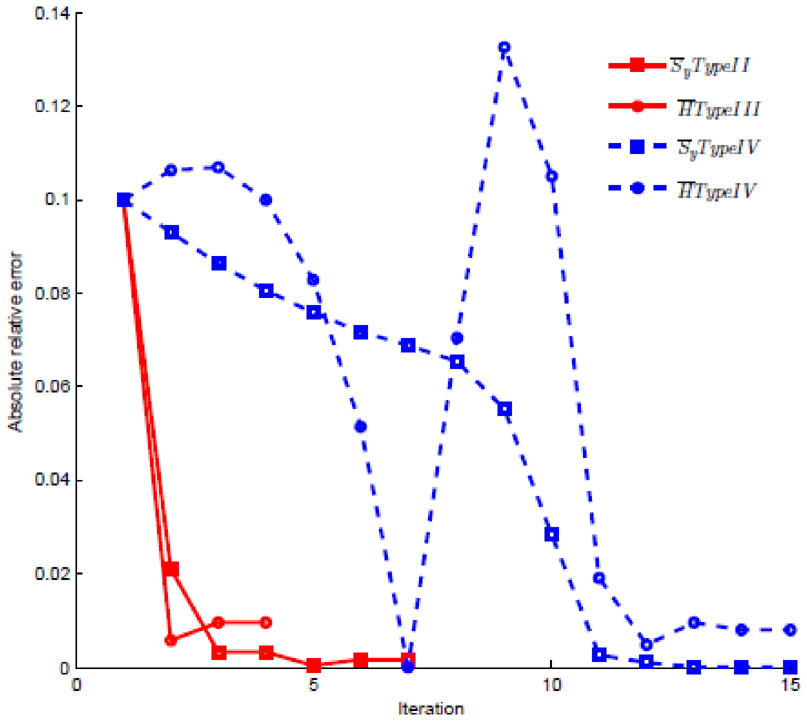

Fig.4.10. Evolution of the identified parameters of type II, III and IV identification based on plane stress assumption during the iterations. The initial guess for both parameters is 90% of the actual value.

The fast convergence rate of the I-MIC3D is also shown in the figures below. For different values of the initial parameter guess, the evolution of the estimated parameter is plotted. Focussing on the identification of S_y and H, we can see the convergence is very fast and only 3 or 4 iterations are required in almost all cases for an acceptable estimation of the parameter.

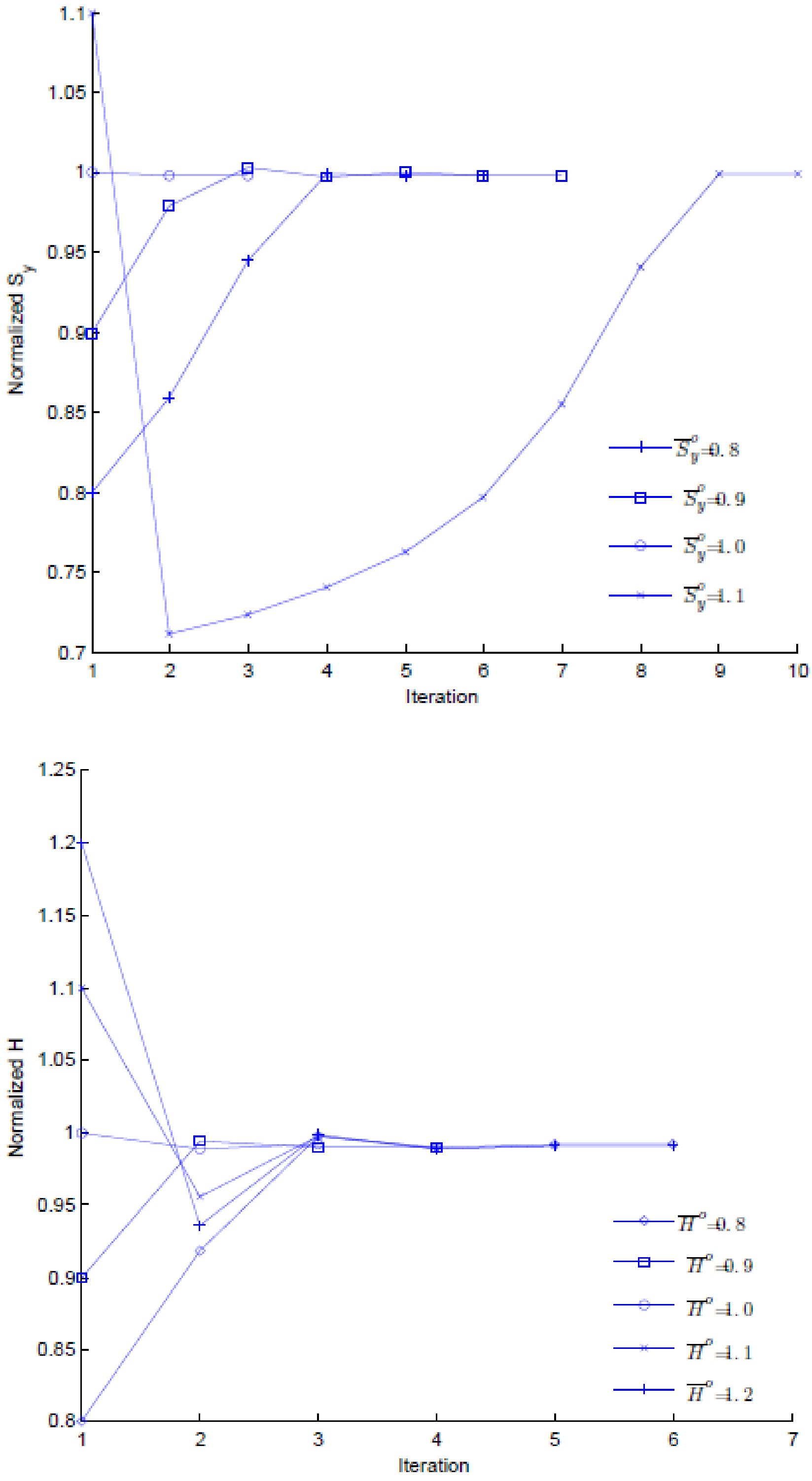

Fig.4.11. Evolution of the identified parameters of type II, III identification based on plane stress assumption during the iterations for various values of the initial guess.

1.5 Correlation Error for DIC and I-MIC3D: The performance of the I-MIC3D which is based on the DIC concept can also be appreciated by examining the evolution of the mean correlation error. The mean correlation error is defined as:

$$merror = \frac{roi - disc}{dynamic} \tag{4.25}$$

where *merror* is mean correlation error, *roi* is the region of interest of the reference image *disc* is the corrected deformed image, corrected by the previously determined displacement and *dynamic* is the difference between maximum and minimum intensities of the reference image. Thus mean correlation error describes the distance between $f(\mathbf{x})$ and $g(\mathbf{x}+u(\mathbf{x}))$ divided by the dynamic of f. It is observed that as the element size decreases, merror also decreases as the correlation system is less constraint [55].

For a type II plane stress assumption, figure 4.11 shows the overall mean correlation error as a function of the iteration for different value of the initial parameter guess. The graph shows increased initial error when the initial guess spreads from the actual value. However, during the iterations it decreases rapidly to the minimum value of 1.8% of the image dynamic. Figure 4.12 shows the evolution of the mean correlation error with respect to the mean strain for the converged value of the parameter. The mean error is plotted as a function of the mean strain for the converged parameter value. This evolution is compared to the result from a pure DIC analysis. The difference in the values after a strain of 0.5% comes from the boundary conditions and the external force vector.

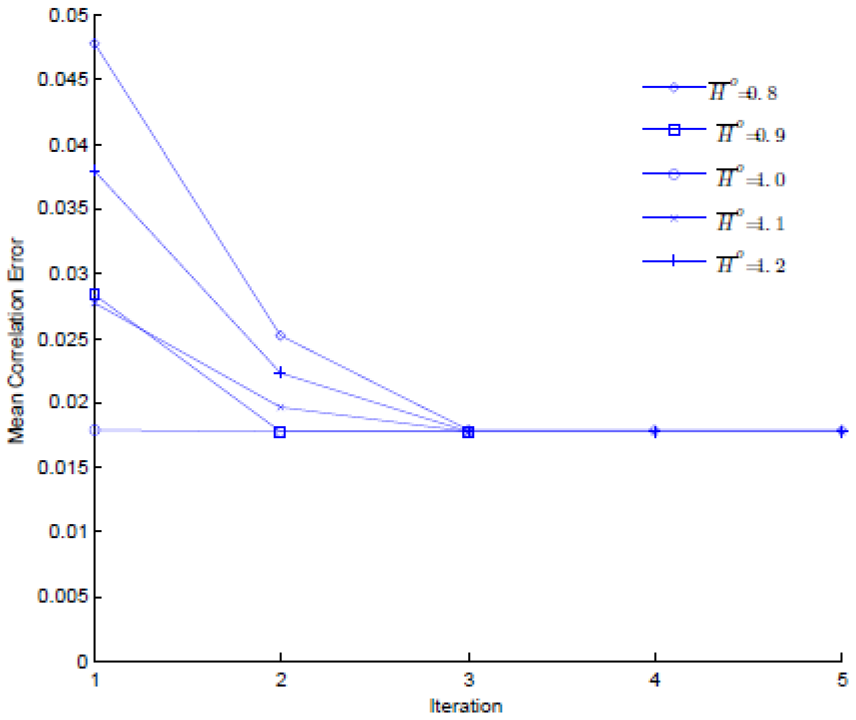

Fig.4.12. Evolution of overall mean correlation error (normalized by the dynamic of the image) for a type III analysis based on plane stress assumption during the iterations.

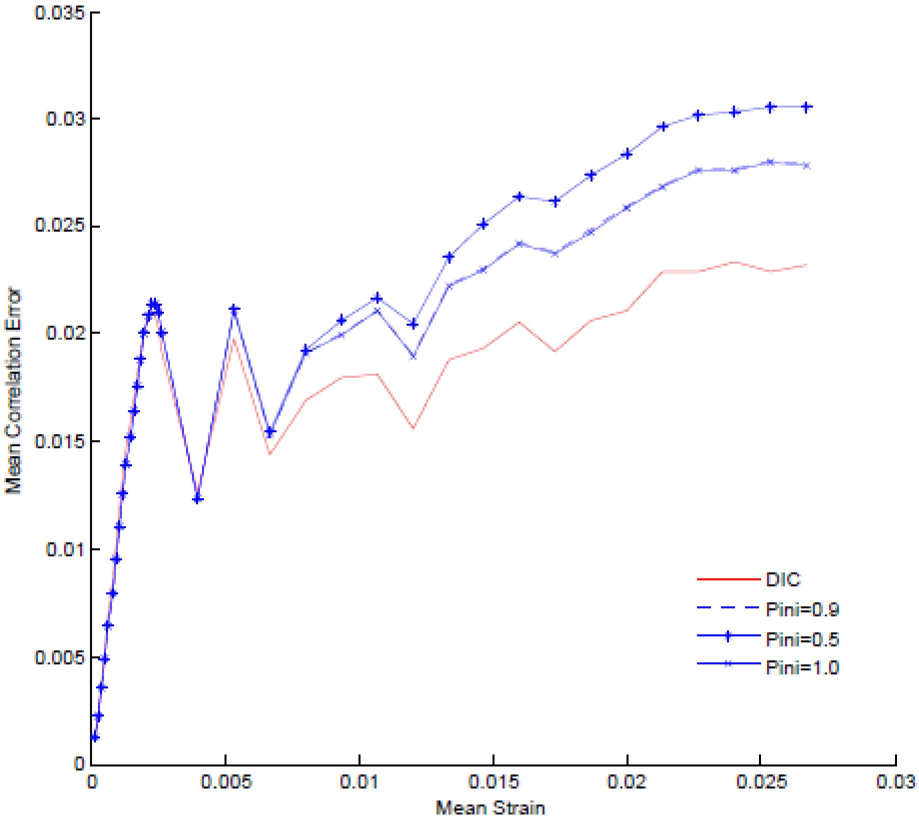

Fig.4.13. Mean correlation error as a function of the mean strain. The initial parameter guess ratio with respect to the actual parameter value is varied to 0.5, 0.9 and 1 for the I-MIC3D analysis.

2 Application to a Tensile Test

After the virtual testing procedure, we move on towards the application of the method to a tensile test of 304L steel specimen. This will give us the necessary validation results for the proposed strategy.

2.1 Experimental Devices and Instrumentation

The tests are performed on the Zwick electric tension-compression machine with maximum capacity of 100kN. An external extensometer is used for the experiment. The loading and unloading cycles are controlled automatically via the electronic control of the machine. For the present experiment we have used a single monotonic loading and unloading is used. Two captors are used for the measurement of force and displacement. One computer bridges the gap between the user and the electronic control of the machine. It is equipped with the software testXpert*II* to program the test as required.

To capture the images existing computer software VicSnap, is used. Since for correlation to work it is important that the specimen image should have a unique fingerprint of light intensity values, an artificial random texture of black and white enamel spray paint is deposited on the two faces of the test specimen. The size of the speckle is random and has been shown previously to strongly affect the sensitivity and accuracy of the correlation technique. As a general rule, the texture should be small and should vary from 1-2 to about 3 pixels [43].

In the experiment we have used a telecentric lens. Most lenses exhibit varying magnification for objects at different distances from the lens. The key problems faced by common objective lenses are:

- Magnification changes, due to object displacement
- Image distortion
- Poor image resolution
- Perspective errors
- Object edge position uncertainty, due to lighting geometry.

Telecentric lenses reduce or even cancel most of these problems, the most important being the magnification changes. It enables us to capture images without any influence of out of plane displacement.
Mechanical parts cannot be precisely positioned because of vibrations or a measurement must be performed at different depths, or even worse, the object thickness (and therefore the object surface position) may vary. So, it is diffficult to obtain a perfect correlation between imaged and real dimensions in case of orthonormal view of the object (i.e, with no object sides imaging). This can be avoided by the use of telecentric lenses provided the object stays within a certain “depth of field” or “telecentric range”. This is due to particular path of rays within the system: Only those rays whose principal ray is parallel to the opto-mechanical main axis are collected by the objective.

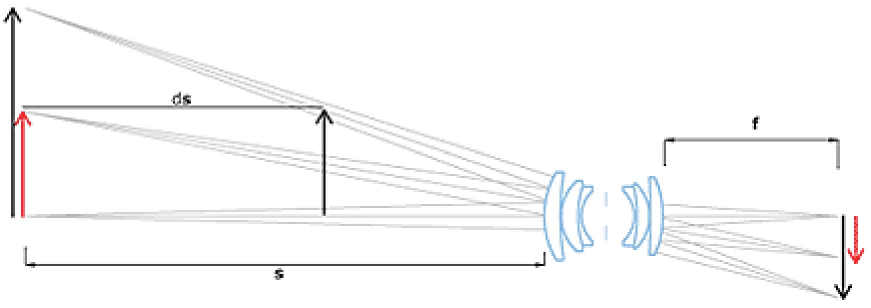

Fig.4.14. Different magnification for objects at different conjugates with respect to the ordinary lens.

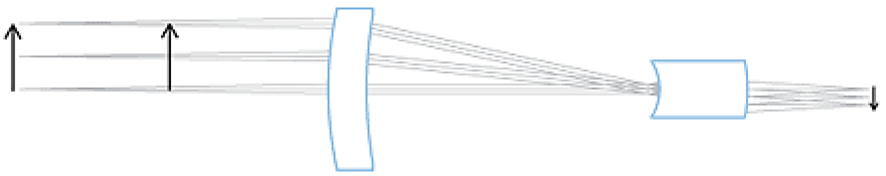

Fig.4.15. Constant Magnification by the telecentric.

Just to get the feeling of how the two different objective types behave, let us think of a standard lens with a focal length f = 12 mm, interfaced to a 1/3” detector, looking at an object of height H = 20 mm, placed at a distance s = 200 mm. Assuming an object displacement of ds = 1mm, the change in its dimensions will be around:
dH = (ds/s) · H = (1/200) ·20 mm = 0,1 mm
In a telecentric lens the magnification change is determined by the “telecentric slope”: good telecentric lenses show an effective telecentric slope theta of about 0,1° (0,0017 rad); this means that the object dimensions would only change of about
dH = ds · theta= 1 · 0,0017 mm = 0,0017 mm
for each displacement ds of 1 mm. Thus, with telecentric lenses the magnification error is reduced to 1/10 to 1/100 compared to standard lenses.

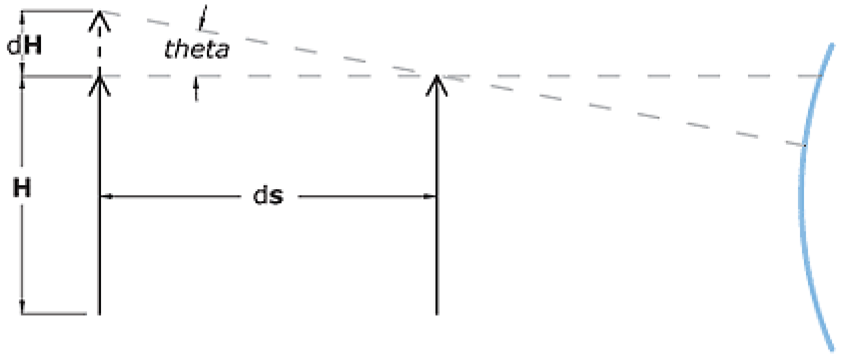

Fig. 4.16. The telecentric slope determines the magnification change

The concept of “telecentric range” or “telecentric depth” is often interpreted as the field depth range where magnification remains constant. This is a somewhat misleading interpretation as it implies that the remaining space is “non-telecentric” while this parameter should always be associated with the maximum measurement error caused by the lens within that same range. A much more significant parameter is “telecentric slope” (above referred to as “theta”) or “telecentricity”. Such angle defines the measurement error due to object displacement, no matter where the object is placed: since the principal optical rays “go straight” the error amount is obviously space-independent.

In order to collect telecentric rays, the front optical components of a telecentric lens must be at least as large as the object largest dimension; for this reason telecentric lenses are larger, heavier and therefore more expensive than common optics.

2.1.1. Particulars of the lenses used in the expriement: For the experiment, three objectives are used. One is the telecentic lens used with 4 million pixel camera for Mono-DIC. The other two objectives are for 16 million pixel left and right cameras used for Stereo-DIC.

Terminology: Before describing the specifications of the lenses, following terms are defined. These are important for the understanding and proper usage of the optical devices.

1. Lens elements & Image quality

All but the simplest cameras contain lenses which are actually comprised of several "lens elements." Each of these elements directs the path of light rays to recreate the image as accurately as possible on the digital sensor. The goal is to minimize aberrations, while still utilizing the fewest and least expensive elements

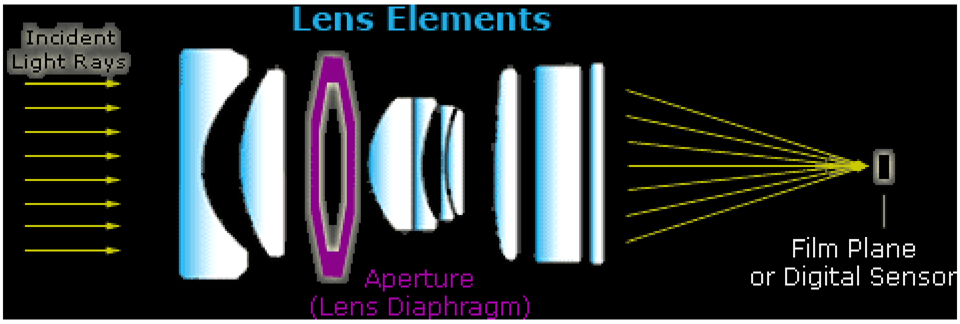

Fig.4.17. Lens Composition.

Optical aberrations occur when points in the image do not translate back onto single points after passing through the lens — causing image blurring, reduced contrast or misalignment of colors (chromatic aberration). Lenses may also suffer from uneven, radially decreasing image brightness (vignetting) or distortion.

2. Lens focal length

The focal length of a lens determines its angle of view, and thus also how much the subject will be magnified for a given photographic position. Wide angle lenses have short focal lengths, while telephoto lenses have longer corresponding focal lengths.

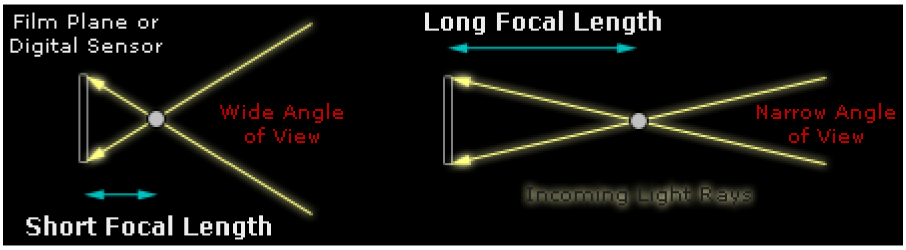

Fig.4.18. Focal Length

3.Influence of lens aperture or f-number.

The aperture range of a lens refers to the amount that the lens can open up or close down to let in more or less light, respectively. Apertures are listed in terms of f-numbers, which quantitatively describe relative light-gathering area (depicted below).

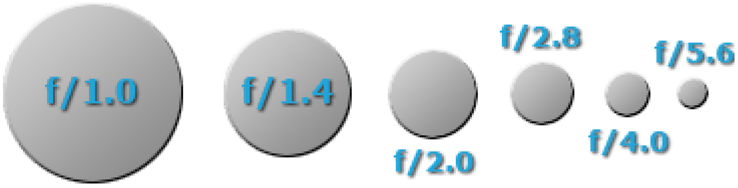

Fig.4.18. f-number

Aperture opening (iris) is rarely a perfect circle, due to the presence of 5-8 blade-like lens diaphragms.

4. Depth of Field

Depth of field refers to the range of distance that appears acceptably sharp. It varies depending on camera type, aperture and focusing distance. Since there is no critical point of transition, a more rigorous term called the 'circle of confusion' is used to define how much a point needs to be blurred in order to be perceived as unsharp. When the circle of confusion becomes perceptible to our eyes, this region is said to be outside the depth of field and thus no longer "acceptably sharp." The circle of confusion above has been exaggerated for clarity; in reality this would be only a tiny fraction of the camera sensor's area.

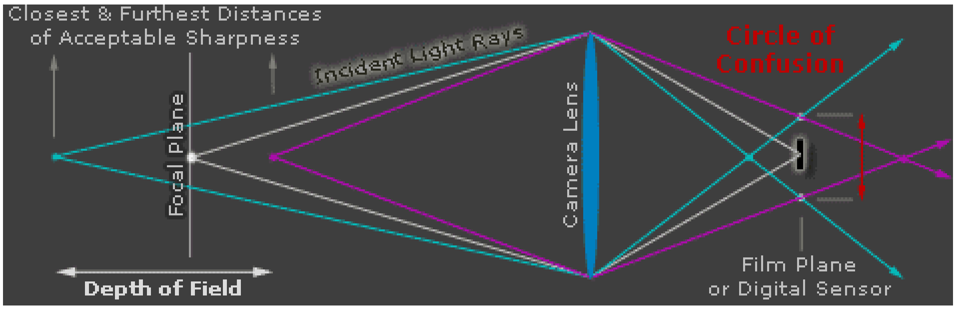

Fig.4.19. Depth of field.

Telecentric Lens: Following lines gives the characteristics & geometry of the telecentric used to get the images for the mono-DIC.

- Object side telecentric light path
- Spectral range 380...900nm
- Maximum object field diameter 57 mm
- max. diameter of lenses 71mm
- Low distortion
- Extremely low telecentric error
- Manual operated iris aperture with fixing
- Robust industrial design: dust-proof, shock-proof
- C-mount (thread connection)

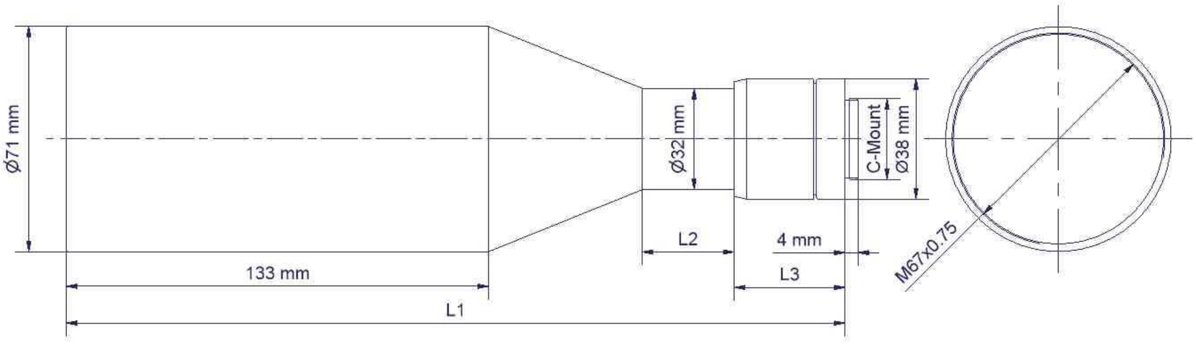

Fig.4.20. Telecentric Lens.

The optical axis must be aligned perpendicularly to object level or plane of measurement to realize exact measurement. The environmental temperature in which the telecentric can operate is -10°C to 50°C.

In the above figure the value of L1 is 292 mm; L2 is 32 mm and L3 is 82 mm. The weight of the telecentric is 1150 g.

Lens for the stereo-DIC: The lens used is AF Micro-Nikkor with a focal length of 200mm. Two of such lenses are used for the left and right images of the stereo system. The following is the list of the specifications of the lens.

- Close-up to approx. 0.5m.
- ED (extra low dispersion) glass elements for higher optical performance
- IF (Internal Focusing) technology
- 260mm working distance
- Nine-blade rounded diaphragm blades achieves a natural blur for out-of-focus elements

Focal length	200mm
Maximum aperture	f/4
Minimum aperture	f/32
Lens construction	13 elements in 8 groups
Picture angle	12°20'
Closest focusing distance	0.5m
No. of diaphragm blades	9
Diameter x length	Appproximately 76 x 193mm
Weight	Approximately 1,190 g

Fig.4.21. Lens and its construction- used for stereo-DIC.

2.1 Test Setup: A uniaxial test is performed on the specimen of 304L steel. The specimen geometry is the same as used in the virtual tests. Material parameters are identified using the load displacement curve. These identified values serve as the actual values and used for comparison with the converged values obtained via I-MIC3D. These actual values are also used for the initial parameter guess that can vary from 80% to 120% of these values. The material model is the same as described in equation (3.20) and the values of the material parameter identified with the uniaxial experiment are the ones that were used in the previous section.

The following figure shows the specimen geometry used in the tensile test and the overall experimental setup with instruments for image acquisition:

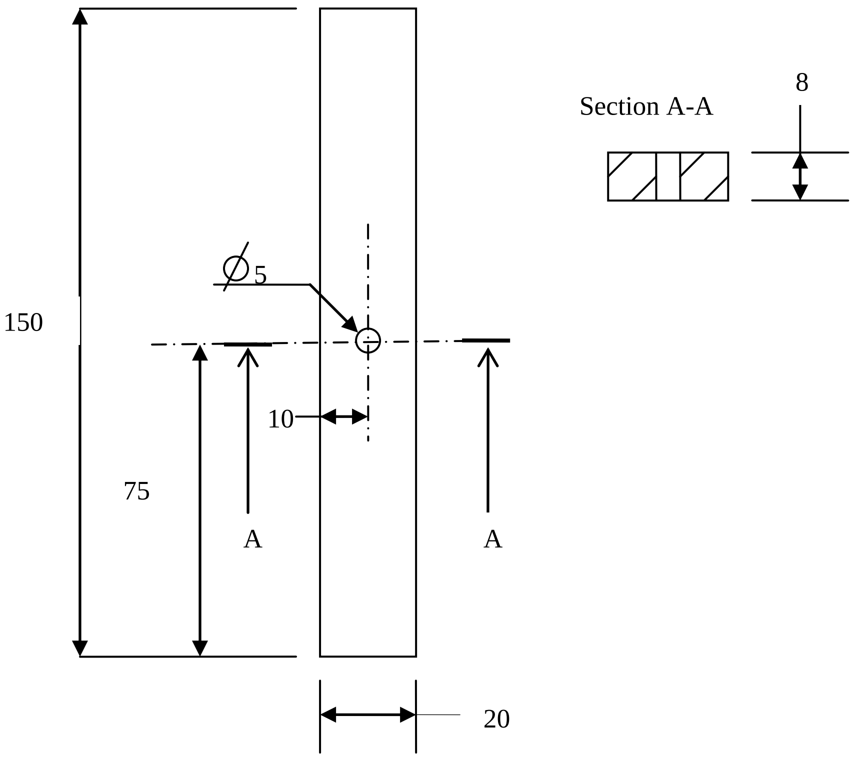

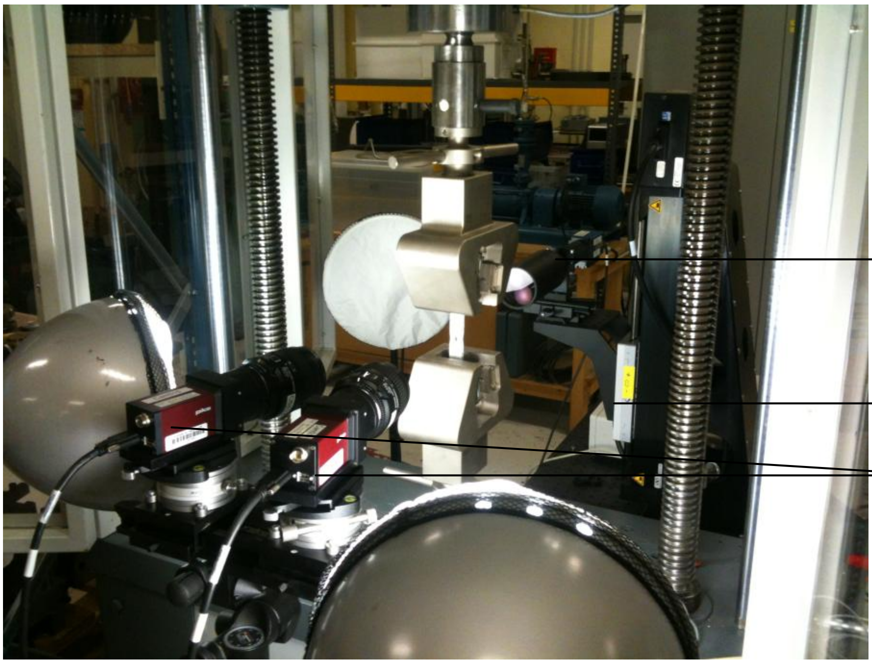

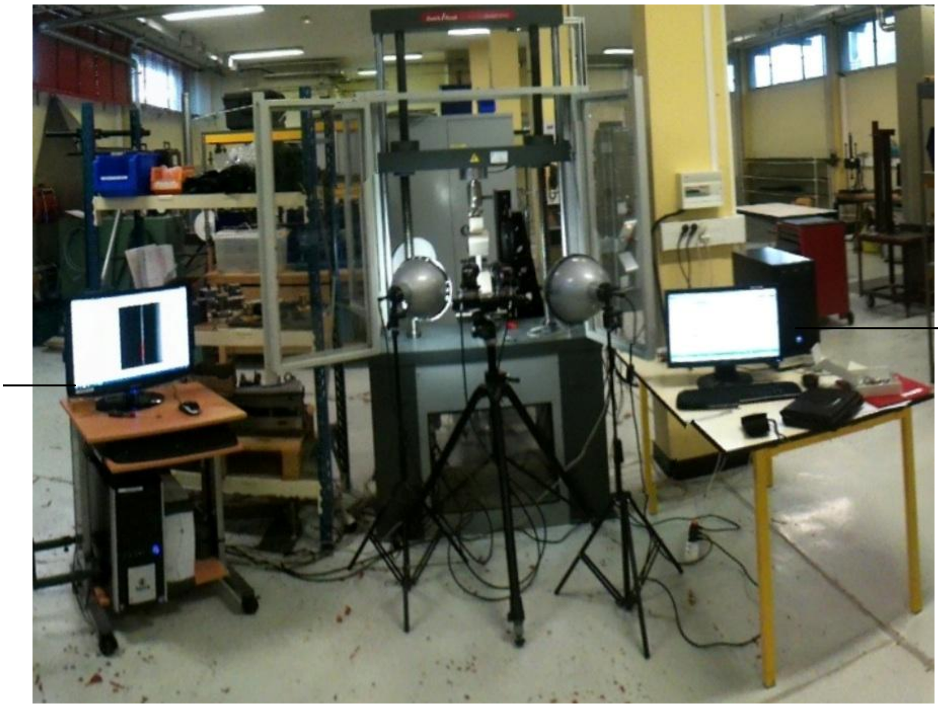

Fig.4.22. Specimen geometry and Experimental Setup with devices employed.

The global response of the sample is shown in the Fig. 4.14 with all the stages employed as in the previous section of virtual testing procedure. Stage 0 contains all the steps before the onset of plasticity (5 images), Young's Modulus E will be identified using these images. Stage 1 contains the steps for low plastic strain (12 images), the initial yield stress S_y will be identified with this data. For the identification of H and δ, stage 2 contains the steps for ε_p up to 30% (70 images).

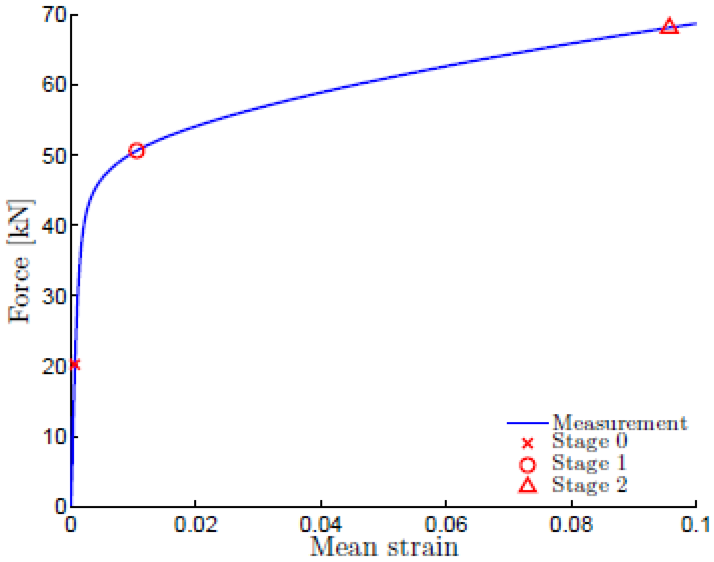

Fig.4.23. Global response (force versus mean strain curve) of the real experiment. The different stages of the identification process are also defined on the graph.

2.3 Mono-DIC analysis: Real images acquired via VicSnap are analyzed by custom made DIC software. As shown in the Fig. 4.13, on one side of the sample a 2048×2048 pixels digital camera mounted with a telecentric lens is used. Since we use telecentric lens to avoid out of plane displacement, Mono-DIC can only measure inplane displacement. However the mechanical model for the I-MIC3D analysis is 3D in order to account for out of plane effect obtained because of the finite thickness of the sample and plastic incompressibility.

The three cameras of the experimental setup are all synchronized with the help of a trigger pulse. The following figure shows the reference image of the camera for Mono-DIC.

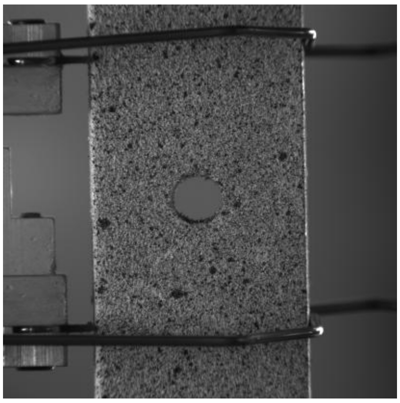

Fig.4.24. Reference Image for the experiment. The image is obtained using one camera with a telecentric lens.

The images obtained are then analyzed. A VTK mesh of the specimen is generated in GMSH and is “glued” to the image. The mesh has 324 quadrangles. Since the problem is non-linear, a Newton algorithm is used as explained in section 4.2. Iterations are performed to find the global minimum as explained in the section 4 of the bibliography. Results are then viewed in ParaView.

Following figures show the two components of the displacement and the mesh used.

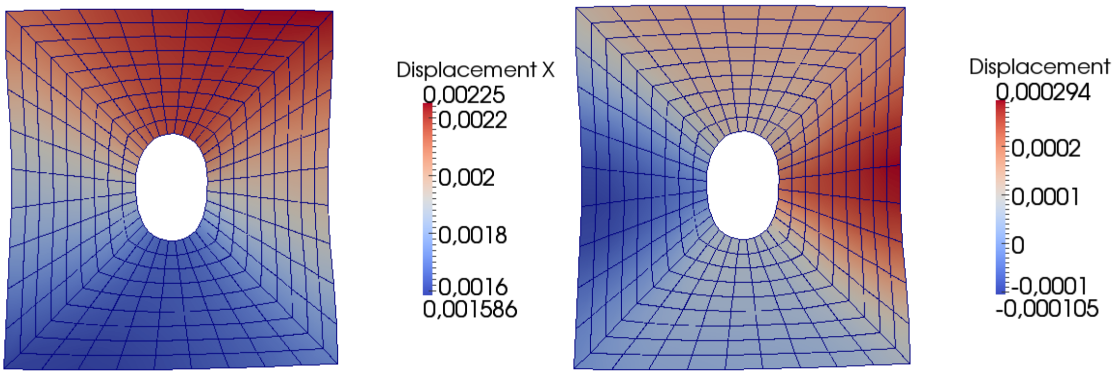

Fig.4.25. Displacement field (meters) obtained using Mono-DIC. VTK mesh used for the analysis is also shown for the last analyzed image.

As noted before we have no information about the third component of the displacement from this analysis. To get information related to the out of plane displacement we move on to stereo digital image correlation.

2.4 Stereo-DIC analysis: On the other side of the sample, two cameras with a 4872×3248 pixel CCD mounted with a 300mm lens are used. They will be used for the binocular stereovision. The following figure shows the stereovision. $P(X,Y,Z)$ is the 3D point to be measured, $p_1(u_1,v_1)$ and $p_2(u_2,v_2)$ are its stereo-projections in the images, C_1 and C_2 are the optical centres of the two cameras. From a pair of images, it is possible to compute the 3D coordinates of a physical 3D point by *Triangulation*, assuming that:

1. The geometry of the stereo-rig is known (i.e. the relative position and orientation of the two cameras) is known. This problem is solved by the off-line camera calibration procedure.
2. The two image points p_1 and p_2 are matched, i.e. identified as corresponding to the same physical point P. This is called the stereo-matching problem.

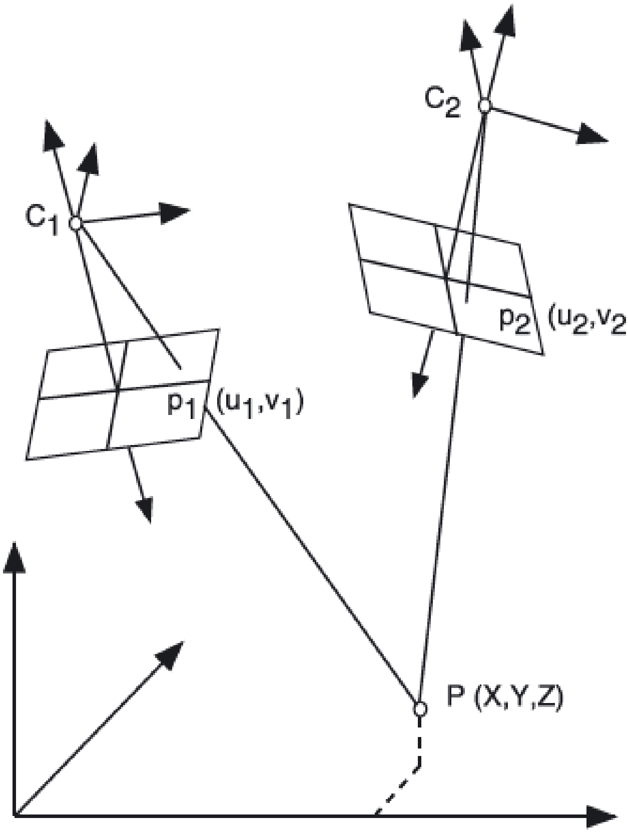

Fig.4.26. Binocular Stereovision.

Calibration of the stereovision sensor: The calibration procedure purpose is the determination of the imaging parameters of each of the cameras (intrinsic parameters) as well as the external positions and orientations of the cameras with respect to a global coordinate system. The system calibration is needed for transforming image positions on the CCDs of the two cameras of a specimen surface point to the corresponding 3D coordinates, via triangulation, of that point. Calibration errors are potentially a major source of systematic evaluation errors limiting the resolution of the results.

The technique used requires the cameras to observe a (planar) pattern shown at a few different orientations (typically between 10 and 20). Using a photogrammetric bundle adjustment approach, the intrinsic parameters of each camera, the 3D points of the pattern and the relative position and orientation between the two cameras are estimated all together. The following figure shows the pattern used during the system calibration:

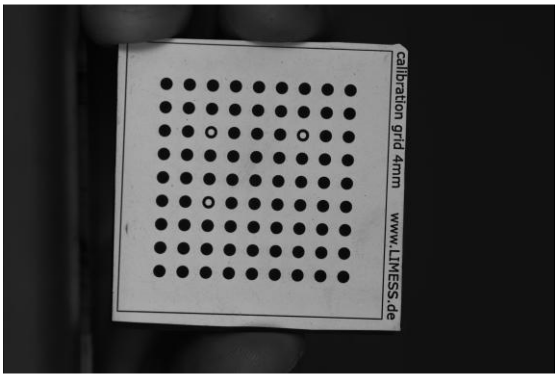

Fig.4.27. Regular pattern used for calibration of the stereo camera system.

Given a point p_1 in image 1, its corresponding point p_2 in image 2, termed 'stereo-correspondent' appears to be always lying along a line of image 2 defined entirely by the coordinates of p_1, the relative position/orientation of the two cameras and their intrinsic parameters: this is the so-called epipolar line associated with p_1 (shown in Figure 4.21). This geometric constraint inherent to any stereo-imaging system, termed 'epipolar constraint' is very interesting because it simplifies the search for the stereo-correspondent of a given point from a 2D search across the entire image to a 1D search along its epipolar line.

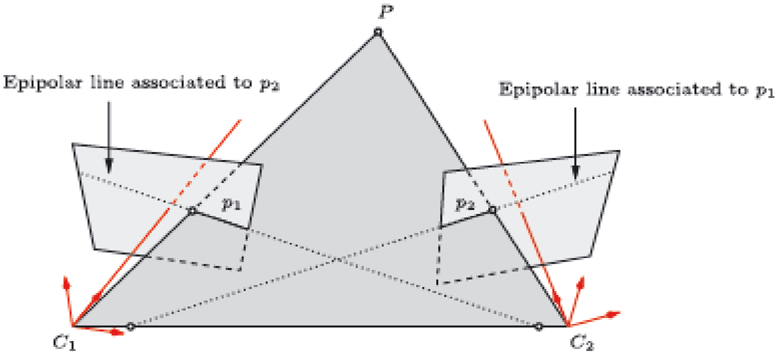

Fig.4.28. The camera optical centres C_1 *and* C_2*, the 3D point* P *and its images* p_1 *and* p_2 *lie in a common plane. This plane intersects each image plane in an epipolar line.*

Once the system has been calibrated, the problem of stereo-matching can be done using the same method as detailed in section 4 of the bibliography. The correlation algorithm tracks the observed gray value patterns for each camera and transforms corresponding pixel positions in both cameras into 3D coordinates for each step, resulting in a track of each surface pixel in 3D space. As the surface deformation is measured point-wise, displacements of individual surface points and subsequently surface strains can be evaluated.

The following figure shows the reference images of the two (left and right) cameras used in the stereo vision system:

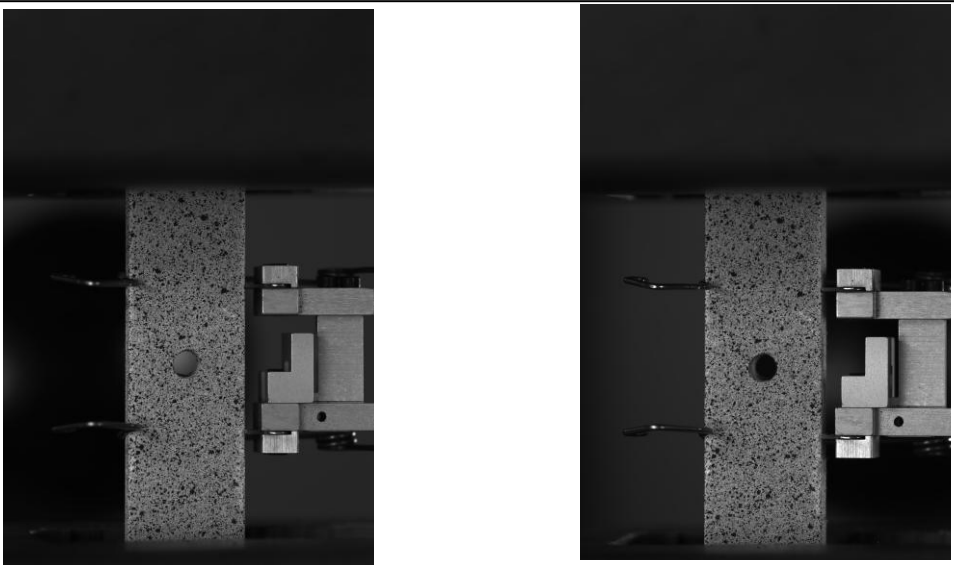

Fig.4.29.Reference images of the left and right camera of the stereo-vision system.

The displacement field obtained for the last image obtained is shown in the figure below. Stereo-DIC also provides the out of plane displacement. The magnitude of the out of plane displacement is small which shows that the grips are properly aligned. Thus, Stereo-DIC also gives information related to the boundary conditions. The difference that we see between the mono and stereo DIC is due to errors in the calibration of the stereo image system. One may also note the difference in the magnification of the mono and stereo images. However the region of interest chosen for image correlation is almost the same size (in pixels).

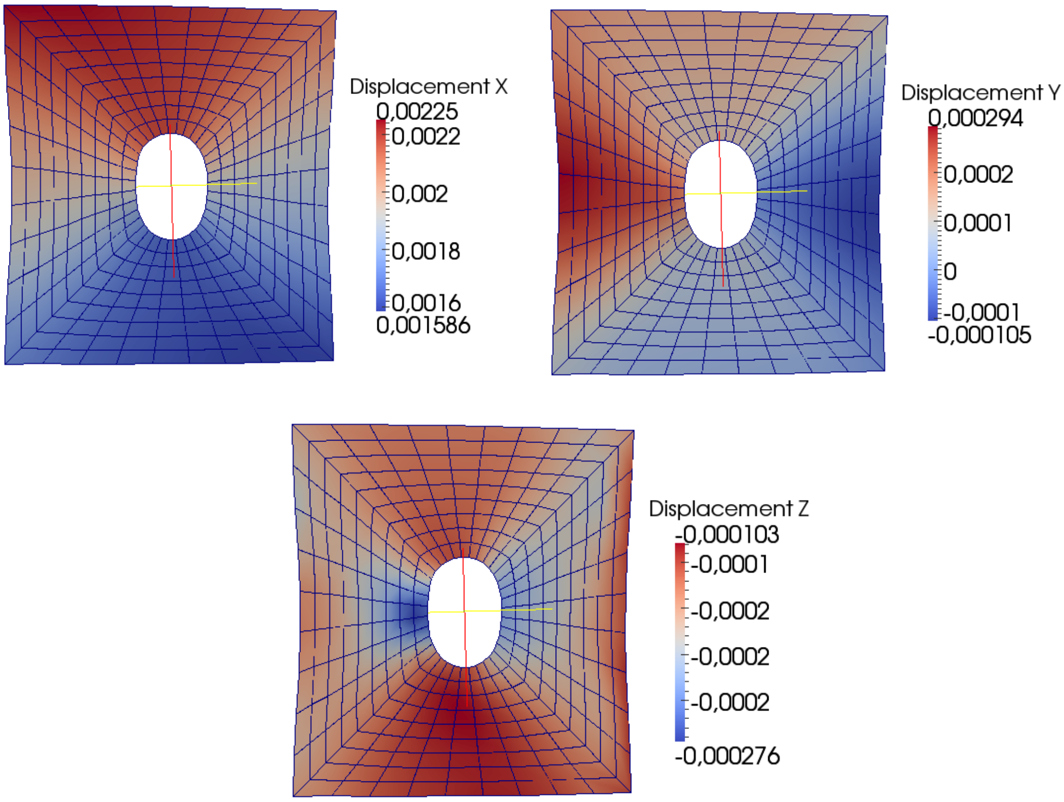

Fig.4.30. The three components of the displacement field obtained via stereo-DIC.

2.5 I-MIC3D with one camera: Using the image from the mono-DIC analysis, the results of

the identification are presented in Figure 4.23. Two meshes are tried. Mesh 0 is the mesh shown in the figure 4.21 with extrusion in the direction normal to the plane with 4 elements through the thickness. Mesh 1 has been refined once in each direction with respect to Mesh 0. Figure 4.23 shows the effect of mesh refinement and the convergence properties of I-MIC3D. For the identification of E and S_y, the convergence takes place in 4 iterations with no affect of mesh refinement. The convergence of H takes place in 5 or 6 iterations for Mesh 1 and Mesh 0 respectively.

Thus I-MIC3D has negligible sensitivity to the mesh size in terms of estimated parameter value as well as convergence speed.

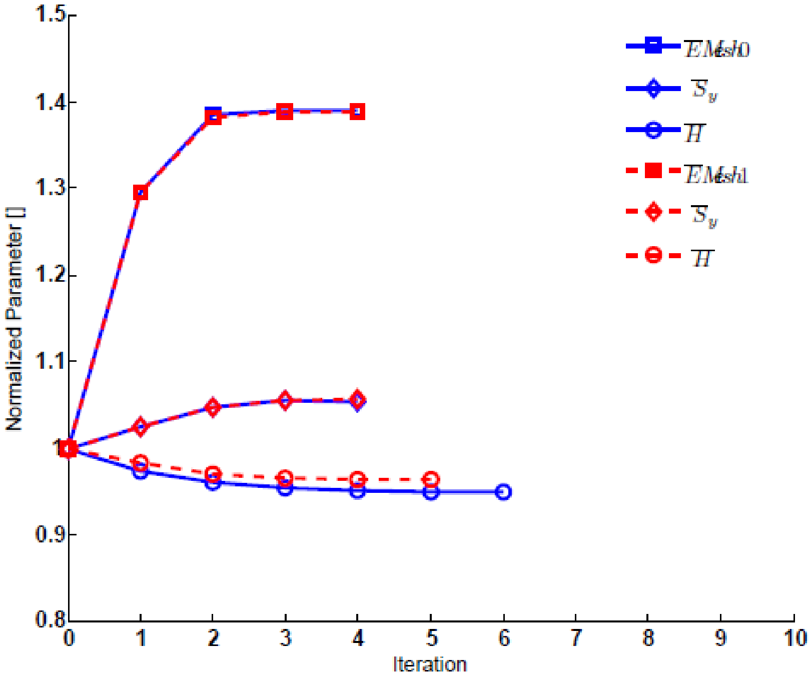

Fig.4.31. Evolution of the identified parameters for type I, II and III analysis on the tensile test using a single camera for different mesh refinement.

2.5 I-MIC3D with two cameras: Now we see the performance of the algorithm in case of stereo-DIC. We see in Figure 4.32, that again the sensitivity to mesh size is minimal.

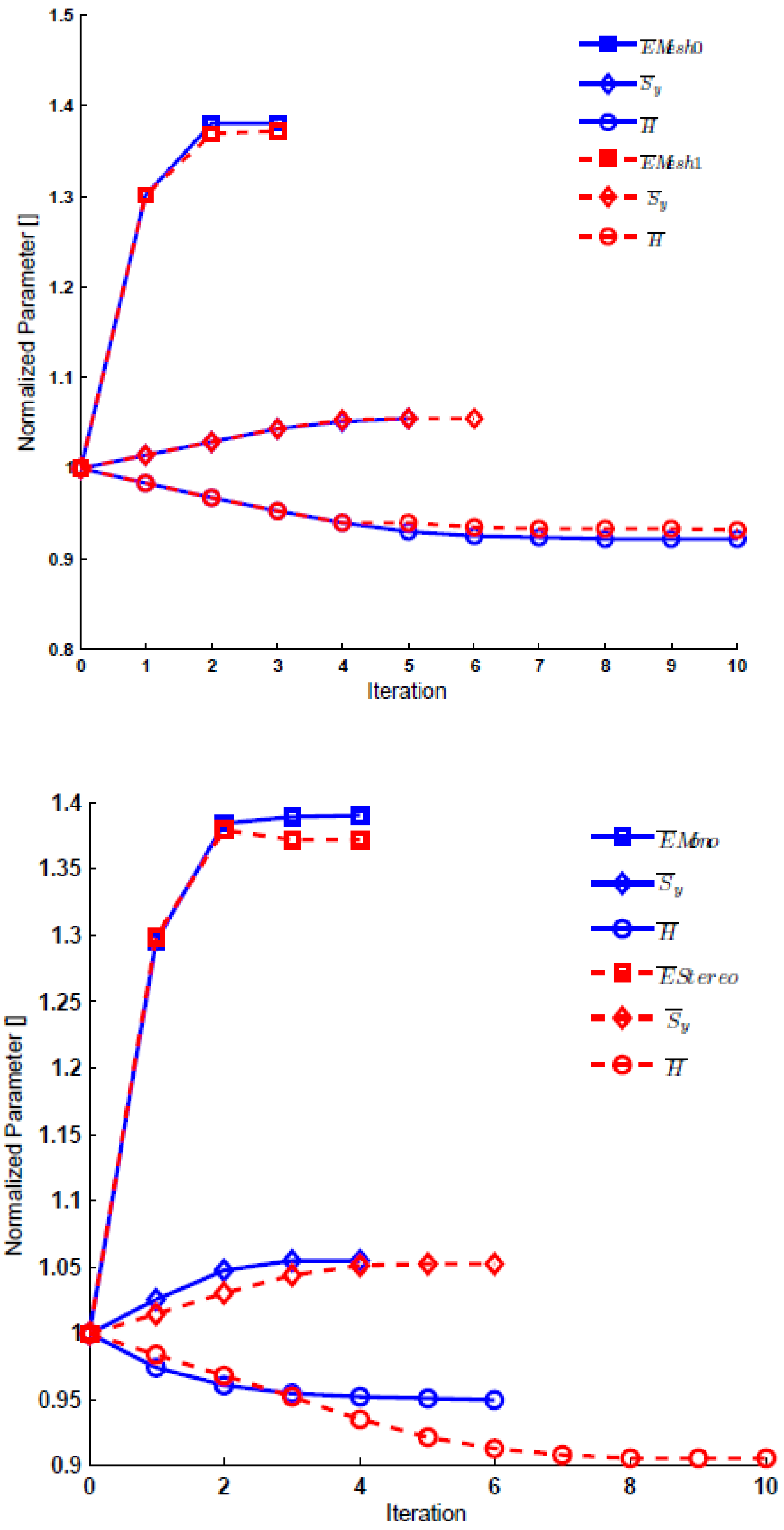

Fig.4.32. Evolution of the identified parameters for type I, II and III analysis on the tensile test using a two camera system for different mesh refinement. The next figure shows the comparison of mono and stereo DIC. The evolution of the identified parameters is plotted for type I, II, III analysis on the real experiment.

2.6 Comparison of mono and stereo I-MIC3D: We can also see that the results of the two optical systems are close and thus the proposed strategy is consistent. Figure 4.25 shows the global response of the two systems, mono and stereo DIC.

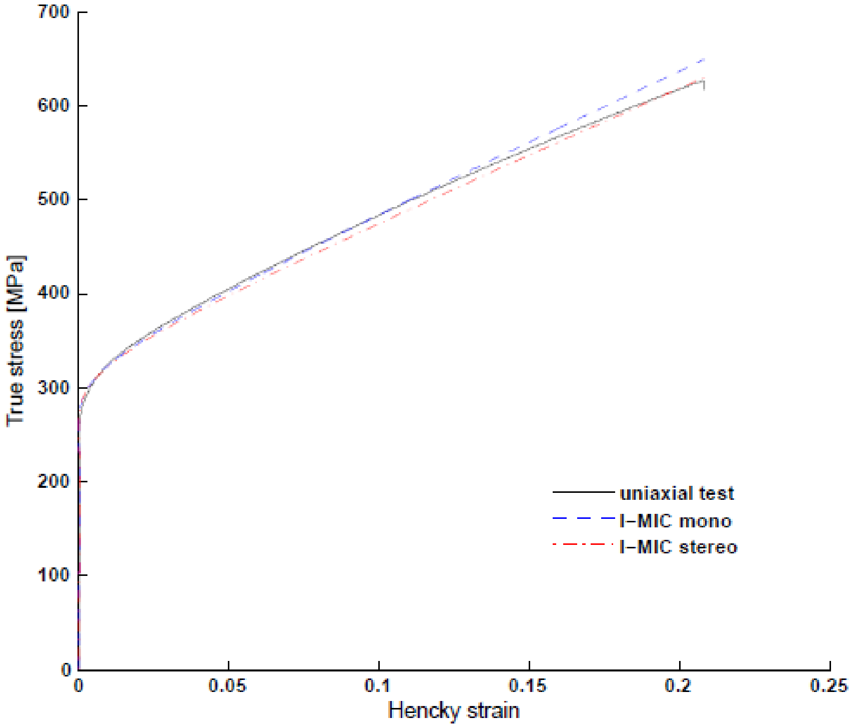

Fig.4.33. Comparison of the stress strain curves obtained by a uniaxial experiment and the identification using Mesh 1 and both mono and stereo camera system.

Figure 4.26 allows to compares the Von misses stress and the accumulated plastic strain for I-MIC3D analysis using Mesh0 for the mono and stereo camera system. The fields are similar which show the consistency of the proposed strategy.

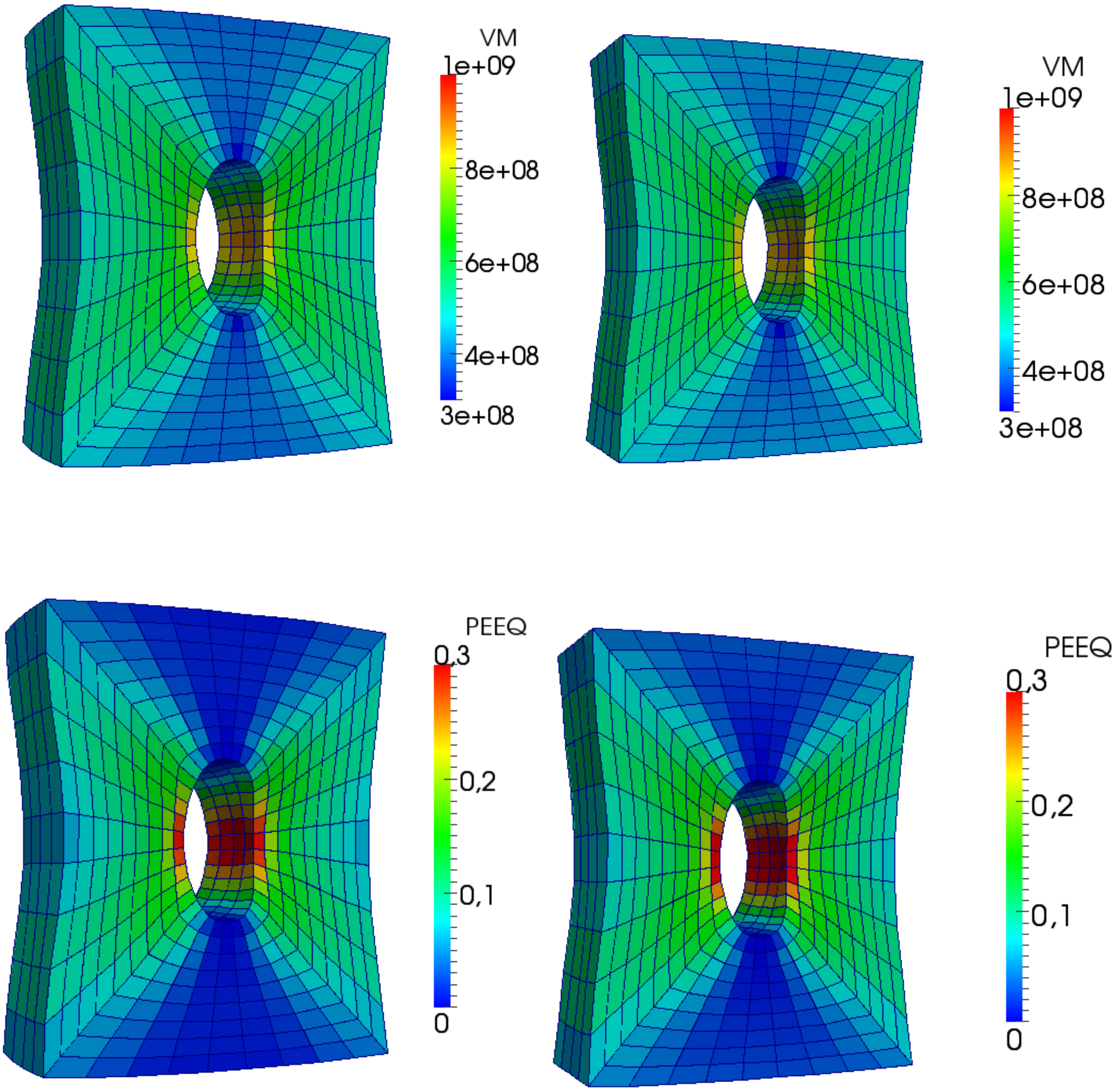

Fig.4.34. Comparison of Von Misses stresses (MPa) and equivalent plastic strain after the numerical simulations for the mono and stereo camera system.

2.7 Correlation error analysis: In the end we do the correlation error analysis. We compare two material laws. The first one is the same as given be equation (4.22) with a linear and a power part. The second with only linear part so that we need to identify only S_y, H . The results are compared with the mean correlation error of DIC. It is clear that for the material law with a power part, the error is close to DIC for the images of stage 0. However, for stage 1 and 2, large differences can be seen. For linear law, the errors are much higher right from the beginning of the analysis. But interestingly, the global responses of the two laws considered are almost similar. Thus the correlation error analysis provides for a more discerning criterion of the better suited material law with comparatively lower correlation error values.

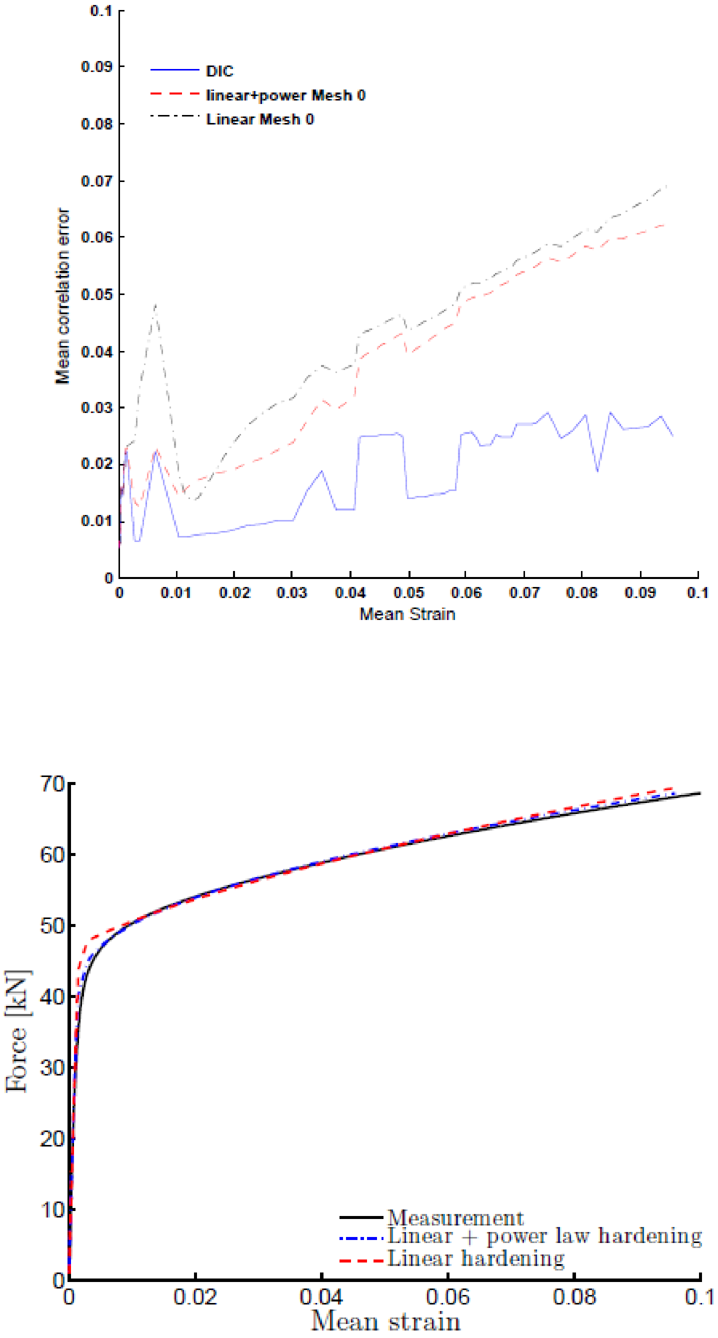

Fig.4.35. Comparison of the mean correlation error and global response of different material laws.

Conclusion

Constitutive law identification has been done traditionally with global force and displacement measurements. The disadvantages of such an approach are the difficulty of using complex models and intricate specimen shapes in the experiments and the requirement of uniform state of stress and strain in the specimen. However, by the use of full field measurements we can have more complex stress states and can identify more complex models that give us a better idea of the constitutive law parameters. Among the full field measurements, digital image correlation is the most famous because of the ease of use and low cost. We need the same instrumentation no matter what the scale of observation is. The cost of CCD cameras and high speed computers is also decreasing and that's why DIC has become the optical method of choice in experimental mechanics. This Ph.D. is a contribution to the use of this interesting technique in the scope of identification of constitutive law of materials.

Together with DIC, we need to have suitable numerical strategies for the identification using digital images. However, all the existing strategies pertain to 2D mechanical models. This means that for specimens with finite thickness these strategies will not give accurate results because of the presence of 3D state of stress and plastic incompressibility. For this reason, a 2D mesh for DIC is extruded along the normal to have 3D effects. Numerical integration for the calculation of internal force vector and stiffness matrix is performed for the nodes on the surface as well as through the thickness.

The strategy, I-MIC3D, offers many benefits. One or more cameras can be used; incorporates 3D effects to account for plastic incompressibility; numerically robust in terms of noise, mesh size and initial parameter guess. The strategy is firstly applied to virtual, noise free images to have a first check on its performance. Finally its application is shown on real images from a tensile test using 304L steel specimens. The results obtained are satisfactory. We get a matching of the global response (force versus strain) obtained via I-MIC3D and experiment. Thus the validation stage is successful.

As a future course, we can incorporate damage and fracture laws in the proposed strategy.

References

[1]. Pagnacco, E., Moreau, A., Lemosse, D., 2007. Inverse strategies for the identification of elastic and viscoelastic material parameters using full field measurements. Material Science and Engineering: A 452-453(0), 737-745.

[2]. Cooreman, S., Lecompte, D., Sol, H., Vantomme, J., Debruyne, D., 2007.Elasto-plastic material parameter identification by inverse methods: Calculation of the sensitivity matrix. International Journal of Solids and Structures: 44, 4329-4341.

[3]. Geymonat, G., Pagano, S., 2003.Identification of mechanical properties by displacement field measurement: A variational approach. Meccanica 38, 535-545.

[4]. Claire, D., Hild, F., Roux, S., 2004. A finite element formulation to identify damage fields: the equilibrium gap method. International Journal for Numerical Methods in Engineering. 2, 189-208.

[5]. Grédiac, M., 1989. Principe des travaux virtuels et identification. Comptes rendus de l'Académie des sciences. Série 2, Mécanique, Physique, Chimie, Sciences de l'univers, Sciences de la Terre 309 (1), 1-5.

[6]. Kavanagh, K., Clough, R., 1971. Finite element applications in the characterization of elastic solids. International Journal of Solids and Structures 7, 11-23.

[7]. Réthoré, J., 2010. A fully integrated noise robust strategy for the identification of constitutive laws from digital images. International Journal for Numerical Methods in Engineering. 84, 631-660.

[8]. Lemaitre J., Chaboche J.L., Mechanics of Solid Materials, Cambridge University Press, 1990.

[9]. Ashby M., Shercliff H., Cebon D., Materials Engineering, Science, Processing and Design, Elsevier, 2007.

[10]. Zink, A.A.G., Davidson,R.W. ,Hanna,R.B., 1995. Strain Measurement in Wood Using a Digital Image Correlation Technique. Wood Fiber Science, 27, 346-359.

[11]. Vendroux, G., ,Knauss, W.G., 1998.Submicron Deformation Field Measurements: Part II, Improved Digital Image Correlation. Experimental Mechanics, 38, 86-92.

[12]. Sutton, M.A., Boone, M.L., Ma,F., ,Helm, J.D., 2000. A combined Modeling-experimental study of the crack opening displacement criterion for characterization of stable growth under mixed mode I/II Loading in thin sheet metals. Engineering Fracture Mechanics, 66, 171-185.

[13]. Reynolds, A.P., Duvall, F., 1999. Digital Image Correlation for determination of weld and base metal constitutive behaviour. The Welding Journal Research Supplement, 78(10), 355-360.

[14]. Chu, T.C., Ranson, W.F., Sutton, M.A., ,Peters, W.H., 1985. Applications of Digital Image Correlation Techniques to Experimental Mechanics. Experimental Mechanics, 25, 232-244.

[15]. Rannou, J., Limodin, N., et al, 2010. Three dimensional experimental and numerical multiscale analysis of a fatigue crack. Computer methods in applied mechanics and engineering , 199, 1307-1325.

[16]. Vendroux, G., Knauss ,W.G., 1988. Submicron Deformation Field Measurements Part I, Developing a Digital Scanning Tunneling Microscope. Experimental Mechanics, 38, 18-23.

[17]. Réthoré, J., Hild, F., Roux, S., 2007.Shear band capturing using a multiscale extended digital image correlation technique. Computer methods in Applied Mechanics and Engineering, 196(49-52):5016-5030.

[18]. Besnard, G., Hild, F., Roux, S., 2006.Finite Element displacement fields analysis from digital images: Application to Portevin-Le Chatelier bands. Experimental Mechanics 46:789-803.

[19]. Avril, S., Bonne, M., Bretelle, A., Grediac, M., Hild, F., Lenny, P., Latourte, F., Lemosse, D., Pagano, S., Pagnacco, E., Allix, O., Deu, JF., 2008. Overview of identification methods of mechanical parameters based on full-field measurements. Experimental Mechanics 48(4): 381-402.

[20]. Avril, S., Pierron, F., 2007. General Framework for the identification of constitutive parameters from full-field measurements in linear elasticity. International Journal of Solids and Structures 44(14-15): 4978-5002.

[21]. Giton, M., Caro-Bretelle, AS., Ienny, P., 2006. Hyper-elastic behaviour identification by a forward problem resolution: application to a tear test of a silicone-rubber. Strain 42:291-297.

[22]. Hoc, T., Gélébart, L., Crépin, J., Zaoui, A., 2003. A procedure for identifying the plastic behaviour of single crystals from the local response of polycrystals. Acta Mater 51:5479-5490.

[23]. Mahnken, R., 2004. A comprehensive study of a multiplicative elastoplasticity model coupled to damage to include parameter identification. Comput Struct 74:179-200.

[24]. Pagnacco, E., Lemosse, D., Hild, F., Aimot, F., 2005. Inverse strategy from displacement field measurement and distributed forces using FEA. In: 2005 SEM annual conference and exposition on experimental and applied mechanics, Portland, 7-9 June 2005.

[25]. Hild, F., Roux, S., 2006. Digital Image Correlation: From measurement to identification of elastic properties- a review. Strain 42:69-80.

[26]. Meuwissen, MHH., Oomens, CWJ., Baaijens, FPT., Petterson, R., Janssen, JD., 1998. Determination of the elasto-plastic properties of aluminium using a mixed numerical-experimental method. J Mater Process Technol 75:204-211.

[27]. Roux S., Hild, F., 2008. Digital Image Mechanical Identification (DIMI). Experimental Mechanics 48(4):495-508.

[28]. Réthoré, J., Hild, F., Roux S. 2007. Extended digital image correlation with crack shape optimization. International Journal for Numerical Methods in Engineering, 73(2): 248-272 .

[29]. Réthoré, J., Elguedj, T., Simon, P., Coret, M., 2009. On the use of NURBS functions for displacement derivatives measurement by digital image correlation. Experimental Mechanics, 50(7): 1099-1116.

[29]. Bornet, M., Brémand, F., Doumalin, P., Dupré, J.-C., Fazzini, M., Grédiac, M.,Hild, F, Mistou, S., Molimard, J., Orteu, J.-J., Robert, L., Surrel, Y., Vacher, P., 2009. Assessment of Digital Image Correlation measurement errors: methodology and results. Experimental Mechanics, 50(7): 1099-1116.

[30]. Siebert, T., Becker, T., Spiltthof, K., Neumann, I., Krupka, R., 2007. Error estimations in digital image correlation technique. Applied Mechanics and Materials vols.7-8: 265-270.

[31]. Lecompte, D., Smits, A., Bossuyt, S., Sol, H., Vantomme, J., Van Hemelrijck, D., Habraken, A.M., 2006. Quality assessment of speckle patterns for digital image correlation. Optics and Lasers in Engineering 44: 1132-1145.

[32]. Chu, T.C., Ranson, W.F., Sutton, M.A., Peters, W.H., 1985. Applications of Digital Image Correlation Techniques to Experimental Mechanics, 25(3), 232-244.

[33]. Triconnet, K., Derrien, K., Hild, F., Baptise, D., 2009. Parameter choice for optimized digital image correlation. Optics and Lasers in Engineering 47: 728-737.

[34]. Triconnet, K., Derrien, K., Hild, F., Baptise, D., 2009. Parameter choice for optimized digital image correlation. Optics and Lasers in Engineering 47: 728-737.

[35]. Bui, H., Constantinescu, A., Maigre, H., 2004. Numerical identification of linear cracks in 2D elastodynamics using the instantaneous reciprocity gap. Inverse Problems 20, 993.

[36]. Grédiac, M., Pierron, F., Avril, S., Toussaint, E., 2006. The virtual fields method for extracting constitutive parameters from full-field measurements: a review. Strain 42(4), 233-253.

[37]. Grédiac, M., Pierron, F., Avril, S., Toussaint, E., 2006. The virtual fields method for extracting constitutive parameters from full-field measurements: a review. Strain 42(4), 233-253.

[38]. Leclerc, H., Perie, J., Roux, S., Hild, F., 2009. Computer Vision/ Computer Graphics Callobration Techniques. Springer, Berlin, Ch. Integrated Digital Image Correlation for the Identification of Mechanical Properties.

[39]. Réthoré, J., Hild, F., Roux, S., 2009. An extended and integrated digital image correlation technique applied to the analysis of fractured samples. European Journal of Computational Mechanics 18, 285-306.

[40]. Madsen, K., Nielsen, H.B., Tingleff, O., 2004. Methods for non-linear least square problems. Informatics and Methamatical Modelling, Technical University of Denmark.

[41]. Quarteroni, A., Saleri, F. Scientific Computing with Matlab and Octave, Springer, 2006.

[42]. Lecompte, D., Smiths, A., Sol, H., J., Vantomme, J., Van Hemelrijck, D, 2007. Mixed Numerical-Experimental Technique for orthotropic parameter identification using biaxial tensile tests on cruciform specimens. International Journal of Solids and Structures: 44, 1643-1656.

[43]. Lecompte, D., Smiths, A., Bossuyt, S., Sol, H., J., Vantomme, J., Van Hemelrijck, D., Habraken, A.M., 2006. Quality assessment of speckle patterns for digital image correlation.Opics and Lasers in Engineering: 44, No 11, 1132-1145.

[44]. Orteu, J.-J., Cutard, T., Garcia, D., Cailleux, E., 2007. Application of stereovision to the mechanical characterisation of ceramic refractories reinforced with metallic fibres. Opics and Lasers in Engineering: 44, No 11, 1132-1145.

[45]. Sun, Y., Pang, J., Wong, C., Su, F., 2005. Finite-element formulation for a digital image correlation method. Applied Optics 44 (34), 7357-7363.

[46]. Sutton, M., Wolters, W., Peters, W., Ranson, W., McNeill, S., 1983. Determination of displacements using an improved digital image correlation method. Image Vision Computing 1 (3), 133-139.

[47]. Wu, T., Coret, M., Combescure, A., 2011. Strain localization and damage measurement by full 3d digital image correlation: Application to 15-5ph stainless steel. Strain 47 (1), 49-61.

[48]. Bui, H., Constantinescu, A., Maigre, H., 2004. Numerical identification of linear cracks in 2d elastodynamics using the instantaneous reciprocity gap. Inverse problems 20, 993.

[49]. Genovese, K., Lamberti, L., Pappalettere, C, 2005. Finite element analysis of a new customized composite post system for endodontically treated teeth. Journal of Biomechanics 38(12): 2375-2389.

[50] Levenberg, K, 1944. A method for the solution of certain nonlinear problems in least squares. Quarterly of Applied Mathematics 2(2): 164-168.

[51] Oomens, C., Ratingen, M., Janssen, J., Kok, J., Hendriks, M, 1993. A numerical-experimental method for a mechanical characterization of biological materials. Journal of Biomechanics, 26: 617-617.

[52] Réthoré, J., Roux, S., Hild, F, 2006. Noise-robust stress intensity factor determination from kinematic field measurements. Engineering Fracture Mechanics 75(13): 3763-3781.

[53] Réthoré, J., Roux, S., Hild, F, 2009. An extended and integrated digital image correlation technique applied to the analysis of fractured samples. European Journal of Computational Mechanics 18: 285-306.

[54] Réthoré, J., Besnard, G., Vivier, G., Hild, F., Roux, S, 2008. Experimental investigation of localized phenomena using digital image correlation. Philosophical Magazine 88(28, 29): 3339-3355.

[55] Leclerc, H., Périe, J-N., Hild, F., Roux, S. Corrélation d'images volumiques : Quelles limites à la résolution spatiale ? 10^{e} Colloque National en Calcul des Structures, 9-13 Mai, 2011, Presqu'ile de Giens (Var).

[56] Hild, F., Raka, B., Baudequin, M., Roux, S., Cantelaube, F, 2002. Multi-scale displacement field measurements of compressed mineral wool samples by digital image correlation. Applied Optics 41 (32) 6815-6828.

[57] Xavier, F., Sylvian, C., François, H., 2007. Controlling testing machines with digital image correlation. Experimental Techniques 31, (3) 57-63.

[58] Leclerc, H., Perie, J.N., Roux, S., Hild, F, 2009. Integrated Digital Image Correlation for the Identification of Mechanical Properties. MIRAGE 2009 - 4th International Conference on Computer Vision/Computer Graphics Collaboration Techniques. Vol 5496. Pages 161-171.

[59] Senseny, P. E., Brodsky, N. S., De Vries, K. L., 1993. Parameter Evaluation for a Unified Constitutive Model. Journal of Engineering Materials and Technology 115, 157-162.

[60] Réthoreé, J., Besnard, G., Vivier, G., Hild, F., Roux, S. 2008. Experimental investigation of localized Phenomena using digital image correlation. Philosophical Magazine; 88(28,29): 3339-3355.

List of Figures

Appendix

Example Mono-DIC Program

```
clear param1 model1
t=cputime;

filexp='-10';
filres=['dic-mono',filexp];
lo=1580-460;
pix2m=20e-3/(lo);

images=[1:10,12:2:20,25:5:440];
roi(1)=400-0;
roi(2)=1600+10;
roi(3)=410+10;
roi(4)=1620-10;

yc=0.5*(1140+880)+10;
xc=0.5*(1130+890);

param1.reference_image='304L_monotonic-0000_0.tif';
imdefs=cell(1,length(images));
if length(images)>1
    for iim=1:length(images)
    filim=sprintf('304L_monotonic-%04d_0.tif',images(iim));
    imdefs{iim}=filim;
    end
else
    filim=sprintf('304L_monotonic-%04d_0.tif',images(1));
    imdefs=filim;
end
param1.image_number=images;

param1.deformed_image=imdefs;

param1.roi=roi;
param1.result_file=filres;
param1.analysis='correlation';
param1.pixel_size=1;
param1.regularization_type='tiko';
param1.restart=0;

param1.iter_max=30;
param1.convergance_limit=1.e-3;
LoadParameters(param1);

nscale=3;
mesh_size=ones(1,2)*32;
model1.nscale=nscale;
model1.basis='fem';
model1.mesh_size=mesh_size;
model1.mesh_file='trou-10.vtk';
glue{1,:}={'scale',[0;0;0],1/pix2m};
glue{2,:}={'rotate',[0;0;1],[0;0;0],pi/2-pi/150};
glue{3,:}={'translate',[xc;yc;0]};
model1.gluing_parameters=glue;


LoadParameters(model1,1);
```

```
ReferenceImage();
LoadMeshes(1);
%%
LoadMask(1);
mscale=nscale;
for iscale=mscale:-1:1
disp(sprintf('Pre-processing scale %d...',iscale));
CreateBasisFunction(iscale,1);
ComputeGradFPhi(iscale,1);
AssembleCorrelationOperator(iscale,1);
end

CreateGradBasisFunction(1,1);
%%
U1=[];

 for iscale=mscale:-1:1
         Uini=InitializeSolution(U1,iscale,1);

 [U1]=Solve(Uini,iscale,1);
 end
%%

U=U1;
unix(['cp TMP/1_error_0.mat ' filres,'-error.mat']);

load(['TMP/1_mesh_0'],'Nnodes','Nelems','xo','yo','conn','elt','ng','selected');
param=param1;
model=model1;
nmod=1;
save([filres,'.mat'],'U','roi','Nnodes','Nelems','xo','yo','param','model',
'nmod','conn','elt','ng');
if length(images)==1
    postpro(filres);
end
postproVTK(filres);
%%
found=find((~selected)&(abs(xo-max(xo))<50));
Uxmin=mean(U(found,:),1);
Uymin=mean(U(length(xo)+found,:),1);
Xmin=mean(xo(found));
Ymin=mean(yo(found));
found=find((~selected)&(abs(xo-min(xo))<50));
Uxmax=mean(U(found,:),1);
Uymax=mean(U(length(xo)+found,:),1);
Xmax=mean(xo(found));
Ymax=mean(yo(found));
n=[(Xmax-Xmin);(Ymax-Ymin)];
lr=norm(n);
n=n/lr;
Emean=abs((Uxmax-Uxmin)*n(1)+(Uymax-Uymin)*n(2))/(lr);

save([filres,'.mat'],'Emean','-append');
```

Example Mono-IMIC-3D

```
close all
clear all
%%
%Preparation
%Output file
%images to be used for identification
%loading input force vector
%defining parameters
t=cputime;

filexp='-10';
fildic=['dic-mono',filexp];
filexp='-r-0-linear';
filreso=['mic-mono-swift-step',filexp];

computeall=0;

%images=[5:5:350];
images=[1:10,12:2:20,25:5:300];
ime=[1:5];
imsy=[1:12];
load('force_mono','Fim');
load(fildic);
Uini=U;
clear U

images0=param.image_number;
imdefs=param.deformed_image;
keep=[];
for iim=1:length(images)
    id=find(images0==images(iim));
    if ~isempty(id)
        keep=[keep,id];
    end
end
Uini=Uini(:,keep);
Fim=Fim(:,keep);
imdefs=imdefs(keep);
param.image_number=images;
param.deformed_image=imdefs;
param.result_file=filreso;
param.update_max=50;
param.helper='abaqus';
param.abaqus_cpus=4;
ro=2.5e-3;
pix2m=20e-3/(1580-460);


param.pixel_size=pix2m;
%param.under_relaxation=2;
param.compute_fint=false;
param.restart=1;
param.iter_max=20;
param.regularization_type='none';
param.search_convergance_limit=1e-3;
LoadParameters(param);
%%
%Initial value of Parameters
%Material model
```

```
%Elastic Plastic behaviour choice
%Output variables from Abaqus simulation
%
Eo=168e9;
nuo=0.25;
mu=0.5*Eo/(1+nuo);
lambda = nuo*Eo/((1.+nuo)*(1.-2.*nuo));%DP
Sy=284e6;
H=1.48e9;
d=0.042;

C=d*Sy/(Eo-H);
B=Sy*C^(-d);
mu=0.5*Eo/(1+nuo);
matmod.mu=mu;
matmod.lambda=lambda;
matmod.young=Eo;
matmod.nu=nuo;

matmod.hardening='swift';
%matmod.hardening='lin';
matmod.delta=d;
matmod.H=H;
matmod.Sy=Sy;
matmod.B=B;
matmod.C=C;


model.material_model='elastic_plastic_homogeneous_isotropic';
model.material_parameters=matmod;
model.reduced_integration=true;
model.nlgeom=true;
model.abaqus_output={'LE','S','PEEQ'};
LoadParameters(model,1);

%%
%Loading VTK mesh file
ReferenceImage();
LoadMeshes(1);
%%
%Creating basis functions,calculating their derivatives & type of
%regularization.
load(['TMP/1_mesh_0'],'selected','xo','yo');
%Uinif=RefineMesh(1,1+0,Uini);
Uinif=Uini;
CreateBasisFunction(1,1);
ComputeGradFPhi(1,1);
AssembleCorrelationOperator(1,1);
%%
%selecting boundary nodes
load(['TMP/1_mesh_0'],'xo','yo','selected');
top=(~selected)&(abs(xo-max(xo))<50);
ytop=yo(top);xtop=xo(top);
figure
plot(xo,yo,'x')
hold on
plot(xtop,ytop,'ro')
y1=min(ytop);x1=xtop(find(ytop==y1));
y2=max(ytop);x2=xtop(find(ytop==y2));
plot(x1,y1,'ms')
```

```
plot(x2,y2,'ms'
%%
%defining specimen sections in pixels
%extrusion parameters

lr=20e-3/pix2m;
er=8e-3/pix2m;
lo=abs(x2-x1+1i*(y2-y1));
eo=er*lo/lr;
Sr=lr*er;
So=lo*eo;
extr.nlayers=2*2*1+1;
extr.thickness=ceil(eo);
model.extrusion_method='3d';
model.extrusion_parameters=extr;
LoadParameters(model,1);

[U3Dini,Mp]=ExtrudeModel(1,Uinif);
CreateGradBasisFunction3D(1,1);
%%
%Application of DIC displacement as boundary condition
%Performing numerical simulation under prescribed displacement
%Comparison of experimental and numerical force

load(['TMP/1_3d_mesh_0'],'Nnodes','Nelems','xo','yo','zo','conn','elt','ng'
,'selected');
L=[ones(length(xo),1),zeros(length(xo),1),zeros(length(xo),1),yo,zeros(leng
th(xo),1),-zo;...
zeros(length(xo),1),ones(length(xo),1),zeros(length(xo),1),-
xo,zo,zeros(length(xo),1);...
zeros(length(xo),1),zeros(length(xo),1),ones(length(xo),1),zeros(length(xo)
,1),-yo,xo];
Urbm=L\U3Dini;

Ubcs=0*U3Dini;
top=find((~selected)&(abs(xo-max(xo))<50));
Utop=[U3Dini(top,:);U3Dini(top+prod(Nnodes),:)];
L=[ones(length(top),1),zeros(length(top),1),yo(top),zeros(length(top),1);..
.
zeros(length(top),1),ones(length(top),1),-xo(top),yo(top)];
Urbmtop=L*(L\Utop);
Ubcs(top,:)=Urbmtop((1:length(top)),:);
Ubcs(top+prod(Nnodes),:)=Urbmtop(length(top)+(1:length(top)),:);
top=find((~selected)&(abs(xo-min(xo))<50));
Utop=[U3Dini(top,:);U3Dini(top+prod(Nnodes),:)];
L=[ones(length(top),1),zeros(length(top),1),yo(top),zeros(length(top),1);..
.
    zeros(length(top),1),ones(length(top),1),-xo(top),yo(top)];
Urbmtop=L*(L\Utop);
Ubcs(top,:)=Urbmtop((1:length(top)),:);
Ubcs(top+prod(Nnodes),:)=Urbmtop(length(top)+(1:length(top)),:);

found=find(~selected);
indi=[found;found+prod(Nnodes)];
found=find((~selected)&(zo==0));
indi=[indi;found+2*prod(Nnodes)];
indj=1:length(indi);
C=sparse(indi,indj,1,3*prod(Nnodes),length(indj));
Up=U3Dini(indi,:);
Fo=zeros(3*prod(Nnodes),1);

[U,Fu]=SolveNL(1,Fo,C,Up);
```

```
Fx=0.5*sum(abs(Fu((1:size(Fu,1)/3),:)))*pix2m^2;

figure
plot(Fim/(Sr*pix2m^2),'b')
hold on
plot(Fx/(So*pix2m^2),'ro')

found=find(~selected);
Fo=zeros(3*prod(Nnodes),size(U,2));
Fo(found,:)=Fu(found,:);
Fo(found+length(xo),:)=Fu(found+length(xo),:);

Fo=Fo*diag((Fim(1:length(Fx))/Sr)./(Fx/So));



found=find(~selected(:));
first=find(selected,1,'first');
indi=[found+2*prod(Nnodes);first;first+prod(Nnodes)];
last=find(selected,1,'last');
if abs(xo(first)-xo(last))>abs(yo(first)-yo(last))
    indi=[indi;last+prod(Nnodes)];
else
    indi=[indi;last];
end
indj=1:length(indi);
C=sparse(indi,indj,1,3*prod(Nnodes),length(indi));
Up=U3Dini(indi,:);

Urbmall=Urbm;
Upall=Up;
Foall=Fo;

%%
%Parameter Identification of Young's Modulus
Urbm=Urbmall(:,ime);
Up=Upall(:,ime);
Fo=Foall(:,ime);
save('UpdateUField','Up','C','Fo','Urbm');

parame=param;
parame.image_number=param.image_number(ime);
parame.deformed_image=param.deformed_image(ime);
LoadParameters(parame);
model.searched_parameter={'E'};
LoadParameters(model,1);
Pini=[1.];
[U1,Pe]=SolveMIC(Pini,1);


load(fullfile('TMP',sprintf('%d_solvemic_%d',1,0)),'Phist','Ehist','niter')
;
load('TMP/1_sens_0.mat');
save(['mic-mono-swift-step','-r-0-
e','.mat'],'Phist','Ehist','niter','sens');
param0=param;
UpdateMaterial(1,Pe);
load('TMP/1_param','param');
model=param;
```

```
param=param0;

%%
%Parameter Identification of Initial Yield Stress
Urbm=Urbmall(:,imsy);
Up=Upall(:,imsy);
Fo=Foall(:,imsy);
save('UpdateUField','Up','C','Fo','Urbm');

paramsy=param;
paramsy.image_number=param.image_number(imsy);
paramsy.deformed_image=param.deformed_image(imsy);
LoadParameters(paramsy);
model.searched_parameter={'Sy'};
LoadParameters(model,1);
Pini=[1.];
[U1,Psy]=SolveMIC(Pini,1);



load(fullfile('TMP',sprintf('%d_solvemic_%d',1,0)),'Phist','Ehist','niter')
;
load('TMP/1_sens_0.mat');

 save(['mic-mono-swift-step','-r-0-
sy','.mat'],'Phist','Ehist','niter','sens');
param0=param;
UpdateMaterial(1,Psy);
load('TMP/1_param','param');
model=param;
param=param0;




%%
%Parameter Identification of Linear Hardening Slope
Urbm=Urbmall;
Up=Upall;
Fo=Foall;

save('UpdateUField','Up','C','Fo','Urbm');
LoadParameters(param);
 model.searched_parameter={'H'};
LoadParameters(model,1);
Pini=ones(length(model.searched_parameter),1);
[U1,Ph]=SolveMIC(Pini,1);


load(fullfile('TMP',sprintf('%d_solvemic_%d',1,0)),'Phist','Ehist','niter')
;
load('TMP/1_sens_0.mat');
save(['mic-mono-swift-step','-r-0-
h','.mat'],'Phist','Ehist','niter','sens');
param0=param;
UpdateMaterial(1,Ph);
load('TMP/1_param','param');
model=param;
param=param0;
%%
%%Parameter Identification of Power exponent
Urbm=Urbmall;
Up=Upall;
```

```
Fo=Foall;

save('UpdateUField','Up','C','Fo','Urbm');
param.result_file=filreso;
LoadParameters(param);
model.searched_parameter={'d'};
LoadParameters(model,1);

Pini=[1.];
[U1,Pd]=SolveMIC(Pini,1);

filexp='-r-0-H';
filres=['mic-mono-swift-step',filexp];
param.result_file=filres;
LoadParameters(param);

model.searched_parameter={'Sy','d','H','E'};
LoadParameters(model,1);
P=[Psy;Pd;Ph;Pe];
U=U1;
param0=param;
UpdateMaterial(1,P);
load('TMP/1_param','param');
model=param;
param=param0;
unix(['cp TMP/1_error_0.mat ' filres,'-error.mat']);
unix(['cp TMP/1_sens_0.mat ' filres,'-sens.mat']);

load(['TMP/1_3d_mesh_0'],'Nnodes','Nelems','xo','yo','zo','conn','elt','ng'
);

load(fullfile('TMP',sprintf('%d_solvemic_%d',1,0)),'Phist','Ehist','niter')
;
nmod=1;
save([filres,'.mat'],'Fim','P','Phist','Ehist','niter','U','roi','Nnodes','
Nelems','xo','yo','zo','param','model','nmod','conn','elt','ng');
postproAbaqus(filres,1);

found=find((~selected)&(abs(xo-max(xo))<50));
Umin=mean(U(found,:),1);
found=find((~selected)&(abs(xo-min(xo))<50));
Umax=mean(U(found,:),1);
Emean=abs(Umax-Umin)/(lo);

found=find((~selected)&(abs(xo-max(xo))<50)&(zo==min(zo)));
Uxmin=mean(U(found,:),1);
Uymin=mean(U(length(xo)+found,:),1);
Xmin=mean(xo(found));
Ymin=mean(yo(found));
found=find((~selected)&(abs(xo-min(xo))<50)&(zo==min(zo)));
Uxmax=mean(U(found,:),1);
Uymax=mean(U(length(xo)+found,:),1);
Xmax=mean(xo(found));
Ymax=mean(yo(found));
n=[(Xmax-Xmin);(Ymax-Ymin)];
lr=norm(n);
n=n/lr;
Emean2=abs((Uxmax-Uxmin)*n(1)+(Uymax-Uymin)*n(2))/(lr);
save([filres,'.mat'],'Emean','Emean2','-append');
```